Using Landslides Induced by Earthquakes for Paleoseismology, Hazard Prediction, and Spatial Analysis

Erich Herzig

A dissertation
submitted in partial fulfillment of the
requirements for the degree of

Doctor of Philosophy

University of Washington

2024

Reading Committee:

Alison Duvall, Chair

Joseph Wartman

Erin Wirth

Program Authorized to Offer Degree:
Earth and Space Sciences

University of Washington

Abstract

Using Landslides Induced by Earthquakes for Paleoseismology, Hazard Prediction, and Spatial Analysis

Erich Herzig

Chair of the Supervisory Committee:
Alison Duvall
Department of Earth and Space Sciences

Landslides are a dangerous natural hazard that can kill people and damage property. Mass movement on hillslopes also erodes mountains and shapes landscapes over the longer term. By studying both landslides and their causes, we can better understand how they influence the environment and how to minimize the risk they pose to people and property. Landslides can be caused by shaking from an earthquake. Unlike landslides induced by other forces such as rainfall, earthquake induced landslides all happen at roughly the same time, which can amplify their hazards and impact on the landscape. I use this pulsed nature of earthquake induced landslides to investigate past earthquakes on the Seattle Fault. The Seattle Fault represents a major hazard for the city of Seattle, but has not experienced a major earthquake since approximately 1000 years ago. Because of this, earthquakes on the fault are poorly understood. We date past landslides in the area using a novel roughness based landslide dating technique. By looking for times when more landslides occurred than normal in places that would likely have strong shaking from an earthquake, I find landslide clusters that likely represent past earthquakes on the Seattle Fault. This method can be generalized to other areas prone to landsliding and infrequent but strong earthquakes. Next, I examine different scenarios to predict where a modern Seattle Fault earthquake would induce landslides. By combining the ground motions from 18 different scenario Seattle Fault kinematic earthquake models and a multi-modal landslide hazard model, I find where landslides are likely to occur

and what controls these patterns. Over all scenarios, I find that there are always high numbers of modelled landslides (10% of slopes failing with translational landslides, and 4% of slopes failing in rotational landslides) and that these landslides mostly occur in the same places as modern rainfall induced landslides. Between scenarios, water saturation and local geologic strength are more important factors than earthquake properties such as hypocenter and magnitude. Finally, I investigate the assumptions behind the roughness based landslide dating technique used previously. I measure the roughness of earthquake induced landslide inventories from both the 1994 Northridge CA, USA and 2016 Kaikoura, NZ earthquakes. The roughness based dating method assumes that these landslides are all about the same roughness when they occur, however I find that these landslides actually have a wide range of initial roughness values. The range of initial roughness values can be reduced by filtering landslides by geology and landslide size. I also test how landslide deposits smooth over time by comparing repeat lidar surveys of the 2014 Oso, WA, USA landslide over a ten year period. These data show that geology also plays an important role in determining the rate at which the landslide smooths. Overall I found that when different geologic units are isolated and analysed separately, the variation in roughness in large landslides (Area $\geq$ 10,000 m^2) would lead to a variation in estimated ages of 500 and 200 years. This is similar to the error (200 years) used in Chapter 2 and validates the use of this technique for landslide age estimation.

TABLE OF CONTENTS

LIST OF FIGURES

LIST OF TABLES

DEDICATION

to my dear wife, Paige

Chapter 1

INTRODUCTION

Most of the time, the force of gravity on the material of a slope is balanced by the shear strength holding the slope in place. However, when this balance is upset, landslides can occur (Lu and Godt; 2013). Slope instability can be caused by many factors such as rainfall increasing the weight of the slope, or a shaking from an earthquake adding to the static forces of gravity. These large mass failures can reshape the landscape and be a powerful force for erosion (Malamud et al.; 2004; Korup et al.; 2007; Larsen and Montgomery; 2012). Additionally, landslides pose a threat to both people and property, killing hundreds to thousands of people every year (Petley; 2012). Earthquake induced landslides can amplify effects, as they result in many landslides occurring at the same time. Combined with hazards from the earthquake shaking itself, these landslides can be additionally dangerous (Fan et al.; 2019). Many aspects of earthquake induced landslides, however, are still poorly understood. While shaking intensity has some control on landsliding it cannot fully explain landslide occurrence rates (Keefer; 1984; Malamud et al.; 2004). Additional local conditions such as soil saturation may need to be considered to improve our ability to predict future landslides (Massey et al.; 2018; Bessette-Kirton et al.; 2019). Additionally, most work on earthquake induced landslides has been performed in locations with frequent earthquakes, as it is relatively easy to map where landslides occurred after a modern earthquake. Not all locations with high earthquake hazards have frequent earthquakes, and little work has been done to both characterize future earthquake induced landslide hazard in these areas and develop tools to understand landslides induced by prehistoric earthquakes. In this dissertation, I examine the patterns of when and where earthquake induced landslides have occurred in the past, even in locations with rare earthquakes, and how that informs when and where earthquake induced landslides might happen in the future.

In Chapter 2, I analyze patterns of past landsliding in the Puget Lowlands WA, USA

in order to understand past earthquakes on the Seattle Fault (Herzig et al.; 2023). I use a novel roughness based landslide dating technique (LaHusen et al.; 2016; Booth et al.; 2017) to date over 1,000 landslides in the Puget Lowlands, WA USA. This technique is based on the assumption that landslides start out rough, and smooth or diffuse over time. By measuring the relationship between age and roughness, a landslide's age can be estimated by simply measuring the deposit's roughness. This relationship was re-calibrated based on new radiocarbon ages of 9 benchmark landslides in the study area. I then compared the dated landslide inventory with ground motions from a set of modelled Seattle Fault earthquake ground motions (Stone et al.; 2022), assessing landslides from the past 4000 years to assess if spatial patterns of landsliding correlate with the zones of strongest shaking from modelled Seattle Fault earthquakes. I found that the landslide pattern and earthquake patterns were correlated around the same time as past Seattle Fault earthquakes recorded by other geologic techniques. In addition to being an important regional discovery, Herzig et al. (2023) also suggests that landslide clusters induced by an earthquake may be unique enough to be used to identify past earthquakes.

In Chapter 3, I use kinematic ground motion models of a Seattle Fault earthquake and a multimodal landslide model to predict where landslides are likely to occur in a future Seattle Fault earthquake. This study considers combinations of 18 different 3D kinematic earthquake scenarios, 2 water saturation levels and variation in geologic strength for both translational and rotational landslides in Seattle, WA, USA. The earthquake ground motions cover earthquakes of Magnitude 6.5 and 7, with three different hypocenter locations (west, center, and east), three different slip distributions (roughly west, center, and east) and consider the effects of topography(Stone et al.; 2022). I model saturation levels typical of winter (wet) and summer (dry) conditions in Seattle, and use a Monte Carlo method to vary geologic strength within possible ranges over 50 runs. I then combine traditional Newmark style failure analysis (Wilson and Keefer; 1983) with a multimodal landslide model (Pollock et al.; 2019) to produce maps of probable landsliding. I find that on average 10% of slopes fail with translational landslides, and 4% of slopes fail in rotational landslides. These landslides mostly occur in similar locations as historical rainfall induced landslides, with some exceptions. Overall, variation between scenarios is minimal, but for what variation

there is, it is mostly controlled by water saturation and local geology rather than earthquake properties.

In Chapter 4, I test the main assumptions used in the roughness-age relationship used to date landslides in Chapter 2. These assumptions are: landslide deposits are rougher than surrounding undisturbed hillslopes and are all of a similar initial roughness; and landslides smooth with time and at similar rates. First, I use existing landslide inventories with a known, well documented landslide trigger to measure the initial roughness of thousands of landslides. I investigate two earthquake induced landslide inventories specifically, the 2016 M7.8 Kaikoura, NZ and the 1994 M6.7 Northridge, CA, USA. By studying earthquake induced landslide inventories I ensure that all landslides are occurring at a similar time, with similar conditions such as water saturation level. My results show that landslides from these inventories had a wide range of initial roughness values, with variability in log roughness of 0.83 and 0.75 for Kaikoura and Northridge respectfully. This range in roughness reduces when I assess roughness of only the only the largest of the landslides ($\geq$10,000 m^2). With this restriction, the landslides have less variation, with variations in log mean initial roughness of 0.56 and 0.46 for Kaikoura and Northridge respectively. Roughness values in this range lead to an error in landslide age estimates of 500 (Kaikoura) and 200 (Northridge) years using the roughness age relationship of LaHusen et al. (2020). Next, I measure how landslide deposit roughness smooths over time with repeat Lidar surveys of the 2014 Oso, WA, USA, landslide. I combine roughness measurements directly after the landslide in 2014, in 2017 and a new Lidar dataset collected for this study in 2024. I find that the roughness diffuses at different rates in different geologic units within the landslide deposit. Together the data from these three case study areas shows that both the mean initial roughness and hillslope diffusion rate are different in landslides in different geologic units. As a result, I conclude that the roughness age relationship needs to be recalculated for each new location with different geologic units for higher-fidelity landslide age estimates.

Bibliography

Bessette-Kirton, E. K., Cerovski-Darriau, C., Schulz, W. H., Coe, J. A., Kean, J. W., Godt, J. W., Thomas, M. A. and Hughes, K. S. (2019). Landslides triggered by hurricane maria:

Assessment of an extreme event in puerto rico, *GSA Today* **29**(6): 4–10.

Booth, A., LaHusen, S., Duvall, A. and Montgomery, D. (2017). Holocene history of deep-seated landsliding in the north fork stillaguamish river valley from surface roughness analysis, radiocarbon dating, and numerical landscape evolution modeling, *Journal of Geophysical Research: Earth Surface* **122**(2): 456–472.

Fan, X., Scaringi, G., Korup, O., West, A., Westen, C., Tanyas, H. and Huang, R. (2019). Earthquake-induced chains of geologic hazards: Patterns, mechanisms, and impacts, *Reviews of geophysics* **57**(2): 421–503.

Herzig, E., Duvall, A., Booth, A., Stone, I., Wirth, E., LaHusen, S., Wartman, J. and Grant, A. (2023). Evidence of seattle fault earthquakes from patterns in deep-seated landslides.

Keefer, D. (1984). Landslides caused by earthquakes, *Geological Society of America Bulletin* **95**(4): 406–421.

Korup, O., Clague, J. J., Hermanns, R. L., Hewitt, K., Strom, A. L. and Weidinger, J. T. (2007). Giant landslides, topography, and erosion, *Earth and Planetary Science Letters* **261**(3-4): 578–589.

LaHusen, S., Duvall, A., Booth, A., Grant, A., Mishkin, B., Montgomery, D. and Wartman, J. (2020). Rainfall triggers more deep-seated landslides than cascadia earthquakes in the oregon coast range, usa, *Science advances* **6**(38): 6790.

LaHusen, S., Duvall, A., Booth, A. and Montgomery, D. (2016). Surface roughness dating of long-runout landslides near oso, washington (usa), reveals persistent postglacial hillslope instability, *Geology* **44**(2): 111–114.

Larsen, I. J. and Montgomery, D. R. (2012). Landslide erosion coupled to tectonics and river incision, *Nature Geoscience* **5**(7): 468–473.

Lu, N. and Godt, J. W. (2013). *Hillslope hydrology and stability*, Cambridge University Press.

Malamud, B., Turcotte, D., Guzzetti, F. and Reichenbach, P. (2004). Landslide inventories and their statistical properties, *Earth Surface Processes and Landforms* **29**(6): 687–711.

Massey, C., Townsend, D., Rathje, E., Allstadt, K. E., Lukovic, B., Kaneko, Y., Bradley, B., Wartman, J., Jibson, R. W., Petley, D. et al. (2018). Landslides triggered by the 14 november 2016 m w 7.8 kaikōura earthquake, new zealand, *Bulletin of the Seismological Society of America* **108**(3B): 1630–1648.

Petley, D. (2012). Global patterns of loss of life from landslides, *Geology* **40**(10): 927–930.

Pollock, W., Grant, A., Wartman, J. and Abou-Jaoude, G. (2019). Multimodal method for landslide risk analysis, *MethodsX* **6**: 827–836.

Stone, I., Wirth, E. and Frankel, A. (2022). Topographic response to simulated m w 6.5–7.0 earthquakes on the seattle fault, *Bulletin of the Seismological Society of America* **112**(3): 1436–1462.

Wilson, R. C. and Keefer, D. K. (1983). Dynamic analysis of a slope failure from the 6 august 1979 coyote lake, california, earthquake, *Bulletin of the Seismological Society of America* **73**(3): 863–877.

Chapter 2

EVIDENCE OF SEATTLE FAULT EARTHQUAKES FROM PATTERNS IN DEEP-SEATED LANDSLIDES[1]

Earthquake-induced landslides can record information about the seismic shaking that generated them. In this study, we present new mapping, lidar-derived roughness dating, and analysis of over 1,000 deep-seated landslides from the Puget Lowlands of Washington, USA, to probe the landscape for past Seattle Fault earthquake information. With this new landslide inventory, we observe spatial and temporal evidence of landsliding related to the last major earthquake on the Seattle Fault 1,100 years before present. We find spatial clusters of landslides that correlate with ground motions from recent 3D kinematic models of Seattle Fault earthquakes. We also find temporal patterns in the landslide inventory that suggest earthquake-driven increases in landsliding. We compare the spatial and temporal landslide data to scenario-based ground motion models and find stronger evidence of the last major Seattle Fault earthquake from this combined analysis than from spatial or temporal patterns alone. We also compare the landslide inventory to ground motions from different Seattle Fault earthquake scenarios to determine the ground motion distributions that are most consistent with the landslide record. We find that earthquake scenarios that best match the clustering of 1,100-year-old landslides produce the strongest shaking within a band that stretches from west to east across central Seattle as well as along the bluffs bordering the broader Puget Sound. Finally, we identify other landslide clusters (at 4.6–4.2 ka, 4.0–3.8 ka, 2.8–2.6 ka, and 2.2–2.0 ka) in the inventory which let us infer potential ground motions that may correspond to older Seattle Fault earthquakes. Our method, which combines hindcasting of the surface response to the last major Seattle Fault earthquake, using a roughness aged landslide inventory with forecasts of modeled ground shaking from 3D

[1]This chapter was published in the Bulletin of the Seismological Society of America in 2023 with authors Erich Herzig, Alison Duvall, Adam Booth, Ian Stone, Erin Wirth, Sean LaHusen, Joseph Wartman, and alex grant

seismic scenarios, showcases a powerful new approach to gleaning paleoseismic information from landscapes.

2.1 Introduction

Strong ground motions from large earthquakes have long been known to trigger widespread landsliding (e.g., Keefer (1984); Jibson and Keefer (1993); Malamud et al. (2004)) that in some cases causes more economic destruction and human loss of life than from the primary earthquake shaking. Notable examples include the 1994 Paez, Colombia (Forero-Duenas; 1996) and 1997 Ardebil, Iran (Bird and Bommer; 2004) earthquakes. The Paez earthquake was an M6.4 earthquake that triggered a large debris flow, which killed 1,100 people (Forero-Duenas; 1996). The M7.4 Ardebil earthquake caused multiple landslides, some of which covered entire villages (Ishihara et al.; 1992). Earthquake-induced landslides can also set in motion an extended chain of surface processes and hazards, including persistent landslides and debris flows, dammed rivers, sediment aggradation and floods in the days, months, and years following the initial seismic event (Fan et al.; 2019). Despite recent advances in our understanding of earthquake-induced hillslope failures, important questions remain regarding their expected number, size, distribution, and failure styles (e.g., Meunier et al. (2008); Marc et al. (2016); Croissant et al. (2019); Valagussa et al. (2019); Medwedeff et al. (2020)), as well as the longer-term effects on hillslope geomorphology and sediment transport (e.g., Wartman et al. (2013); Croissant et al. (2019); Campforts et al. (2020); Francis et al. (2022)).

Landslide properties, such as location and volume, are often coupled to the ground motion characteristics of the related earthquake (e.g., Jibson (1985)). Thus, studies of earthquake-induced landslides can also yield important paleoseismic information of past earthquake shaking (Jibson; 1985). One useful method for looking for past earthquake-induced landslides is by finding a cluster of related landslides in space and time (Crozier et al.; 1995). More recent studies suggest that the distribution of these landslide clusters can reveal patterns about where and when earthquake-induced landslides tend to occur in an area, as well as the seismic properties of the earthquake (Tanyaş et al.; 2018; Wang et al.; 2020; Rasanen and Maurer; 2021). For example, Rasanen and Maurer (2021) propose

a statistical approach that inverts probabilities of rupture location and magnitude from regional landslide evidence. Models of hillslope failures based on predictions of ground shaking intensity from 3D earthquake simulations (Allstadt et al.; 2013; Grant; 2017; Pollock et al.; 2019) may also yield insights into paleoseismic rupture parameters, especially when compared to patterns in documented landslide inventories.

Many of the approaches described above are improved as the number of landslides with an estimated age in an inventory increase. However, it is difficult to estimate the age of many landslides in a large inventory, and thus while studies of landslide geochronology (e.g., Aylsworth et al. (2000); Brooks (2013)) are effective, these studies have also been somewhat few, especially the further back in time the earthquake occurred. Moreover, although it is increasingly common to develop a landslide inventory following a modern earthquake in locations where seismometers characterize the ground motions and earthquake properties (e.g., Tanyaş et al. (2018)), it is much less common and more difficult to identify the cause of prehistoric landslides. Attempts at tying past landslides to seismic triggers typically involve geochronological dating that shows the landslide and earthquake were coincident, or slope stability models demonstrating that the landslide would never have failed unless there was seismic forcing (e.g., Jibson (1996); Schulz et al. (2012)). This difficulty of studying older earthquake-induced landslides means that although we have a better understanding of earthquake-induced landslides in areas with large recent earthquakes (e.g., Aylsworth et al. (2000); Brooks (2013)), other areas with infrequent earthquakes remain ambiguous.

In this paper, we use the spatial and temporal patterns of landslides in the greater Seattle, Washington area of the USA to better understand past earthquakes on the Seattle Fault zone, a crustal fault that ruptures through this region. First, we present a newly mapped deep-seated landslide inventory of the Puget Lowland of Washington, a well-populated region that includes the city of Seattle and is notorious for landslide susceptibility and multiple drivers of hillslope instability (Tubbs; 1974; Coe et al.; 2004; Baum et al.; 2005; Schulz; 2007; Harp et al.; 2008; Davis et al.; 2022). Next, we apply a recently established method to estimate the ages of these landslides based on their surface roughness (LaHusen et al.; 2016, 2020; Booth et al.; 2017). This method permits rapid assessment of the timing of thousands of deep-seated landslides on a regional scale. With this landslide inventory, we

assess spatial and temporal landslide clustering as evidence of the last major Seattle Fault earthquake, which ruptured to the surface around 1050–1020 cal yr. BP (Bucknam et al.; 1992; Atwater; 1999; Sherrod; 2001; Nelson et al.; 2014). We then compare this clustering to a suite of simulated M7.0 earthquakes on the Seattle Fault (Stone et al.; 2022) to explore possible earthquake characteristics, including regions of strong ground motion, based on the landslide record.

2.2 Puget Lowland Study Area and Background

Seattle and the surrounding area lie within the Puget Lowlands of Washington, USA (Figure 2.1), a region where landslides pervade the landscape (Laprade et al.; 2000; Survey; 2020). High regional landslide susceptibility stems from the many steep slopes underlain by weak glacial material (Tubbs; 1974; Schulz; 2007; Perkins et al.; 2017), a wet maritime climate, proximity to earthquake-producing faults, and human activity. Compilations of historical landslides (Laprade et al.; 2000; Survey; 2020) show a predominance of precipitation-induced landslides in this region. Recorded landslides have been paired with complementary precipitation data to estimate rainfall and soil moisture conditions that lead to shallow slope failures in Seattle (Baum et al.; 2005; Godt et al.; 2006). New Bayesian modeling of landslide inventories indicates that the highest probability of precipitation-induced landslides occurs in January or February, just after the annual precipitation peak (Luna and Korup; 2022).

In contrast to precipitation-induced landslides, earthquake-induced landslides are much less frequent or predictable in this area. In fact, no large ($\geq$M5) earthquakes on surface faults in the Puget Lowlands have happened during the modern record (1900-2023). The few earthquakes that have occurred in the historical record (1900-2023) were deep intraslab earthquakes with strong, but not severe, ground motions (Peak Ground Velocity [PGV] $\leq$ 50 cm/s). The most recent of these was the 2001 M6.8 Nisqually earthquake that induced few landslides in the region (Highland; 2003). However, significantly more landslides are expected for M 9 Cascadia subduction zone (CSZ) earthquakes, and more still from ruptures near the surface on crustal faults (Grant; 2017). Here we focus on the Seattle Fault (also known as the Seattle Fault Zone [SFZ]), a crustal fault zone running through the City of

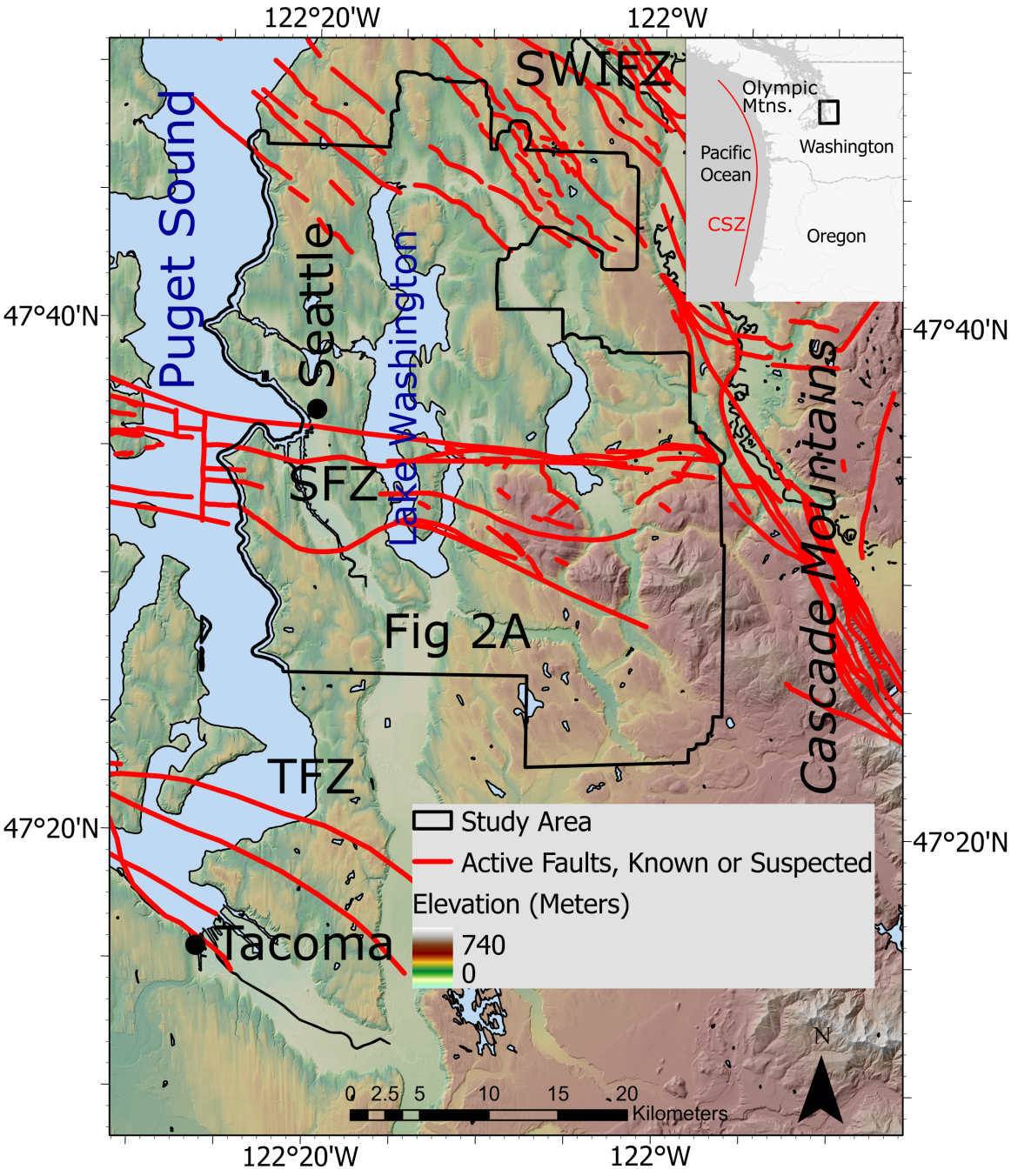

Figure 2.1: Shaded-relief map of the Puget Lowlands, highlighting the study area. The black outline shows the region of mapped landslides, shown in Figure 2.2, and the red lines are mapped active faults. TFZ is the Tacoma Fault Zone, SFZ is the Seattle Fault Zone, and SWIFZ is the southern Whidbey Island Fault Zone (SWIFZ).

Seattle (Figure 2.1) with a recurrence interval for a full rupture on the SFZ of longer than 6,500 years (Sherrod et al.; 2000). Other earthquakes recorded with paleoseismic data in the Seattle Fault Zone occur more frequently and are still large enough (M6.5–7) to induce landsliding (Nelson et al.; 2003, 2014; Karlin et al.; 2004). The Seattle Fault Zone is one crustal fault of several in the Puget Lowlands fault inventory that also includes the southern Whidbey Island Fault (Johnson et al.; 1999, 2004; Sherrod et al.; 2008) to the north and the Tacoma Fault (Brocher et al.; 2001; Sherrod et al.; 2004) to the south (Figure 2.1).

The Seattle Fault is an active south-dipping crustal reverse fault within the forearc of the CSZ that trends east-west for 60–65 km across the Puget Lowlands (Johnson et al.; 1999; Blakely et al.; 2002)(Figure 2.1). The locations, orientations, and dip of Seattle Fault splays are poorly constrained (e.g. Pratt et al. (1997); Johnson et al. (1999); Brocher et al. (2001); Brink et al. (2002); Moore et al. (2022)). The three main fault strands of the SFZ are blind (Johnson et al.; 1999; Blakely et al.; 2002); however secondary backthrusts within the hanging wall of the main structure break the surface, forming Holocene fault scarps (Nelson et al.; 2003, 2014; Kelsey et al.; 2008). The current best estimate, derived from dendrochronology, of the last major Seattle Fault Zone earthquake is that it occurred in the winter of 1,093–1,092 yr B. P. (Black et al.; 2023) and had an estimated magnitude of 7–7.5 (Brink et al.; 2006; Styron and Sherrod; 2021). This earthquake triggered regional uplift (Bucknam et al.; 1992) and a tsunami in the Puget Sound (Atwater and Moore; 1992). The Seattle Fault also had at least one more recent earthquake, and possibly several others. Nelson et al. (2014) identified earthquake "NE", at 940–380 cal. B.P. and Angster et al. (2022) identified earthquake "RH2" at $\leq$530 cal yr. B.P. These earthquakes were likely only partial ruptures and were smaller than the earthquake that occurred 1,000 years ago. In the last 4,000 years, the Seattle Fault has also had at least two older earthquakes: earthquake "RH1", 1,330 cal. B.P. (Angster et al.; 2022), earthquake "NC", 1,310–1,200 cal. B.P. (Nelson et al.; 2003, 2014) and earthquake "NB", 2,650–1,940 cal. B.P. (Nelson et al.; 2003, 2014). These earthquakes likely had magnitudes around M 7 (Nelson et al.; 2003, 2014).

Landslide deposits within Lake Washington (Jacoby et al.; 1992; Karlin et al.; 2004), as well as within the Olympic Mountains to the west (Schuster et al.; 1992), along with oral histories of Seattle Fault-associated ground failures (Ludwin et al.; 2005), implicate

a strong landscape response to earthquakes in the region. The full impact of earthquake-induced ground shaking on hillslopes from past Seattle Fault earthquakes, however, remains poorly resolved. Allstadt et al. (2013) modeled where future landslides might occur using a single-scenario Seattle Fault earthquake simulation. This work was useful for revealing how site and basin amplification may control where earthquake-induced landsliding occurs in the Seattle area, leading to increased landslide rates in the Seattle basin and in areas with unconsolidated sediments. They also found that higher ground saturation (100% vs 0% saturation) would lead to about an order of magnitude more landslides.

Using a similar methodology, Grant (2017) analyzed the hillslope response to simulated CSZ megathrust earthquakes and found that an earthquake on the Seattle Fault would likely cause more landslides in the Seattle area than a CSZ earthquake.

The findings of Allstadt et al. (2013) and Grant (2017) have yet to be vetted against a record of past landslides due to limited information about the timing or cause of the thousands of discrete, deep-seated landslide deposits that exist within the landscape. By mapping, dating, and characterizing spatial patterns of the deep-seated landslides, we improve our understanding of the distribution of earthquake-induced landslides in the area. Additionally, we compare our landslide inventory to a new suite of Seattle Fault earthquake scenario simulations (Stone et al.; 2022), to assess possible earthquake properties of past earthquakes on the Seattle Fault.

2.3 Methods

2.3.1 Landslide Mapping and Dating

Using high-resolution (1 m) lidar data, we mapped over 1,000 deep-seated landslides in the Puget Lowlands area (Figure 2.2, Table 2.4). Throughout the rest of this paper, when we refer to landslides from this inventory, we are specifically referencing deep-seated landslides, those in which the slide plane lies below the roots of trees. Such deep-seated landslides are often categorized as rotational or compound landslides using the classification system of Hungr et al. (2014). Landslide deposits were mapped from bare-earth lidar imagery based on the presence of headscarps, many of them arcuate, upslope of hummocky terrain

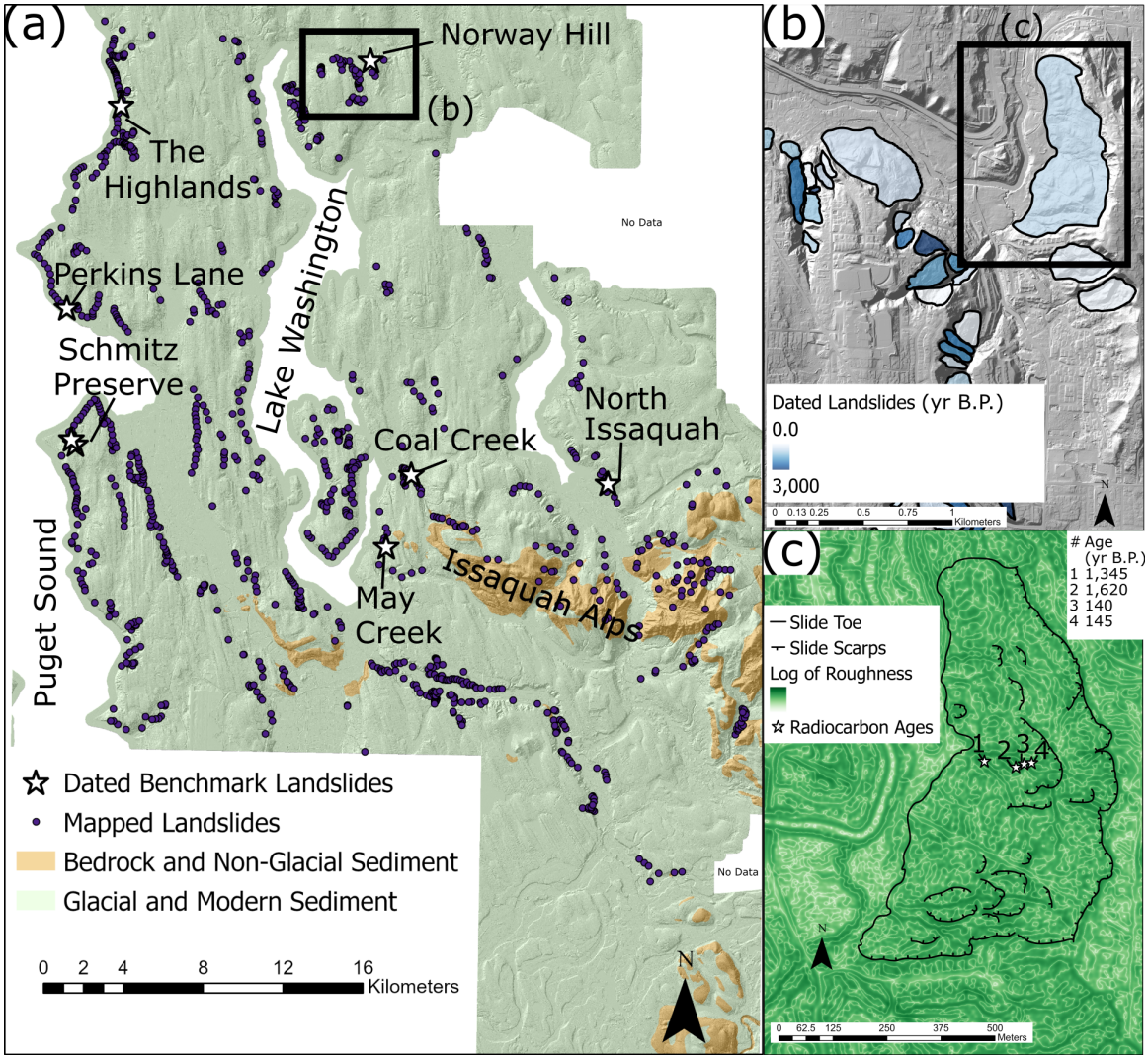

Figure 2.2: Landslide inventory maps. (a) Lidar hillshade map with all mapped deep-seated landslides from this study as circles and benchmark (dated) landslides as stars. The map is colored based on whether the surface geologic unit is glacial, modern, or bedrock (Yount et al.; 1993). (b) Lidar hillshade map with a subset of mapped landslide areas colored by roughness-based age. See panel (a) for location. (c) Roughness map showing landslide toe and scarps of a benchmark landslide. Radiocarbon sampling locations are numbered and shown with stars; corresponding mean ages are in a table in the top right corner. See panel (b) for location.

(Figure 2.2). Previous mapping by Washington Geological Survey geologists was used as a reference point (Survey; 2020). Lidar data were used to calculate properties of these mapped landslides, such as height (from headscarp to deposit toe) and length of the landslide. Field observations, including stratigraphy and morphology assessments at some of the landslides, confirmed the accuracy of the remote mapping. Field observations were combined with lidar-based mapping to create detailed morphology maps of a selection of benchmark landslides that were dated using radiocarbon ages (Figure 2.2c).

To provide age information for our full catalogue of landslides, we applied a recently developed method based on the age-calibrated roughness of landslide deposits (LaHusen et al.; 2016; Booth et al.; 2017). The premise behind this method is that the ground surface roughens significantly from mass movement. As a result, landslide deposits exhibit their highest roughness just after failure and smooth by diffusive hillslope processes over time (e.g. Figure 2.10). This smoothing can be modeled as an exponential age-roughness relationship (Figure 2.3). Calibrating this relationship for the field site requires measured roughness values for each landslide deposit and several benchmark landslides of known age. The lidar we used was collected in 2016, so here this roughness method provides an age before 2016. For this reason, when analyzing and discussing landslide timing within this paper, we use yr B. P. starting at 2016.

Following Booth et al. (2017), we measured landslide roughness using a 15 m Ricker wavelet Ricker (1943) transform, often known as a "Mexican hat" wavelet, on the lidar elevation data of the landslide deposit (Booth et al.; 2009, 2017; LaHusen et al.; 2020). This wavelet was scaled so that it measures topographic curvature as a function of length scale (Kumar and Foufoula-Georgiou; 1997; Lashermes et al.; 2007; Booth et al.; 2017). We used a 15 m scaled wavelet based on work by Booth et al. (2017) showing that this length scale best characterized landslide age in a similar topographic, climatic, and sedimentologic setting north of our study area. We excluded areas of the deposit within 8 m of places that have been altered in ways not modeled by simple soil diffusion, such as gullies or roads. Gullies were identified as areas with a concave-up profile curvature of $\geq 0.09 m^{-1}$ and with a drainage area of $\geq$2,670m^2 calculated using a D-infinity flow accumulation algorithm as done in Booth et al. (2017). Landslide roughness may vary as a function of failure style, relative

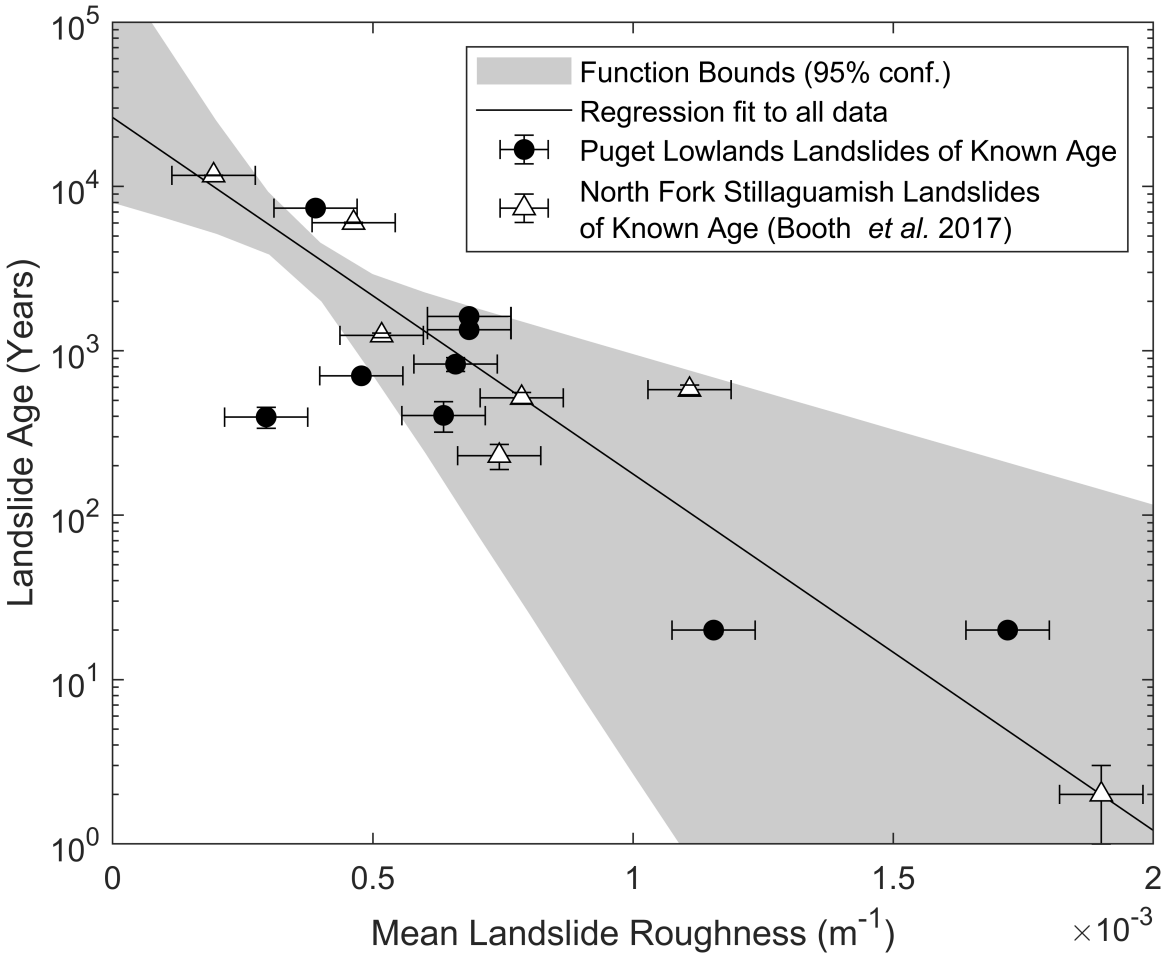

Figure 2.3: Age-roughness relationship for the Puget Lowlands. Previous data from the North Fork Stillaguamish Valley (Booth et al.; 2017) are shown as triangles and new data from landslides from the Seattle region of the Puget Lowlands (this study) are shown as circles. The exponential fit to data from both datasets is plotted as a black line with the shaded area indicating uncertainty on this fit (95% confidence bounds). Uncertainty was calculated by varying input data based on their error and refitting the exponential fit, the gray area then shows where 95% of these functions cover.

activity, or material properties (McKean and Roering; 2004; Goetz et al.; 2015; Booth et al.; 2009, 2017). To minimize these effects, we considered only deep-seated rotational landslides within similar glacial materials. By controlling for landslide type and parent material, we assume landslide deposits included in this study will be governed by similar diffusive relationships. Landslides mapped as failing in different styles, or from different parent materials were excluded from this study. Some mapped landslides are also active, with many landslides exhibiting reactivation. For consistency, we map complex landslides as a single slide. Although the error on the age for a single landslide is high, making it difficult to definitively estimate the age of a single slide, the quantity of landslides with estimated ages allows for studying large-scale patterns.

To establish newly-dated benchmark landslides to calibrate the roughness model, we used radiocarbon dating of organic material embedded in the landslide deposits. We targeted streams incised into landslide deposits to collect nine pre-modern (pre-1950) samples of wood and other organic debris. We only took samples that were entrained within the landslide deposit to minimize the chance that they are not associated with the main landslide failure. Radiocarbon dating is well suited to the landslides of the study area, since abundant vegetation is likely to be preserved in landslide deposits, but it does have some disadvantages (Pánek; 2015). For example, many landslides are part of large landslide complexes that have failed many times. These reactivations can contain both new material and older material from past landslides, and as such, their radiocarbon ages can be difficult to interpret. Additionally, sample material such as charcoal can be older than landslides that contain it (Struble et al.; 2020). To reduce this uncertainty, we collected multiple samples when possible. By comparing these ages, as well as looking to lidar to identify crosscutting relationships (Ramsey; 2009), we constrain the ages of some of these landslides to a smaller range than that provided by just a single sample. These samples were dated using accelerator mass spectrometry (AMS), performed by DirectAMS. Calibrated ages were derived using OxCal v4.3.2 (Ramsey; 2017) with IntCal13 (Reimer et al.; 2013).

We combine radiocarbon data from the North Fork Stillaguamish (LaHusen et al.; 2016; Booth et al.; 2017), which lies in a similar climate to the Puget Lowlands and has similar Quaternary glacial deposits, with the newer Puget Lowlands landslide ages to develop the

age-roughness relationship that we use in this study: $t = 26,298e^{-4,994r}$ where t is the time in yr B. P. and r is the roughness in m^{-1} (Figure 2.3). We then use this function to estimate the age of all landslides in our inventory. The final ages are subject to multiple sources of uncertainty. The radiocarbon ages have error based on both the radiocarbon dating and the time that passed between wood growth and entrainment into the landslide deposit. The roughness measurements themselves are variable based on the lidar data quality, and may differ between landslide styles. These sources of error are then incorporated into uncertaintity of the age-roughness relationship (gray area in Figure 2.3) and thus the final landslide ages.

2.3.2 Landslide History Models

We adapt a landslide history model developed by LaHusen et al. (2020) to assess the main causes of landsliding in the area from 4,600 yr B. P. to present day. This model considers the effects of variable initial landslide deposit roughness on the roughness-based age calculation, as well as the effect of preservation bias. It produces a count of landslides in a given area over time. This helps us understand if the variations we see in the landslide chronology are the result of natural variation, bias and error, or if there is an underlying signal. Due to the uncertainty of the roughness ages and the nonlinear relationship between roughness and age, an earthquake is unlikely to be represented by a sharp peak in landslide frequency, but instead by a broad peak (LaHusen et al.; 2020). We can model this sort of broad peak and compare it to the landslide inventory to test if it is present in our data. We used two model setups and compare these to the observed landslide history: one with steady landslides and one that also included pulsed landslides. The model pair allows us to consider the possible impacts of earthquake-induced landslides on the landslide record. For each model, we ran 10,000 simulations to explore the possible range of starting roughness values. A baseline annual landslide rate was used to approximate landslides caused by precipitation and other landslide triggers in the steady model. It is worth noting that precipitation-induced landslides are not actually constant through time, but stochastic and likely subject to a heavy-tailed distribution of inter-event times (e.g. Sadler (1981); Schumer

and Jerolmack (2009)). Although the low precision of the landslide ages should mitigate the error from a steady assumption, this does represent a potential source of unmeasured error. This baseline rate was also included in the earthquake-pulse model, which added an additional earthquake-induced landslide factor modeled as a pulse of landslides observed at the time of the last major earthquake on the Seattle Fault (1,100 yr B. P., Sherrod et al. (2000)).

Other earthquake sources have produced earthquakes that likely impacted the study area during this time period, most notably several M 9 CSZ earthquakes (Goldfinger et al.; 2012). While these M 9 earthquakes may have induced landslides in the study area, this earthquake signal is not easily identified due to uncertainty in the landslide dating method and the frequency of earthquakes (LaHusen et al.; 2020). For this reason, we focus on the Seattle Fault, which is most proximal to the study area, ruptures to the surface, and has a longer recurrence interval such that landslide signals from each earthquake do not overlap. Additionally, the overlapping signals from M9 earthquakes should not disrupt our ability to measure signals from a Seattle Fault earthquake because they are implicitly included in the background landslide rate. The upper age limit of 4,600 yr B. P. and 200-year bins were chosen by limiting our focus to bins that contain at least 5 landslides. Because we are only considering the last 4,600 years and the last major shift in climate in this area occurred 6,000 yr B. P. (Cwynar; 1987), we assume that the climate, and thus the baseline background landslide rate, remained relatively consistent during this period and would have had a less significant impact on the landslide history than earthquakes. However, we are not restricting the ages used to calibrate the age-roughness relationship (which include ages up to 10,000-years) and thus a change in climate may be a source of uncertainty in our age-roughness relationship. Preservation bias is modeled as an exponential function fit to the landslide frequency derived from the inventory. This bias is multiplied by the modeled landslide frequency to show what might be observed in a real world landslide inventory.

In addition to landslide frequency through time, we also model landslide areas using a power law relationship $p(x) \propto x^{\alpha}$, where α is an exponent derived from the frequency-area distribution of the landslide inventory, p is the probability of occurrence, and x is the area of the landslide, as developed in Tanyaş et al. (2018). We do this using the methods described

	Slip Distribution #1	Slip Distribution #2	Slip Distribution # 3
West Hypocenter	Scenario 1	Scenario 4	Scenario 7
Central Hypocenter	Scenario 2	Scenario 5	Scenario 8
East Hypocenter	Scenario 3	Scenario 6	Scenario 9

Table 2.1: Table of water table regression parameters for both winter and summer conditions

in A. et al. (2009). This provided a power law exponent of -1.8 with a cutoff at 6,600m^2. Landslide frequency-area distributions are known to only follow a power law at larger areas, while smaller landslides below a rollover point do not (e.g., Malamud et al. (2004); Frattini and Crosta (2013)). To avoid issues with modeling this rollover point, we conservatively only simulate landslides with areas $\geq$9,000m^2.

The two landslide history models described above, one background steady-state model and one earthquake (pulsed) model, were tuned to match the total number of landslides in the mapped landslide inventory. This tuning was done to minimize the error between the model and the inventory (Figure 2.11). We restricted this tuning to the modeled window of 400–4,600 yr B. P. to remove the effect of apparent increase of landslides in the past 400 years. The resulting number of landslides is different than the total number of landslides created by the model because of preservation bias, which has been noted in similar studies (LaHusen et al.; 2016, 2020; Booth et al.; 2017).

2.3.3 Seattle Fault Earthquake Simulations

We use nine simulations of Seattle Fault earthquakes to compare landslide clustering to modeled ground motions and use these comparisons to invert for reasonable ground motion characteristics of the last major earthquake on the Seattle Fault (1,100 yr B. P.). The ground motions we use are peak ground velocities (PGVs) from nine different M7 scenario earthquakes on the Seattle Fault (Figure 2.4) (Stone et al.; 2022). We use PGV instead of peak ground acceleration (PGA) due to limitations of the simulations for producing accurate PGA values. These models incorporate the effects of topographic amplification

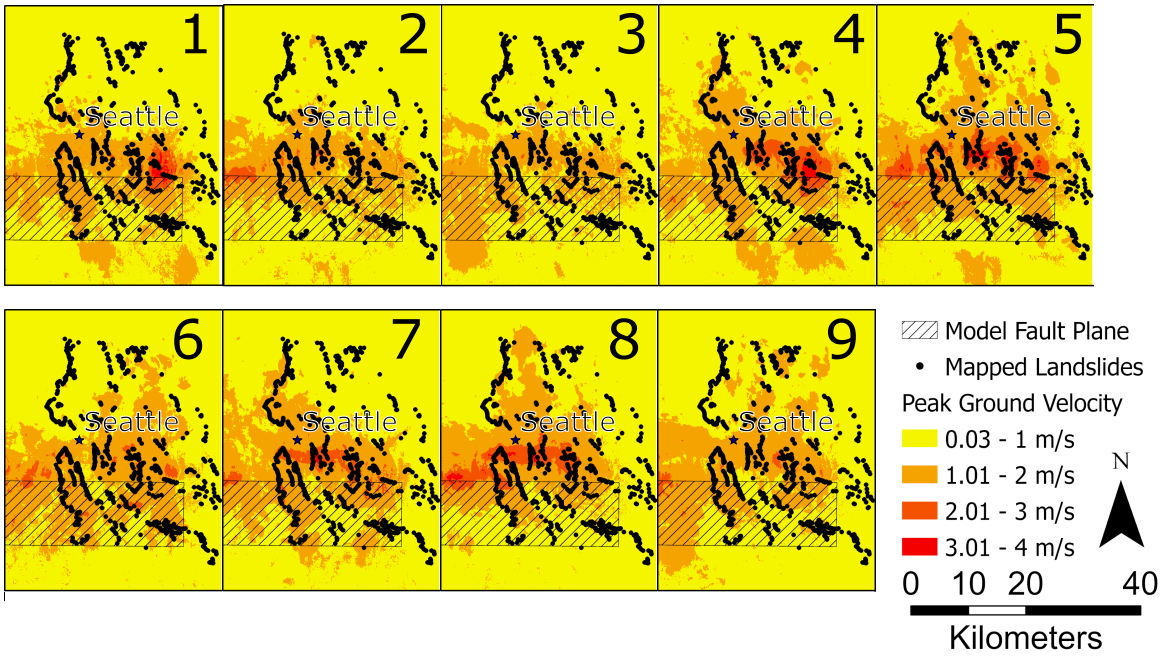

Figure 2.4: Ground motions in PGV for each Seattle Fault earthquake scenario (1–9). Higher ground motions are indicated with red and orange; lower ground motions in yellow. The landslide inventory is shown as points and the modeled fault plane location shown as a cross-hatched rectangle.

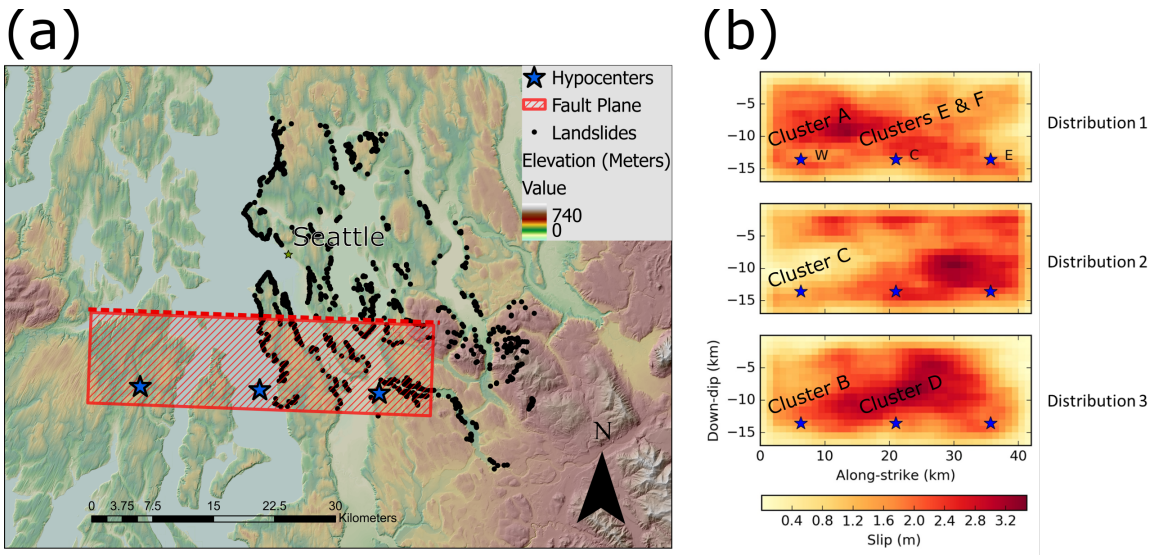

Figure 2.5: Properties of considered earthquake scenarios. (a) Shaded relief map with scenario fault plane (red) and hypocenter locations (blue stars) with mapped landslide inventory shown as black points. (b) Slip distributions and hypocenter locations (stars, W = west C = central E = east) for all scenarios (Adapted from Stone et al. (2022)). Best-fit scenarios for different temporal landslide clusters (A – F) are highlighted (see results, discussion, and Figure 2.9 for details).

as well, an important element for understanding landslide initiation. The nine different rupture scenarios we consider (Table 2.1) are based on a combination of three different slip distributions (Figure 2.5) and three different hypocenter locations (East, Center, and West), as described in detail by Stone et al. (2022). The three slip distributions were randomly generated but can roughly be described as slip concentrated in the east (distribution 1), in the west (distribution 2), and in the central portion of the rupture (distribution 3).

The spatial distribution of observed landslides among different PGVs from the Seattle Fault earthquake simulations is measured using a probability density function (PDF) created using a kernel density smoothing function. First, two probability density functions were created, one for the occurrence of landslides P(Landslide) and another for the distribution of PGVs P(PGV). We also create a conditional probability of PGVs in areas with landslides P(PGV—Landslide). Using Bayes' theorem, we can then calculate the probability of landsliding at a given PGV P(Landslide—PGV). To consider areas that landslides are likely to occur, these distributions were derived only for areas with slopes higher than 10 degrees. This cutoff was chosen based on proportionally less landslides occurring on slopes $\leq$10 degrees (Figure 2.12). PGV distributions were based on median PGV values from all scenarios, to avoid being skewed by a single scenario with a high PGV at any given location; though, a mean PGV based analysis produces similar results. The spatial distribution of these median peak ground motions is shown in Figure 2.6, along with the landslide inventory. We exclude the higher PGV values where $P(PGV) \leq 0.1$, because the low sample sizes at these values lead to misleading statistics. We also calculated the conditional probability P(Landslide—DistanceFromFault) in a similar manner, finding the probability of landsliding given a 3D distance from the modeled fault plane. We perform these measurements for both observed landslide count and observed landslide area. Landslide area weights the statistics, so that larger landslides have a larger effect on the probabilities.

To test for spatial clustering of landslides based on earthquake shaking (PGV), or distance to rupture, we use a two sample Kolmogorov–Smirnov (K-S) test. This technique tests if two sample sets are drawn from the same nonparametric continuous probability distribution (Massey Jr; 1951). In our case, we compare the background distribution of PGV, representing earthquake shaking intensity, across all landslide-susceptible areas within our

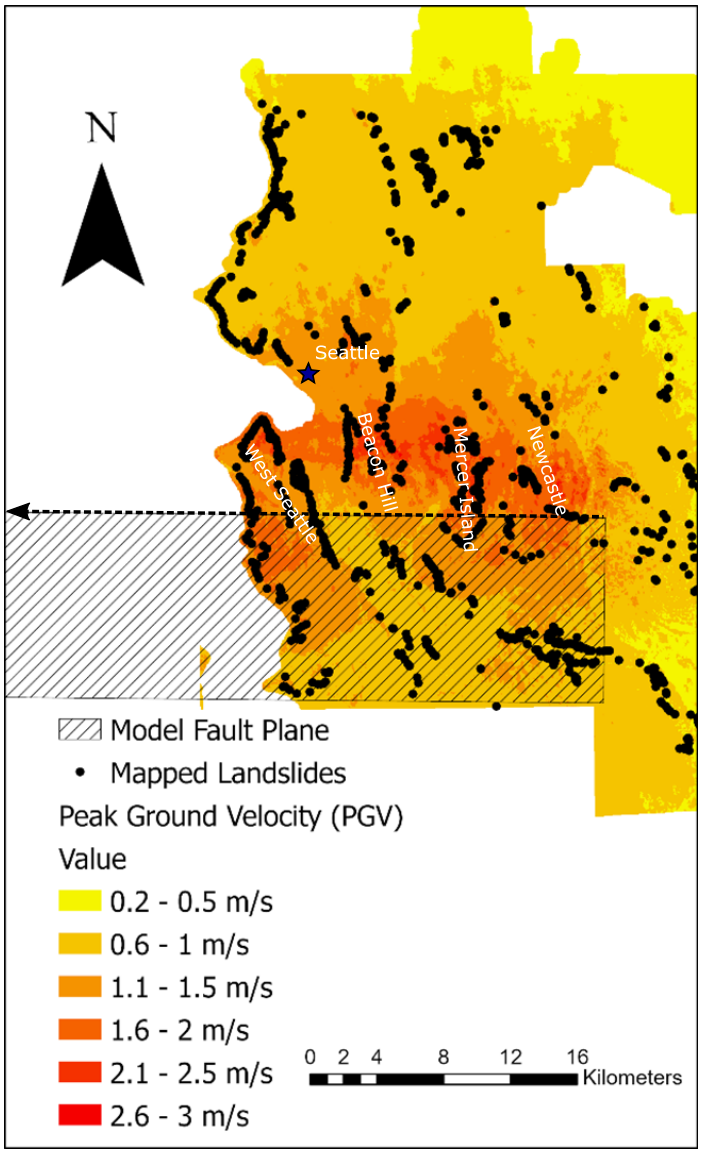

Figure 2.6: Peak ground velocity (PGV) map for the study area based on median maximum horizontal ground motions from all earthquake model scenarios. Mapped landslides are shown as points. The fault plane is shown as the hatched area, with a dashed line showing the surface trace of the fault. The arrow indicates that the fault trace and plane continue to the west out of the frame.

study, to the distribution of PGVs just within mapped landslide polygons. From global empirical observations (Keefer; 1984; Jibson; 1985; Malamud et al.; 2004), we assume areas of stronger shaking should promote more, and larger, landslides compared to areas of less shaking, and construct a null hypothesis to test that the distributions of PGV in both landslide and non-landslide points match. Given this assumption, we use the K-S test to identify two conditions: (1) the null hypothesis is rejected, and landslide polygons show a significant difference in PGV compared to background, or (2) we cannot reject the null hypothesis and landslides are not sensitive to high (or low) PGV values. K-S tests were performed on landslide distributions for a sequence of 200-year time periods from 0 – 4.6 ka using all nine Seattle Fault earthquake simulations. We hypothesize that during periods of local ground shaking due to Seattle Fault earthquakes (e.g., around the most recent 1,093–1,092 yr B. P. event, Black et al., in review), we will observe a strong clustering of landslides in high PGV regions and reject the null hypothesis, while in aseismic periods, we will observe more uniformly distributed precipitation-induced landsliding and will not reject the null hypothesis. We ran the K-S test two times for each time period, once measuring if the distribution of landslides correlated with ground motions, and once to see if the landslides exhibit an inverse relationship with ground motions. We use results from this test to interpret whether the landslides in each of these time periods were likely to be caused by ground motions from one of the scenario earthquakes. This is useful because even if a temporal cluster is caused by precipitation or another earthquake source (such as the southern Whidbey Island Fault), it will not show up in this test (i.e., the spatial distribution of landslides will not correlate with the likely spatial distribution of PGV from a Seattle Fault earthquake). In this way we can narrow the source of the landslide cluster to just those likely caused by a Seattle Fault earthquake. The inverse test, on the other hand, will not represent earthquake induced landslides. Instead, this test measures if there are more landslides in areas with low PGVs. Such a pattern could be expected if landslides that occur in the years after an earthquake are preferentially located in areas that did not fail during the previous earthquake.

Landslide Name	Material	Radiocarbon Age (yr. B.P)	1σ Error (yr)	Calibrated Ages[a] (cal. B.P) with 2σ Error	Latitude and longitude
North Issaquah Slide	Charcoal	903	22	830 ± 80	122°2'39.47"W 47°33'36.725"N
Schmitz Preserve N	Wood	382	23	405 ± 85	122°24'5.205"W 47°34'36.04"N
Schmitz Preserve E	Wood	6484	36	7,390 ± 70	122°23'57.341"W 47°34'27.28"N
Norway Hill	Wood	1463	24	1,345 ± 45	122°12'24.437"W 47°44'58.484"N
Norway Hill	Wood	1706	37	1,620 ± 80	122°12'20.92"W 47°44'58.089"N
Norway Hill	Wood	161	20	140 ± 140	122°12'20.102"W 47°44'58.356"N
Norway Hill	Wood	173	25	145 ± 145	122°12'19.215"W 47°44'58.452"N
Coal Creek	Charcoal	789	20	705 ± 25	122°10'16.695"W 47°33'41.193"N
May Creek	Wood	317	21	396 ± 58	122°11'25.899"W 47°31'49.360"N

Table 2.2: Benchmark Landslide Radiocarbon Ages. Additional information in Table 2.4.

[a]Calibrated ages from OxCal (4.3.2) using IntCal13 and are in years before 1950

2.4 Results

2.4.1 New Radiocarbon Ages

To develop our roughness relationship (Figure 2.3), we dated six benchmark landslides using AMS radiocarbon dating performed by DirectAMS (Table 2.2). Four ages are from the Norway Hill landslide complex (Figure 2.2). These ages, derived from samples of wood and other organic materials, were collected from exposed gullies running up the complex and were, in order from lowest to highest elevation sampling location: 1,345 ± 45, 1,620 ± 80, 140 ± 140, 145 ± 145 cal. B.P. Uncertainty on these and other dates is 2-sigma error. Based on crosscutting relationships observed from the lidar data, where younger landslides overlay older landslides, the youngest two ages likely represent a more recent secondary failure in the landslide complex, while the older two likely represent the initial age of the complex. For this reason, we use both older dates to calibrate the age-roughness model (Figure 2.3), but not the younger ages. While these ages do not overlap in error and may represent separate failures, they are close enough that excluding either does not significantly change the age-roughness fit.

We also obtained two ages from wood buried in individual landslides in the Schmitz Preserve, with ages of 405 ± 85 and 7,390 ± 70 cal B.P. for landslides in the northern and eastern parts of the preserve, respectively (Figure 2.2a). We also obtained one age from wood exposed in a gully near May Creek (Figure 2.2a), which gave an age of 396 ± 58 cal. B.P for that landslide. Two additional charcoal ages were obtained from landslides near North Issaquah (830 ± 80 cal. B.P.) and Coal Creek (705 ± 25 cal. B.P.) (Figure 2.2a). Owing to long preservation times, charcoal is more likely to provide a maximum age constraint than an absolute age. However, based on the relatively young ages recorded here, we used these to calibrate the age-roughness relationship. Finally, to consider the youngest possible ages, we use landslides that occurred during the winter of 1996–97 at Perkins Lane and near the “Highlands” (Figure 2.2a) (Baum et al.; 1998).

2.4.2 Landslide Inventory

We mapped 1,064 deep-seated landslides in the study area (Table 2.4). GIS polygons of our mapped landslide inventory are available as a shapefile with the supporting information. Some of these landslides are part of slide complexes with multiple successive failures. Individual landslides range in area from $300m^2$ to $530{,}000m^2$, with a mean landslide size of $18{,}000m^2$. The height-to-length ratios (height is measured as base of headscarp to end of toe) of the landslides range from 0.03 to 4, with a mean height-to-length ratio of 0.5. The landslides generally occurred along the steep slopes of the area, such as waterfront bluffs and river valleys (Figure 2.2a) and overlap with areas predicted to fail in a Seattle Fault earthquake by Allstadt et al. (2013) and Grant (2017). We did not map bedrock failures in the Issaquah Alps (Figure 2.2a), which explains the dearth of landslides from that region in our inventory.

The landslide inventory ages, derived from roughness, reflect an exponential preservation bias, with more landslides having younger ages owing to the erosional removal and overwriting of older landslide deposits (Table 2.4, Figure 2.7). This appears as a linear relationship in the semi-log plot in Figure 2.7. However, there are even more landslides at younger ages than this bias would predict, with a large increase in landslides with ages younger than 400 yr B. P. This may be an artificial increase due to the "Sadler effect" (Sadler; 1981; Schumer and Jerolmack; 2009), where changing the sampling window can artificially increase measured rates of stochastic events (see appendix and Figure 2.13 for more information on this effect). Beyond the expected preservation bias and Sadler effect, there are additional fluctuations in the number of landslides through time, such as around 1.0 ka and 2.6 ka (Figure 2.7).

2.4.3 Modeled Landslide Histories through Time

The results of the roughness-based landslide models through time are shown in Figure 2.7 and compared to the inferred frequency of landslides from our inventory (black line). Because these models only consider landslides $\geq 9{,}000m^2$, the landslide inventory is similarly filtered to provide an appropriate comparison. The steady model has a landslide rate of

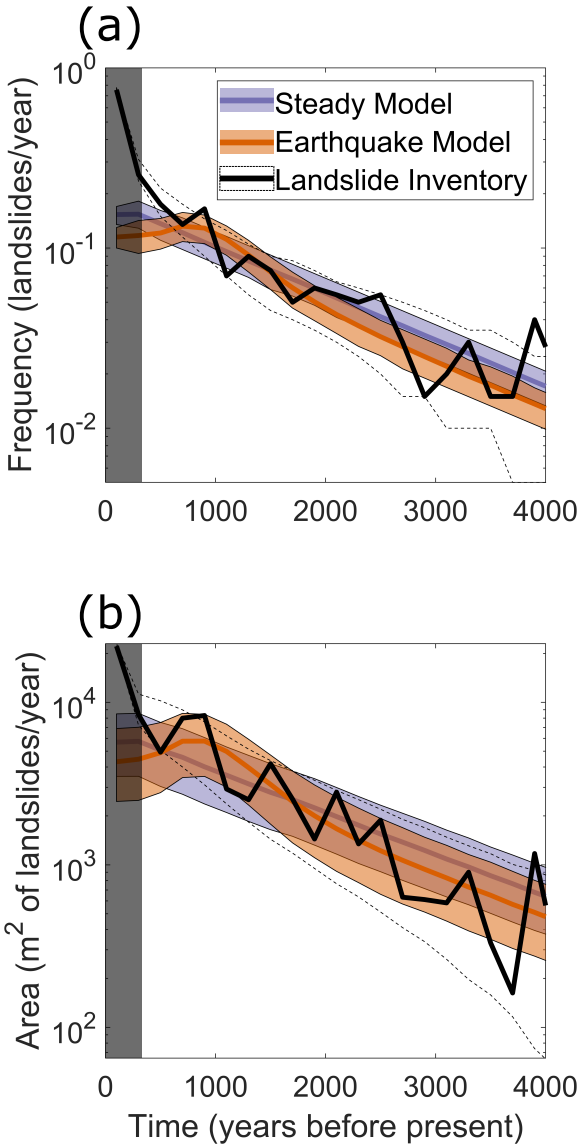

Figure 2.7: Landslide frequency (a) and area (b) over time. The black line represents the mapped landslide inventory, 2σ error in dashed lines. The dark gray vertical bar over the most recent time interval indicates the anomaly, possibly due to the Sadler effect, that is not considered during modelling. The blue line and shaded area represent the model with a uniform landslide rate. The orange line and area represent the model with an increase in landslide frequency and area around the time of the last major earthquake on the Seattle Fault. The lines indicate the mean values, and the shaded areas represent 90% of model runs. See methods section for scenario model details.

16 landslides per 100 years. The best-fit earthquake (pulsed) model has a landslide rate of 12 landslides per 100 years with 80 additional landslides induced by simulated representation of the last major Seattle Fault earthquake. Both of these best-fits are determined by minimizing root mean squared logarithmic error (RMSLE) between the modeled frequency distributions and the observed landslide distribution.

Although the earthquake-induced landslide model produces an overall similar pattern to the steady landsliding model, it does do a better job of fitting some of the observed variations in landslide frequency and area. Based on comparing the frequency distributions of the models to the observations, the earthquake model has a RMSLE of 0.018 while the steady model has a RMSLE of 0.078. For the area distributions, these errors are 0.54 and 2.8, respectively. In particular, the earthquake landslide model fit is better around the time of the last major Seattle Fault earthquake 1,100 yr B. P. in the area distribution. Although the fit is also slightly better for the earthquake model in the frequency distributions, it is less robust. Both models fail to capture a cluster in landsliding around 2.6 ka and 3.8–4.6 ka, possibly related to other Seattle Fault earthquakes (Nelson et al.; 2003; Karlin et al.; 2004). These peaks might be better characterized by a model with landslides induced from those earthquakes. We did not try to replicate the substantial increase in modern landsliding observed in the last 400 years. This cluster may be a result of the Sadler effect (Sadler; 1981; Schumer and Jerolmack; 2009), see appendix and Figure 2.13.

2.4.4 Seattle Fault Earthquake Simulations and Spatial Landslide Patterns

Assuming that spatial correlations between landslides and PGV signify earthquake-induced landslides, we can use the spatial distribution of landslides to measure the likelihood that landslides were earthquake induced. Spatial patterns were first assessed by comparing landslide distributions to PGVs and distance to the fault. Although conditional landslide probability is proportional to distance from the fault and PGV, the relationship is stronger for PGV with higher maximum probabilities for both landslide count (conditional probability for PGV 0.144 $\geq$ conditional probability for distance 0.071) and area (conditional probability for PGV 0.116 $\geq$ conditional probability for distance 0.082) (Figure 2.14). As a result,

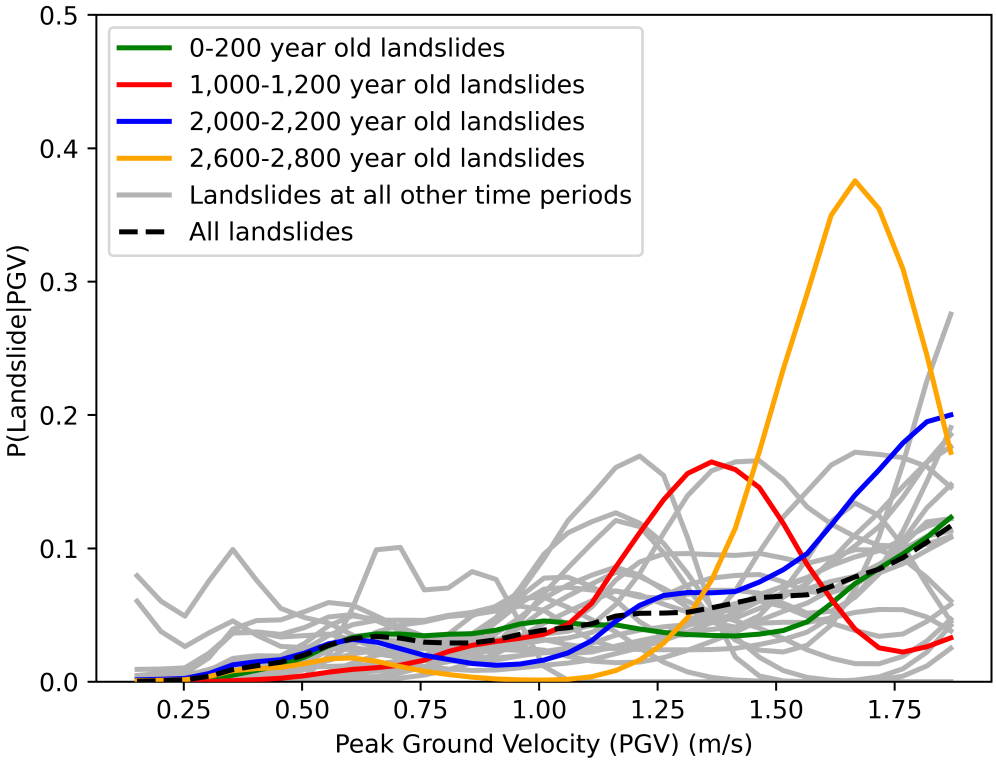

Figure 2.8: Conditional probability of landsliding as a function of peak ground velocity P(Landslides—PGV) at 200-year time slices. Highlighted time slices are in color: green for 0-200 yr B. P., red for 1,000-1,200 yr B. P. (time window that includes a known Seattle Fault earthquake), blue for 2,000-2,200 yr B. P., and yellow for 2,600-2,800 yr B. P. Other time slices from 4.6 – 0 ka are plotted in gray. The probability for the entire time period is plotted as a dashed black line. Peak ground velocity (PGV) is from the median of all earthquake scenarios in units of m/s. The 0–200 period represents a "null" scenario as no M7.0 earthquakes from faults in the region have been recorded, felt, or described during this time. The blue and yellow highlighted time slices have the maximum conditional probabilities.

we use PGV as the main indicator of earthquake-induced landslides. It should also be noted that P(Landslide—PGV) stops being a useful indicator at high PGVs ($P(PGV) \leq 0.1$) due to their low probability of occurrence. The distribution of P(Landslide—PGV) at different 200-year intervals is shown in Figure 2.8 (Figure 2.15 is similar, but uses mean PGV instead of median PGV). Highlighted in this figure are time periods that have higher than average correlations between landslides and PGV (blue and yellow lines), the time slice that includes the last known major Seattle fault earthquake (red line), and the "null" time slice of the last 200 years, a time window that we know did not experience a major Seattle fault earthquake.

Using the D statistics produced by two sample K–S tests, we compare the ground motions from different scenarios with the spatiotemporal distribution of landslides in Figure 2.9 and Table 2.3. The D statistic is a measure of how different the probability distributions of the two samples are, with higher values corresponding to greater differences. Above a critical value this statistic invalidates the null hypothesis that the two samples are from the same distribution. This critical value varies based on the input sample size but is on average 0.1 at a 99.9% confidence level for our dataset. Any value higher than this is considered statistically significant. We can additionally compare the values to get a relative measure of how well the distributions agree. To better compare variability in critical values among the different scenarios, Table 2.3 lists the D statistic divided by the corresponding critical value and Figure 2.9 summarizes this by finding the average normalized D statistic over all scenarios for each time period. We interpret values higher than 1 to indicate some earthquake-induced landslides, with higher values corresponding to a higher likelihood and proportion of earthquake-induced landslides. We plot (Figure 2.9) both the positive correlation (solid line with points) and inverse correlation (dashed line with points). The positive correlation between the landslides and PGV values represents earthquake forcing, whereas a lack of correlation or inverse correlation may represent landslides triggered by other forces. Inverse correlation additionally may suggest some sort of preconditioning of the landscape by earthquakes, causing landslides in areas other than those that failed due to shaking. Note that these values may not visually match the patterns shown in the conditional probability plots (Figure 2.8), because small number statistics can artificially

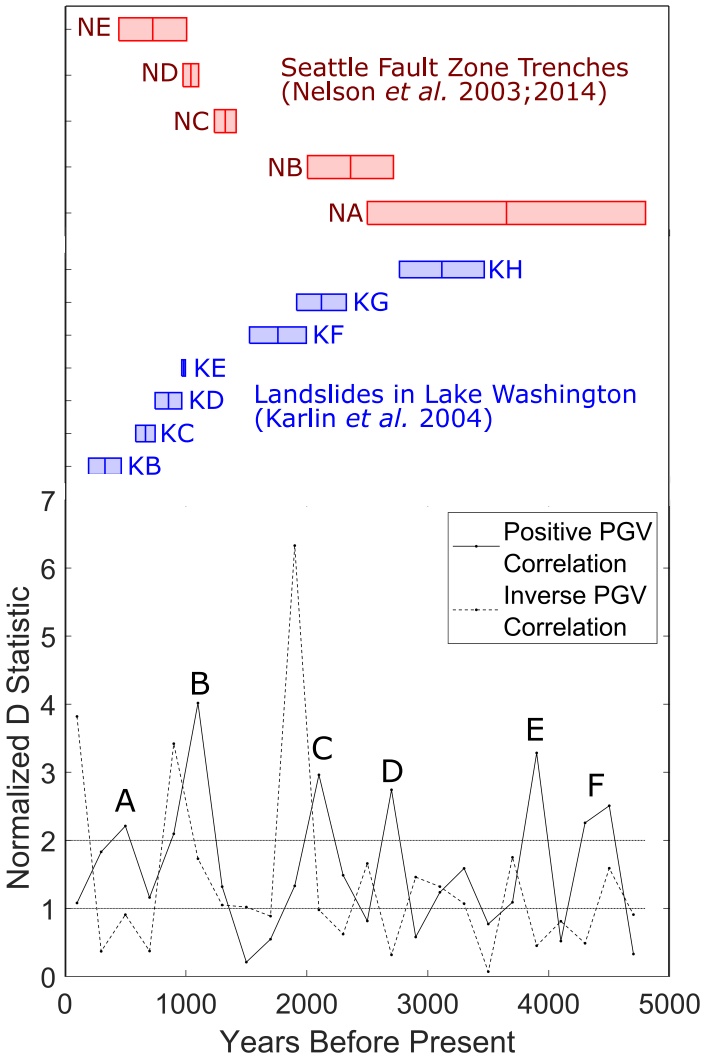

Figure 2.9: Plot showing the normalized D statistic (D statistic divided by the corresponding critical value, D statistic compares landslide distribution and PGV distribution) averaged over the nine earthquake simulation scenarios for each 200-year time interval through 4,800 yr B. P. Horizontal lines show values of 1 and 2. Values above 1 invalidate the null hypothesis and indicate earthquake forcing. Values above 2 have a higher probability of earthquake forcing and are used to designate possible earthquakes. These clusters are labeled (A-F); cluster B overlaps with the timing of the last major Seattle Fault earthquake. See text for details. For comparison, other earthquakes on the Seattle Fault (Nelson et al.; 2003, 2014) are plotted as red bars (labelled NA-NE) and landslide deposits in Lake Washington (Karlin et al.; 2004) are plotted as blue bars (labelled KA-KH).

Age Range (Years Ago)	Scenario 1	Scenario 2	Scenario 3	Scenario 4	Scenario 5	Scenario 6	Scenario 7	Scenario 8	Scenario 9	Mean	Cluster from this study	Nelson et al. (2003, 2014) Earthquakes	Karlin et al. (2004) Events
0–200	2.371	1.343	0.807	0.876	1.294	0.664	1.378	0.297	0.69	1.08			B
200–400	1.69	2.424	1.498	2.017	1.959	1.854	2.089	2.161	0.788	1.831			B
400–600	2.339	1.161	1.938	2.401	2.648	2.416	2.488	2.58	1.927	2.211	A	E	
600–800	1.138	0.806	1.052	1.072	1.556	1.378	1.031	0.681	1.736	1.161		E	C
800–1,000	1.969	1.164	1.193	2.623	1.221	3.082	2.608	3.005	1.999	2.096	B	E	D
1,000–1,200	4.917	2.470	4.656	3.559	4.647	3.292	5.328	4.137	3.144	4.017	B	D	E
1,200–1,400	0.7631	0.653	1.009	2.071	1.872	1.120	1.597	1.716	1.083	1.32		C	
1,400–1,600	0.216	0.431	0.322	0.301	0.099	0.147	0.055	0.047	0.284	0.211			F
1,600–1,800	0.211	0.065	0	0.879	0.942	0.52	0.766	1.546	0	0.548			F
1,800–2,000	0.999	1.099	1.87	0.922	1.59	1.272	1.846	1.779	0.601	1.331			F & G
2,000–2,200	1.638	3.397	1.436	4.419	3.225	1.641	4.051	3.643	3.208	2.962	C	B	G
2,200–2,400	1.686	1.787	0.599	1.112	1.751	2.012	1.25	0.989	2.203	1.487		B	G
2,400–2,600	0.661	7.8E-2	0.823	1.934	0.578	0.162	1.209	1.273	0.622	0.816		B	
2,600–2,800	2.957	2.253	2.056	2.262	3.253	2.9991	3.3	3.408	2.194	2.742	D	A	H
2,800–3,000	0.239	0.59	0.908	1.171	0.726	0.107	0.483	0.489	0.51	0.580		A	H
3,000–3,200	1.39	1.528	1.931	1.145	0.231	1.988	1.256	0.922	0.74	1.237		A	H
3,200–3,400	0.913	1.561	0.591	1.519	2.092	2.053	1.607	2.155	1.805	1.588		A	H
3,400–3,600	0.985	0.278	0.945	1.043	0.826	0.661	0.66	0.688	0.849	0.771		A	H
3,600–3,800	0.735	1.008	1.025	0.824	1.508	1.133	0.859	1.215	1.508	1.090		A	
3,800–4,000	2.111	4.208	2.767	2.66	3.516	2.956	3.445	3.798	4.094	3.284	E	A	
4,000–4,200	0.386	0.314	0.363	0.952	0.376	0.679	0.625	0.463	0.526	0.52		A	
4,200–4,400	2.185	3.764	1.983	1.962	1.715	1.342	2.119	2.248	2.997	2.257	F	A	
4,400–4,600	3.091	3.861	2.492	2.648	2.194	2.278	1.829	2.232	1.943	2.508	F	A	
4,600–4,800	0.336	0.374	0.589	0.346	0.136	0.282	0.223	0.168	0.517	0.33		A	

Table 2.3: K-S test normalized D statistics, for different earthquake scenarios and time periods, and earthquakes from paleoseismology studies

inflate the conditional probability at high PGVs (e.g., the¬ 2.8–2.6 ka event in Figure 2.8).

By comparing across time, we look for high positive correlation values to indicate that an earthquake likely occurred during a given period. Moreover, by comparing across scenarios during that interval (Figure 2.16), we estimate the most likely distribution of ground motions from that simulated earthquake scenario. We observe the highest normalized D statistics in the 1.2 – 1.0 ka and 1.0 – 0.8 ka time periods, which correspond to the time of the last major Seattle Fault earthquake (peak labeled B in Figure 2.9). Within these time periods, earthquake scenario 7 (Table 2.1, Figure 2.4), from 1.2 – 1.0 ka, has the highest D statistic among the different scenarios considered. This scenario was generated using a western hypocenter and slip distribution 3, with centrally concentrated slip (Table 2.1, Figure 2.5). The spatial distribution of PGV from scenario 7 shows the strongest ground motions in a band stretching from West Seattle to Mercer Island (Figure 2.4, scenario 7). Relative to other scenarios, this scenario also has higher ground motions along the bluffs bordering the Puget Sound.

We can also look for other clusters in the normalized D statistic that indicate other possible earthquakes (value ≥ 2). As a check on this approach, we inspect the most recent 200 years, an interval where no significant earthquakes were recorded along the Seattle Fault. As expected, we find no spike or corresponding increase in the normalized D statistic to indicate any earthquake-induced landslide activity. Consideration of older time intervals shows evidence for one cluster younger and four clusters older than the 1,100 yr B. P. Seattle Fault earthquake (B in Figure 2.9). We name the clusters in increasing age as A (0.6–0.4 ka), B (1.2 – 0.8 ka), C (2.2–2.0 ka), D (2.8–2.6 ka), E (4.0–3.8 ka), and F (4.6–4.2 ka) (Figure 2.9 and Table 2.3). The slip and hypocenters of the best-fitting scenarios for each of the clusters are presented in Figure 2.5 and the expected ground motions are presented in Figure 2.4.

2.5 Discussion

The new deep-seated landslide inventory presented here combined with landslide-age and earthquake ground-shaking scenario models substantiates that the landscape records past earthquakes on crustal faults in the Seattle region. Each line of evidence examined supports

the inference that earthquake-induced landsliding led to temporal and spatial clustering of landslide deposits in the study area, at least for the last M 7 Seattle Fault earthquake (1,100 yr B. P.). Although this interpretation can be drawn from either the temporal or spatial datasets separately, the most robust conclusions come from considering all the data and models together. The discovery of landslide clustering due to earthquakes is important over both geologic and human timescales, as such patterns should affect landscape evolution and hazards in the region. Our results differ from work by LaHusen et al. (2020), which found little evidence that deep-seated landslides within the Oregon Coast Range are triggered by subduction zone earthquakes. This may be due to stronger ground motions and less seismic wave attenuation from crustal fault earthquakes, as opposed to subduction earthquakes. While CSZ earthquakes may have higher moment magnitude, they are typically deeper and offshore, and thus generally have lower PGVs at inland sites (Serey et al.; 2019). Alternatively, the presence of a fault damage zone in the crustal SFZ could be at play, which has been shown to affect earthquake-induced landslide patterns in other fault zones (e.g. Bloom et al. (2022)) and there are differences in radiated frequency content among crustal vs subduction zone earthquakes. The observed temporal pattern of landslide ages in the Puget Lowland fits slightly better to a model with a pulse of landslides at the time of the last major Seattle Fault earthquake rather than steady landslides through time (Figure 2.7). Also, a model based on the landslide area distributions fits better than the frequency distributions. This indicates that a consideration of landslide area through time can help identify an earthquake signal. Perhaps this is due to some differences in size from different landslide sources, though this variation is difficult to resolve with our dataset (see Figure 2.17, which shows a constant landslide-area power law exponent through time, suggesting no source dependence for landslide size). However, it is worth noting the uncertainty in resolving an earthquake signal from landslide age-modeling alone. In both plots that we consider, landslide frequency and landslide area (Figure 2.7), the fits to the earthquake model are not perfect and it is possible that the cluster we interpret as an earthquake signal 1,000 years ago may be noise. Also, our focus on landslides with areas greater than $\geq$9,000 m^2 may bias the distribution and miss some pattern in smaller landslides. Additionally, while our models assume a relatively constant background rate, even precipitation-induced

landslide events tend to be stochastic (Coe et al.; 2004). This means that our models do not account for the Sadler effect (Sadler; 1981; Schumer and Jerolmack; 2009), seen in the inventory dataset (see appendix). The large uncertainties on individual landslide ages associated with the age-roughness dating approach limit our ability to identify high-magnitude landslide-triggering earthquakes in the record, especially if they occur somewhat frequently. In theory, infrequent large earthquakes, such as along the Seattle Fault, should be distinguishable in the landslide record, whereas more frequent earthquakes will blur together and be indistinguishable from the background rate. In practice, this means the landslide timing record cannot be used to rule out the occurrence of earthquakes due to an absence of temporal clustering and the strongest conclusions can be made when combining landslide age information with spatial patterns (e.g. Grant et al. (2022)). Additionally, it is worth noting that some of the earthquake-induced landslides may not be triggered co-seismically, but instead fail in the following years after an earthquake main shock due to aftershocks or weakened slope materials.

In our study, we also see a trend in the spatial clustering of landslides that comports with ground shaking modeled for past earthquakes on the Seattle Fault (Stone et al.; 2022) (e.g., Figure 2.6). Given similarities in geologic material and mean annual precipitation across the study area, we expect spatial patterns of non-seismic landslides to be relatively unclustered and random through time. Future work may be able to compare our deep-seated landslide inventory with modern shallow landslide inventories to test if this assumption is true for non-seismic landslides. In contrast, when looking at specific time periods for our dataset, we observe a significant shift in the spatial pattern of landsliding that we interpret to record earthquake activity (Figure 2.8). This shows that earthquake-induced landslides do not affect the entire study area equally and will have different effects in different areas. Additionally, there is a mismatch in the distribution of interpreted non-seismic and earthquake-induced landslides (200–0 year old versus 1,200–1,000 year old landslides in Figure 2.8). This observation has implications for landslide hazard assessments, as hazard based on rainfall-based predictions, for example, will not necessarily correlate with hazard from earthquake-induced landslides.

By comparing the spatial landslide distribution to the modeled PGVs in different scenar-

ios, we can look for an indication that an earthquake occurred during that time interval, as well as determine the best-fitting patterns in ground motions during the last major earthquake on the Seattle Fault. We do this using the K-S D statistic as a measure of how different a given landslide distribution is from the norm, which for a positive correlation indicates the likelihood that a landslide distribution is caused by an earthquake scenario. For the 1.2 – 1.0 ka and 1.0 – 0.8 ka intervals, the period that includes the last known major rupture on the Seattle Fault, all ground-motion scenarios show positive correlation D statistics well above the critical value (Figure 2.9, Table 2.3). None of the earlier time intervals show scenarios this high above the normalized critical value of 1. These results show strong evidence that spatial landslide patterns were impacted by an earthquake during this time. Although any of the scenarios are statistically reasonable based on the normalized critical value, the scenario that best matches the landslide distribution (scenario 7) has the strongest ground shaking stretching from West Seattle to Mercer Island, with strong shaking along the bluffs of the Puget Sound. This scenario was created using a western hypocenter and central slip distribution.

We next speculate on the earthquake properties from other identified possible earthquakes using the best-fit scenarios, with the caveat that the nine earthquake scenarios considered do not represent a full suite of potential rupture characteristics. Many of the landslide clusters found in our data may represent the same earthquakes recorded in fault trenches in the SFZ (Nelson et al.; 2003, 2014) and turbidite and landslide deposits in Lake Washington (Karlin et al.; 2004) (Figure 2.9). Cluster A (0.6–0.4 ka) correlates with earthquake NE (940–380 cal yr. B.P) from Nelson et al. (2014). This may also represent RH2 (650–200 cal yr. B.P) noted by Angster et al. (2022). Cluster A does not have a clear best-fit ground-motion scenario, with most scenarios performing equally well (Figure 2.16). Cluster C (2.2–2.0 ka) correlates with earthquake NB (2,650–1,940 cal yr. B.P) from Nelson et al. (2003, 2014) and event KG (2,260–1,850 cal yr. B.P) from Karlin et al. (2004). The best-fit scenario (Figure 2.16) for this cluster indicates the strongest ground motion from Beacon Hill to Newcastle (Figure 2.6), with high ground motions along the Puget Sound on the western edge of the study area. Cluster D (2.8–2.6 ka) may represent earthquake NA ($\geq$2,500 cal yr. B.P) from Nelson et al. (2003, 2014) and event KH (3,400–2,700 cal

yr. B.P) from Karlin et al. (2004). The best scenario (Figure 2.16) for cluster D had the strongest motions stretched from West Seattle to Mercer Island (Figure 2.6), with relatively high ground motions around Lake Washington. Cluster E (4.0–3.8 ka) overlaps, as well, with earthquake NA (≥2,500 cal yr. B.P) from Nelson et al. (2003, 2014). This cluster has some of the lowest ground motions of any scenario, with strong shaking mostly confined to the area near the surface trace of the fault. The 4.6–4.4 ka and 4.4–4.2 ka increases (Cluster F) also overlap with earthquake NA (≥2,500 cal yr. B.P) from Nelson et al. (2003). This cluster also has a best fit (Figure 2.16) to the same scenario as cluster E, which suggests that E and F might be a signal from the same earthquake. Based on the best-fits to all these clusters (Figure 2.16), an eastern hypocenter appears least likely to have occurred in the past 4,600 years, while all other hypocenters and all slip distributions tend to be the best-fit for at least one possible earthquake.

Some proposed earthquakes from Nelson et al. (2003, 2014); Karlin et al. (2004); Angster et al. (2022) are not apparent in our landslide inventory. Karlin et al. (2004) date submarine landslide and turbidite deposits in Lake Washington and interpret some of these to be seismically induced. Although the Seattle Fault is proximal to this lake, other triggers, such as large storms (e.g. Karlin et al. (2004) event KD [900–680 cal yr. B.P]) or earthquakes on other faults or the CSZ (e.g. Karlin et al. (2004) event KB [400–130 cal yr. B.P]), could lead to such deposits. In contrast, Nelson et al. (2003, 2014) studies and Angster et al. (2022) are directly linked to the Seattle Fault as they trenched a backthrust. One possible explanation for why we could miss an event would be if dry conditions during the rupture led to fewer landslides and a less diagnostic spatial pattern. This may explain why we do not see a clear signal from earthquake NC (1,350–1,170 cal yr. B.P) from Nelson et al. (2003, 2014) and why there is also no landslide signal in Lake Washington at that time (Karlin et al.; 2004). To this point, Angster et al. (2022) tested both dry and wet hillslope conditions and found that the total area of landslide sources was an order of magnitude smaller when an earthquake happened during the dry season than when soils were completely saturated.

The D statistic for the inverse correlation may also contain information regarding these past earthquakes. Only three time periods (2.0–1.8 ka, 1.0–0.8 ka, 0.2–0 ka) have inverse D statistics higher than 2, and all of these postdate landslide clusters C, B, and A respectively.

This may represent a delayed effect where, after an earthquake has caused landslides on unstable slopes with strong shaking, the remaining unstable slopes will be biased towards areas that experienced less shaking. In the following centuries this pre-existing bias could lead to an apparent inverse relationship between landslides and ground motions during periods with no earthquakes. This conflicts with other studies (e.g. Parker et al. (2015)) showing that earthquake-induced landslide locations are influenced by past failures, and are more likely in areas that failed in the past. Perhaps the triggering mechanism is important here, with earthquake-induced landslides occurring more frequently in the same locations while rainfall-induced landslides are more likely in areas without earthquake-induced landslides. Further testing of this hypothesis could help improve our understanding.

Taken together, these results can be tentatively interpreted to indicate that the Seattle Fault does not have a characteristic rupture style and instead generates earthquakes with a variety of slip distributions, hypocenter locations, and resulting ground motion distributions. While this means that we cannot rule out any rupture parameter for either past or future earthquakes on the fault, we can assess the likelihood of different ground motion distributions in the past based on the landslide record. For example, based on our analyses, we can show that an eastern hypocenter is the least likely hypocenter location for these past earthquakes. An important caveat to this interpretation is that ground motions are not unique to a particular set of rupture parameters and the modeled likelihoods will not fully contain the rupture parameters to a single set of values. The ground motions also used a uniform shear-wave velocity minimum of 450 m/s, instead of a more detailed consideration of variations in glacial sediment site effects (see appendix for more discussion on the ground motion simulation parameters). Additionally, the different scenarios all have sufficiently different PGV distributions such that risk analyses based on a single earthquake scenario may obscure the inter-event variability of seismic hazard due to Seattle Fault earthquakes. Because of these factors, future work using this method could be improved by considering a wider range of earthquake scenarios, with more variability and granularity in the rupture parameters. For example, while Stone et al. (2022) considers three different hypocenters, they are all at the same depth on the fault. Considering different hypocenter and rupture depths could expand the range of possible ground motions we use to evaluate earthquake-induced

landslides.

2.6 Conclusions

In this study, we combine analysis of a new, deep-seated landslide inventory with morphologically estimated ages, with landslide and earthquake simulation modeling to investigate spatial and temporal clusters of landslides in the Puget Lowlands of Washington State, USA. We find evidence of increased landsliding around the time of the last major Seattle Fault earthquake. Spatially, this corresponds to more landslides in areas with higher modeled PGVs. Temporally, this increase in landslides leads to possible clustering with ages near the time of the last major Seattle Fault earthquake. By restricting our view to landslides within the timeframe of the 1050–1020 cal yr. BP Seattle Fault earthquake (Bucknam et al.; 1992; Atwater and Moore; 1992; Sherrod; 2001; Nelson et al.; 2014), we also see an increase in spatial clustering compared to the temporally unrestricted spatial patterns. Landslide clustering also reveals evidence of earlier earthquakes on the Seattle Fault, some of which correlate with other paleoseismic evidence (Nelson et al.; 2003, 2014; Karlin et al.; 2004). Our work helps to refine the ages for these past earthquakes. Earthquake NA ($\geq$2,500 cal yr. B.P) from Nelson et al. (2003) is poorly constrained, and while we cannot narrow it down to a single time period, we can suggest that it may be related to either landslide cluster D (2.6–2.8 ka), E (3.8–4.0 ka), or F (4.2–4.6 ka). In addition, comparison of different earthquake scenarios to the landslide inventory identifies the modeled ground motions that best match the clustering related to the last major Seattle Fault earthquake. We find that the scenario with strongest shaking stretching from West Seattle to Mercer Island and high shaking along the bluffs bordering the Puget Sound fits best. This scenario (i.e., scenario 7) was created with a western hypocenter and central slip distribution. By applying this technique to the other possible earthquake-induced landslide clusters, we see that a variety of different ground motion distributions provide the best match to different temporal landslide clusters (Figure 2.16), which suggests that Seattle Fault earthquakes have variable rupture characteristics that result in different patterns of ground shaking. More generally, our study demonstrates the power of combining a regional landslide inventory with multiple earthquake scenario models to perform paleoseismic analysis. Future work in the Puget

Lowland could investigate if there are similar landslide clusters related to other crustal faults such as the southern Whidbey Island Fault. Our approach offers a means to investigate past earthquakes, especially in areas with rare but strong earthquakes in landscapes prone to landsliding. Where records of past seismic activity are missing, the method may be used as one of few means to extract information about past earthquake ground motions directly from the landscape.

Bibliography

A., C., Shalizi, C. and Newman, M. (2009). Power-law distributions in empirical data, *SIAM Review* **51**(4): 661–703. arXiv:0706.1062,.

Allstadt, K., Vidale, J. and Frankel, A. (2013). A scenario study of seismically induced landsliding in seattle using broadband synthetic seismograms, *Bulletin of the Seismological Society of America* **103**(6): 2971–2992.

Angster, S., Sherrod, B., Pearl, J., Staisch, L. and Johns, W. (2022). Paleoseismic evidence for a near historic rupture within the seattle fault zone: Implications for complex hanging wall kinematics above an active blind reverse fault, *AGU Fall Meeting Abstracts*, Vol. 2022, p. 15 –07.

Atwater, B. (1999). Radiocarbon dating of a seattle earthquake to ad 900–930, *Seismological Research Letters* **70**(2): 232.

Atwater, B. and Moore, A. (1992). A tsunami about 1000 years ago in puget sound, washington, *Science* **258**(5088): 1614–1617.

Aylsworth, J., Lawrence, D. and Guertin, J. (2000). Did two massive earthquakes in the holocene induce widespread landsliding and near-surface deformation in part of the ottawa valley, *Canada? Geology* **28**(10): 903–906.

Baum, R., Chleborad, A. and Schuster, R. (1998). Landslides triggered by the winter 1996-97 storms in the puget lowland, washington, *Open-File Report* .

Baum, R., Coe, J., Godt, J., Harp, E., Reid, M., Savage, W., Brien, D., Chleborad, A., McKenna, J. and Michael, J. (2005). Regional landslide-hazard assessment for seattle, *Landslides* **2**: 266–279.

Bird, J. and Bommer, J. (2004). Earthquake losses due to ground failure, *Engineering Geology* **75**(2): 147–179.

Black, B. A., Pearl, J. K., Pearson, C. L., Pringle, P. T., Frank, D. C., Page, M. T., Buckley, B. M., Cook, E. R., Harley, G. L., King, K. J. et al. (2023). A multifault earthquake threat for the seattle metropolitan region revealed by mass tree mortality, *Science advances* **9**(39): eadh4973.

Blakely, R., Wells, R., Weaver, C. and Johnson, S. (2002). Location, structure, and seismicity of the seattle fault zone, washington; evidence from aeromagnetic anomalies, geologic mapping, and seismic-reflection data, *Geological Society of America Bulletin* **114**: 169–177.

Bloom, C., Howell, A., Stahl, T., Massey, C. and Singeisen, C. (2022). The influence of off-fault deformation zones on the near-fault distribution of coseismic landslides, *Geology* **50**(3): 272–277.

Booth, A., LaHusen, S., Duvall, A. and Montgomery, D. (2017). Holocene history of deep-seated landsliding in the north fork stillaguamish river valley from surface roughness analysis, radiocarbon dating, and numerical landscape evolution modeling, *Journal of Geophysical Research: Earth Surface* **122**(2): 456–472.

Booth, A., Roering, J. and Perron, T. (2009). Automated landslide mapping using spectral analysis and high-resolution topographic data: Puget sound lowlands, washington, and portland hills, oregon, *Geomorphology* **109**(3-4): 132–147.

Brink, U., Molzer, P., Fisher, M., Blakely, R., Bucknam, R., Parsons, T., Crosson, R. and Creager, K. (2002). Subsurface geometry and evolution of the seattle fault zone and the seattle basin, washington, *Bulletin of the Seismological Society of America* **92**: 1737–1753.

Brink, U., Song, J. and Bucknam, R. (2006). Rupture models for the ad 900–930 seattle fault earthquake from uplifted shorelines, *Geology* **34**(7): 585–588.

Brocher, T., Parsons, T., Blakely, R., Christensen, N., Fisher, M. and Wells, R. (2001). Upper crustal structure in puget lowland, washington: Results from the 1998 seismic hazards investigation in puget sound, *Journal of Geophysical Research: Solid Earth* **106**(B7): 13541–13564.

Brooks, G. (2013). A massive sensitive clay landslide, quyon valley, southwestern quebec, canada, and evidence for a paleoearthquake triggering mechanism, *Quaternary Research* **80**(3): 425–434.

Bucknam, R., Hemphill-Haley, E. and Leopold, E. (1992). Abrupt uplift within the past 1700 years at southern puget sound, washington, *Science* **258**: 1611–1614.

Campforts, B., Shobe, C., Steer, P., Vanmaercke, M., Lague, D. and Braun, J. (2020). Hylands 1.0: a hybrid landscape evolution model to simulate the impact of landslides and landslide-derived sediment on landscape evolution, *Geoscientific Model Development* **13**(9): 3863–3886.

Coe, J., Godt, J. and Tachker, P. (2004). Map showing recent (1997-98 el nino) and historical landslides, crow creek and vicinity, alameda and contra costa counties. US Department of the Interior, US Geological Survey.

Croissant, T., Steer, P., Lague, D., Davy, P., Jeandet, L. and Hilton, R. (2019). Seismic cycles, earthquakes, landslides and sediment fluxes: Linking tectonics to surface processes using a reduced-complexity model, *Geomorphology* **339**: 87–103.

Crozier, M., Deimel, M. and Simon, J. (1995). Investigation of earthquake triggering for deep-seated landslides, taranaki, new zealand, *Quaternary International* **25**: 65–73.

Cwynar, L. (1987). Fire and the forest history of the north cascade range, *Ecology* **68**(4): 791–802.

Davis, E., Chang, S., Hou, S., Teal, T., Cowell, K. and Garcia-Arceo, S. (2022). A century of landslides in seattle, washington: Coalescing and digitizing the city's historic landslide inventories, *Environmental and Engineering Geoscience* **28**(4): 335–346.

Fan, X., Scaringi, G., Korup, O., West, A., Westen, C., Tanyas, H. and Huang, R. (2019). Earthquake-induced chains of geologic hazards: Patterns, mechanisms, and impacts, *Reviews of geophysics* **57**(2): 421–503.

Forero-Duenas, C. (1996). Experiences from the paez earthquake, colombia, *Eleventh World Conference on Earthquake Engineering. Pergamon, Elsevier, Oxford. Paper* (103).

Francis, O., Fan, X., Hales, T., Hobley, D., Xu, Q. and Huang, R. (2022). The fate of sediment after a large earthquake, *Journal of Geophysical Research: Earth Surface* **127**(3): 2021 006352.

Frattini, P. and Crosta, G. (2013). The role of material properties and landscape morphology on landslide size distributions, *Earth and Planetary Science Letters* **361**: 310–319.

Godt, J., Baum, R. and Chleborad, A. (2006). Rainfall characteristics for shallow landsliding in seattle, *Earth Surface Processes and Landforms: The Journal of the British Geomorphological Research Group* **31**(1): 97–110.

Goetz, J., Brenning, A., Petschko, H. and Leopold, P. (2015). Evaluating machine learning and statistical prediction techniques for landslide susceptibility modeling, *Computers and geosciences* **81**: 1–11.

Goldfinger, C., Nelson, C., Morey, A., Johnson, J., Patton, J., Karabanov, E. and Vallier, T. (2012). Turbidite event history—methods and implications for holocene paleoseismicity of the cascadia subduction zone (no. 1661-f, *US Geological Survey* .

Grant, A. (2017). Regional-scale coseismic landslide hazard modeling and consequence analysis.

Grant, A., Struble, W. and LaHusen, S. (2022). Limits to coseismic landslides triggered by cascadia subduction zone earthquakes, *Geomorphology* **418**: 108477.

1123 Harp, E., Michael, J. and Laprade, W. (2008). Shallow landslide hazard map of seattle,
1124 washington, *Landslides and Engineering Geology of the Seattle, Washington, Area: Geo-*
1125 *logical Society of America Reviews in Engineering Geology* **20**: 67–82.

1126 Highland, L. (2003). An account of preliminary landslide damage and losses resulting from
1127 the february 28, 2001. US Department of the Interior, US Geological Survey.

1128 Hungr, O., Leroueil, S. and Picarelli, L. (2014). The varnes classification of landslide types,
1129 an upyear, *Landslides* **11**: 167–194.

1130 Ishihara, K., Haeri, S., Moinfar, A., Towhata, I. and Tsujino, S. (1992). Geotechnical aspects
1131 of the june 20, 1990 manjil earthquake in iran, *Soils and Foundations* **32**(3): 61–78.

1132 Jacoby, G., Williams, P. and Buckley, B. (1992). Tree ring correlation between
1133 prehistoric landslides and abrupt tectonic events in seattle, washington, *Science*
1134 **258**(5088): 1621–1623.

1135 Jibson, R. (1985). Landslides caused by the 1811-12 new madrid earthquake.

1136 Jibson, R. (1996). Use of landslides for paleoseismic analysis, *Engineering geology*
1137 **43**(4): 291–323.

1138 Jibson, R. and Keefer, D. (1993). Analysis of the seismic origin of landslides: examples from
1139 the new madrid seismic zone, *Geological Society of America Bulletin* **105**(4): 521–536.

1140 Johnson, S., Dadisman, S., Childs, J. and Stanley, W. (1999). Active tectonics of the
1141 seattle fault and central puget sound, washington; implications for earthquake hazards,
1142 *Geological Society of America Bulletin* **111**: 1042–1053.

1143 Johnson, S., Nelson, A., Personius, S., Wells, R., Kelsey, H., Sherrod, B. and Harding, D.
1144 (2004). Evidence for late holocene earthquakes on the utsalady point fault, northern puget
1145 lowland, washington, *Bulletin of the Seismological Society of America* **94**(6): 2299–2316.

1146 Karlin, R., Holmes, M., Abella, S. and Sylwester, R. (2004). Holocene landslides and a
1147 3500-year record of pacific northwest earthquakes from sediments in lake washington,
1148 *GSA Bulletin* **116**(1-2): 94–108.

1149 Keefer, D. (1984). Landslides caused by earthquakes, *Geological Society of America Bulletin*
1150 **95**(4): 406–421.

1151 Kelsey, H., Sherrod, B., Nelson, A. and Brocher, T. (2008). Earthquakes generated from
1152 bedding plane-parallel reverse faults above an active wedge thrust, seattle fault zone,
1153 *Geological Society of America Bulletin* **120**(11-12): 1581–1597.

1154 Kumar, P. and Foufoula-Georgiou, E. (1997). Wavelet analysis for geophysical applications,
1155 *Reviews of geophysics* **35**(4): 385–412.

1156 LaHusen, S., Duvall, A., Booth, A., Grant, A., Mishkin, B., Montgomery, D. and Wartman,
1157 J. (2020). Rainfall triggers more deep-seated landslides than cascadia earthquakes in the
1158 oregon coast range, usa, *Science advances* **6**(38): 6790.

1159 LaHusen, S., Duvall, A., Booth, A. and Montgomery, D. (2016). Surface roughness dating of
1160 long-runout landslides near oso, washington (usa), reveals persistent postglacial hillslope
1161 instability, *Geology* **44**(2): 111–114.

1162 Laprade, W., Kirkland, T., Nashem, W. and Robertson, C. (2000). Seattle landslide study,
1163 *Technical report*.

1164 Lashermes, B., Foufoula-Georgiou, E. and Dietrich, W. (2007). Channel network extraction
1165 from high resolution topography using wavelets, *Geophysical Research Letters* **34**(23).

1166 Ludwin, R., Thrush, C., James, K., Buerge, D., Jonientz-Trisler, C., Rasmussen, J. and
1167 Los Angeles, A. (2005). Serpent spirit-power stories along the seattle fault, *Seismological*
1168 *Research Letters* **76**(4): 426–431.

1169 Luna, L. and Korup, O. (2022). Seasonal landslide activity lags annual precipitation pattern
1170 in the pacific northwest, geophys, *Res. Lett* **49**(18): 2022 098506.

1171 Malamud, B., Turcotte, D., Guzzetti, F. and Reichenbach, P. (2004). Landslide inventories
1172 and their statistical properties, *Earth Surface Processes and Landforms* **29**(6): 687–711.

1173 Marc, O., Hovius, N. and Meunier, P. (2016). The mass balance of earthquakes and earth-
1174 quake sequences, *Geophysical Research Letters* **43**(8): 3708–3716.

1175 Massey Jr, F. J. (1951). The kolmogorov-smirnov test for goodness of fit, *Journal of the*
1176 *American statistical Association* **46**(253): 68–78.

1177 McKean, J. and Roering, J. (2004). Objective landslide detection and surface morphology
1178 mapping using high-resolution airborne laser altimetry, *Geomorphology* **57**(3-4): 331–351.

1179 Medwedeff, W., Clark, M., Zekkos, D. and West, A. (2020). Characteristic landslide dis-
1180 tributions: An investigation of landscape controls on landslide size, *Earth and Planetary*
1181 *Science Letters* **539**: 116203.

1182 Meunier, P., Hovius, N. and Haines, J. (2008). Topographic site effects and the location of
1183 earthquake induced landslides, *Earth and Planetary Science Letters* **275**(3-4): 221–232.

1184 Moore, G., Roland, E., Bennett, S., Watt, J., Kluesner, J., Brothers, D. and Myers, E.
1185 (2022). High-resolution marine seismic imaging of the seattle fault zone: Near-surface
1186 insights into fault zone geometry, quaternary deformation, and long-term evolution, *Bul-*
1187 *letin of the Seismological Society of America* **112**(5): 2715–2744.

1188 Nelson, A., Johnson, S., Kelsey, H., Wells, R., Sherrod, B., Pezzopane, S. and Bucknam, R.
1189 (2003). Late holocene earthquakes on the toe jam hill fault, seattle fault zone, bainbridge
1190 island, washington, *Geological Society of America Bulletin* **115**(11): 1388–1403.

1191 Nelson, A., Personius, S., Sherrod, B., Kelsey, H., Johnson, S., Bradley, L. and Wells,
1192 R. (2014). Diverse rupture modes for surface-deforming upper plate earthquakes in the
1193 southern puget lowland of washington state, *Geosphere* **10**(4): 769–796.

1194 Parker, R., Hancox, G., Petley, D., Massey, C., Densmore, A. and Rosser, N. (2015). Spa-
1195 tial distributions of earthquake-induced landslides and hillslope preconditioning in the
1196 northwest south island, new zealand, *Earth surface dynamics* **3**(4): 501–525.

1197 Perkins, J., Reid, M. and Schmidt, K. (2017). Control of landslide volume and haz-
1198 ard by glacial stratigraphic architecture, northwest washington state, usa, *Geology*
1199 **45**(12): 1139–1142.

Pollock, W., Grant, A., Wartman, J. and Abou-Jaoude, G. (2019). Multimodal method for landslide risk analysis, *MethodsX* **6**: 827–836.

Pratt, T., Johnson, S., Potter, C., Stephenson, W. and Finn, C. (1997). Seismic reflection images beneath puget sound, western washington state; the puget lowland thrust sheet hypothesis, *Journal of Geophysical Research* **102**: 27469–27489.

Pánek, T. (2015). Recent progress in landslide dating: a global overview, *Progress in Physical Geography* **39**(2): 168–198.

Ramsey, C. (2009). Bayesian analysis of radiocarbon years, *Radiocarbon* **51**(1): 337–360.

Ramsey, C. (2017). Methods for summarizing radiocarbon datasets, *Radiocarbon* **59**(6): 1809–1833.

Rasanen, R. and Maurer, B. (2021). Probabilistic seismic source inversion from regional landslide evidence, *Landslides* p. 1–13.

Reimer, P., Bard, E., Bayliss, A., Beck, J., Blackwell, P., Ramsey, C., Buck, C., Cheng, H., Edwards, R., Friedrich, M. and Grootes, P. (2013). Intcal13 and marine13 radiocarbon age calibration curves 0–50,000 years cal bp, *Radiocarbon* **55**(4): 1869–1887.

Ricker, N. (1943). Further developments in the wavelet theory of seismogram structure, *Bulletin of the Seismological Society of America* **33**(3): 197–228.

Sadler, P. (1981). Sediment accumulation rates and the completeness of stratigraphic sections, *The Journal of Geology* **89**(5): 569–584.

Schulz, W. (2007). Landslide susceptibility revealed by lidar imagery and historical records, seattle, washington, *Engineering Geology* **89**(1-2): 67–87.

Schulz, W., Galloway, S. and Higgins, J. (2012). Evidence for earthquake triggering of large landslides in coastal oregon, usa, *Geomorphology* **141**: 88–98.

Schumer, R. and Jerolmack, D. (2009). Real and apparent changes in sediment deposition rates through time, *Journal of Geophysical Research: Earth Surface* **114**(F3).

Schuster, R., Logan, R. and Pringle, P. (1992). Prehistoric rock avalanches in the olympic mountains, washington, *Science* **258**(5088): 1620–1621.

Serey, A., Piñero-Feliciangeli, L., Sepúlveda, S., Poblete, F., Petley, D. and Murphy, W. (2019). Landslides induced by the 2010 chile megathrust earthquake: A comprehensive inventory and correlations with geological and seismic factors, *Landslides* **16**: 1153–1165.

Sherrod, B. (2001). Evidence for earthquake-induced subsidence about 1100 yr. ago in coastal marshes of southern puget sound, washington, *GSA Bulletin* **113**(10): 1299–1311.

Sherrod, B., Blakely, R., Weaver, C., Kelsey, H., Barnett, E., Liberty, L. and Pape, K. (2008). Finding concealed active faults: Extending the southern whidbey island fault across the puget lowland, washington, *Journal of Geophysical Research: Solid Earth* **113**(B5).

Sherrod, B., Brocher, T., Weaver, C., Bucknam, R., Blakely, R., Kelsey, H. and Haugerud, R. (2004). Holocene fault scarps near tacoma, *Geology* **32**(1): 9–12.

Sherrod, B., Bucknam, R. and Leopold, E. (2000). Holocene relative sea level changes along the seattle fault at restoration point, washington, *Quaternary Research* **54**(3): 384–93.

Stone, I., Wirth, E. and Frankel, A. (2022). Topographic response to simulated m w 6.5–7.0 earthquakes on the seattle fault, *Bulletin of the Seismological Society of America* **112**(3): 1436–1462.

Struble, W., Roering, J., Black, B., Burns, W., Calhoun, N. and Wetherell, L. (2020). Dendrochronological dating of landslides in western oregon: Searching for signals of the cascadia ad 1700 earthquake, *GSA Bulletin* **132**(7-8): 1775–1791.

Styron, R. and Sherrod, B. (2021). Improving paleoseismic earthquake magnitude estimates with rupture length information: application to the puget lowland, washington state, usa, *Bulletin of the Seismological Society of America* **111**(2): 1139–1153.

Survey, W. G. (2020). Landslide protocol inventory mapping–gis data, february, 2020:

Washington geological survey digital data series 19. version 2.0, previously released January, 2019.

Tanyaş, H., Allstadt, K. and Westen, C. (2018). An upyeard method for estimating landslide-event magnitude, *Earth surface processes and landforms* **43**(9): 1836–1847.

Tubbs, D. (1974). *Landslides in Seattle*, Department of Natural Resources.

Valagussa, A., Marc, O., Frattini, P. and Crosta, G. (2019). Seismic and geological controls on earthquake-induced landslide size, *Earth and Planetary Science Letters* **506**: 268–281.

Wang, J., Howarth, J., McClymont, E., Densmore, A., Fitzsimons, S., Croissant, T. and Hilton, R. (2020). Long-term patterns of hillslope erosion by earthquake-induced landslides shape mountain landscapes, *Science advances* **6**(23): 6446.

Wartman, J., Dunham, L., Tiwari, B. and Pradel, D. (2013). Landslides in eastern honshu induced by the 2011 tohoku earthquake, *Bulletin of the Seismological Society of America* **103**(2B): 1503– 1521.

Yount, J., Minard, J. and Dembroff, G. (1993). *Geologic map of surficial deposits in the Seattle*, US Geological Survey.

Landslide Name	DirectAMS Code	Submitter ID	Fraction of Modern (pMC)	1σ Error (pMC)
North Issaquah Slide	D-AMS 034468	MS1901	89.37	0.25
Schmitz Park N	D-AMS 034469	SE1901	95.36	0.27
Schmitz Park E	D-AMS 034470	SE1902	44.61	0.2
Norway Hill	D-AMS 036575	BP1901	83.35	0.25
Norway Hill	D-AMS 036576	BP1902	80.87	0.37
Norway Hill	D-AMS 036577	BP1903	98.02	0.25
Norway Hill	D-AMS 036578	BP1904	97.87	0.31
Coal Creek	D-AMS 034879	CC1901	90.65	0.23
May Creek	D-AMS 042596	MC0121	96.13	0.25

Table 2.4: Additional Landslide Radiocarbon Date Information

2.7 Appendix

2.7.1 Seattle Fault Earthquake Simulations

We used predicted peak ground velocities (PGVs) from 9 different M7 scenario earthquakes on the Seattle Fault to understand possible ground motion distributions. These kinematic simulations were developed using SPECFEM3D, a spectral element method (SEM) code that can incorporate detailed topographic surfaces (Komatitsch et al.; 2004). These simulations were only valid up to 3 Hz and thus, may not accurately predict PGA. Therefore, we used PGV to measure ground shaking, which should be accurately represented by the simulations. The mesh used had a variable element spacing, with average element sizes of 30 m at depths of 300 m or less, 100 m at depths between 300 and 1200 m, and of 300 m at depths greater than 1200 m. By incorporating a complex topography in the mesh, the model output allows consideration of the effect of topographic amplification or de-amplification (Meunier et al.; 2008). This surface topography had a resolution of 30 m and was based on a combined topography and bathymetry DEM of the Puget Lowlands (Finlayson; 2005).

The earthquake simulations use the Cascadia 3-D seismic velocity model (Stephenson et al.; 2017). This 3D velocity model includes sedimentary basins such as the Seattle Basin, as well as the first-order structure of the Seattle Fault. To account for near-surface site effects, a low velocity layer was placed in the upper 50–100 m of the model with a minimum shear wave velocity of 450 m/s. The source model was produced using the methods of Frankel et al. (2014), wherein the M7 earthquake sources were assigned randomly-seeded slip distributions with correlation lengths of 14.6 km along-strike and 6.9 km down-dip. The resulting slip distributions were mapped onto a 45°south-dipping plane. This roughly corresponds to the northernmost fault strand of Blakely et al. (2002). The final rupture zone had an along-strike extent of 43.8 km and a down-dip extent of 18.2 km, in accordance with the empirical scaling relationships of Wells and Coppersmith (1994). The up-dip limit of slip was at a depth of 3 km. To compare to our landslide inventory data, we consider 9 different M7 rupture scenarios (Table 2.1) based on a combination of three different slip distributions (Figure 2.4) and three different hypocenter locations (East, Center, and West), as described in detail by Stone et al. (2022).

2.7.2 Fitting the Temporal Landslide Model

The best fit landslide history model was chosen by minimizing error in three aspects. First, models were chosen so that the number of modelled landslides produced a similar number of expected preserved landslides as is observed in the landslide inventory. Second, the model results were compared to the dated landslide inventory both in a frequency and area based method. The differences between the data and the model were measured using the Root Mean Squared Log Error (RMSLE) and does not consider the most recent 400 years due to an anomalous increase in landslides with those ages. The best fit model was chosen to also minimize the RMSLE measured in both frequency and area. Figure 2.11 shows this error as a function of input parameters and indicates the final model used as a red point.

2.7.3 Scale Based Preservation Bias

For the temporal landslide models, we use a single power-law based preservation bias. However, it is possible that preservation bias is scale dependent. For example, over time, smaller landslides are more likely to be completely covered or removed than larger landslides. This would result in a stronger preservation bias for smaller landslides. To test this we calculate the frequency-area power law exponent (see Section 2.3) for the landslide inventory in 200 year windows (Figure 2.17). Whereas there is some variation, these values are all within error of the value we use: -1.8. If there was a scale-based preservation bias, there would be a trend in these values towards higher values at higher ages instead. There still might be a slight scale dependency on preservation bias, however it is too small to be detected in our dataset and minor enough to not affect our results.

2.7.4 Sadler Effect

The Sadler effect is based on the idea that erosional processes are stochastic in nature and have a heavy-tailed distribution of inter-event times (Sadler; 1981; Schumer and Jerolmack; 2009). In short this leads to different apparent rates (in this case, landslide rates) based on the time over which observations are collected. It is possible that the landslide inventory we present is subject to this effect. In order to test this hypothesis, we produce a Sadler plot of the landslide rate as a function of measurement interval (Figure 2.13). Here we see that the data can be fit by a power law with a scaling exponent (-0.53). This is indicative of a distribution impacted by the Sadler effect. However, this type of decrease in rate as a function of time may also be the result of a preservation bias. In particular, this may explain the drop off in landslide rates at high time intervals ($\geq 1,000$ years) that is even lower than the rate predicted by the fit to a power law function. As far as we are aware, no study so far has applied a Sadler effect to a landslide inventory and decoupled the effects of preservation bias and the Sadler effect. As such, it is beyond the scope of this work to attempt to deconvolve these two effects.

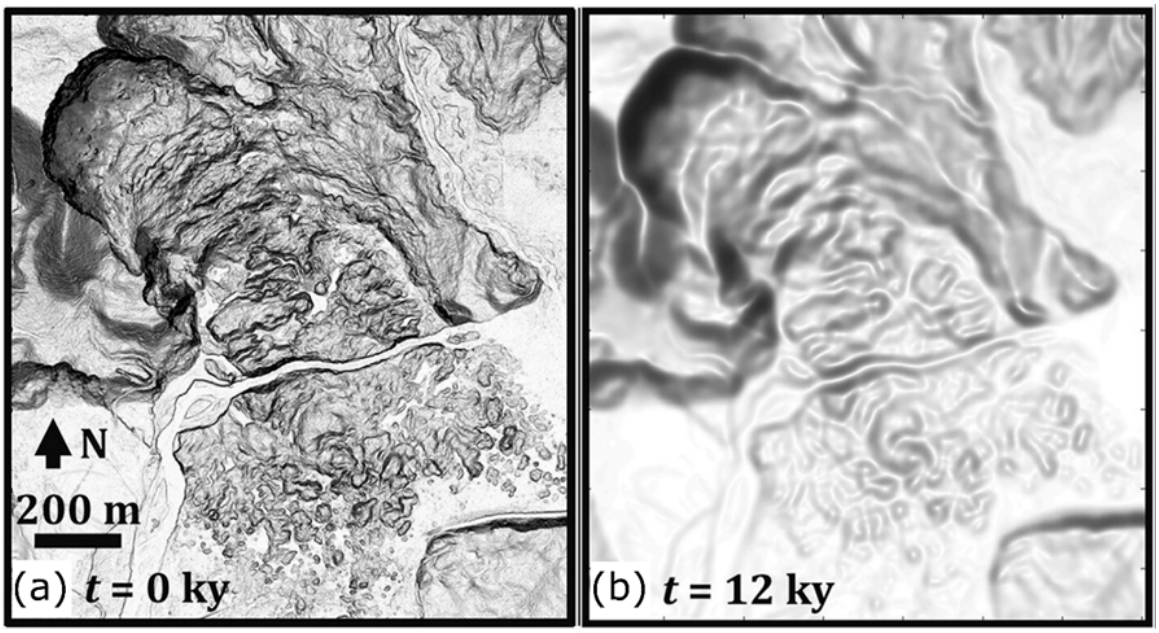

Figure 2.10: Slope maps of the surface evolution of the 2014 Oso landslide predicted by a nonlinear model of hillslope sediment flux. Figure a) is 2014 lidar data, while Figure b) is a model result of this same landscape after 12,000 years of non-linear hillslope diffusion. Adapted from Booth et al. (2017).

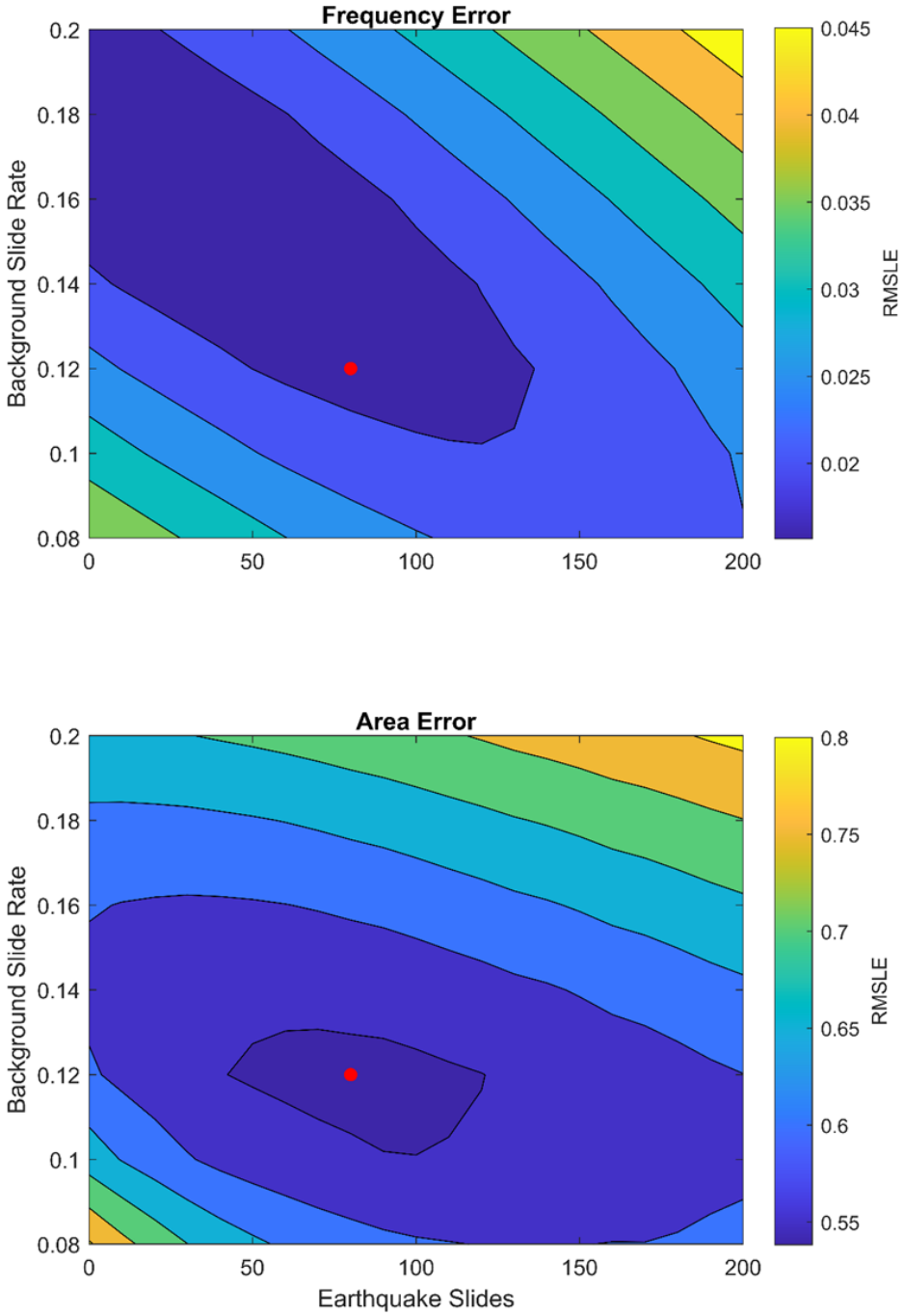

Figure 2.11: Contour maps of the error for different temporal landslide models. Error is measured as Root Mean Squared Log Error (RMSLE) for both the frequency (top) and area (bottom) based distributions (Figure 2.7). The red dot indicates the parameters used as a best fit to the data.

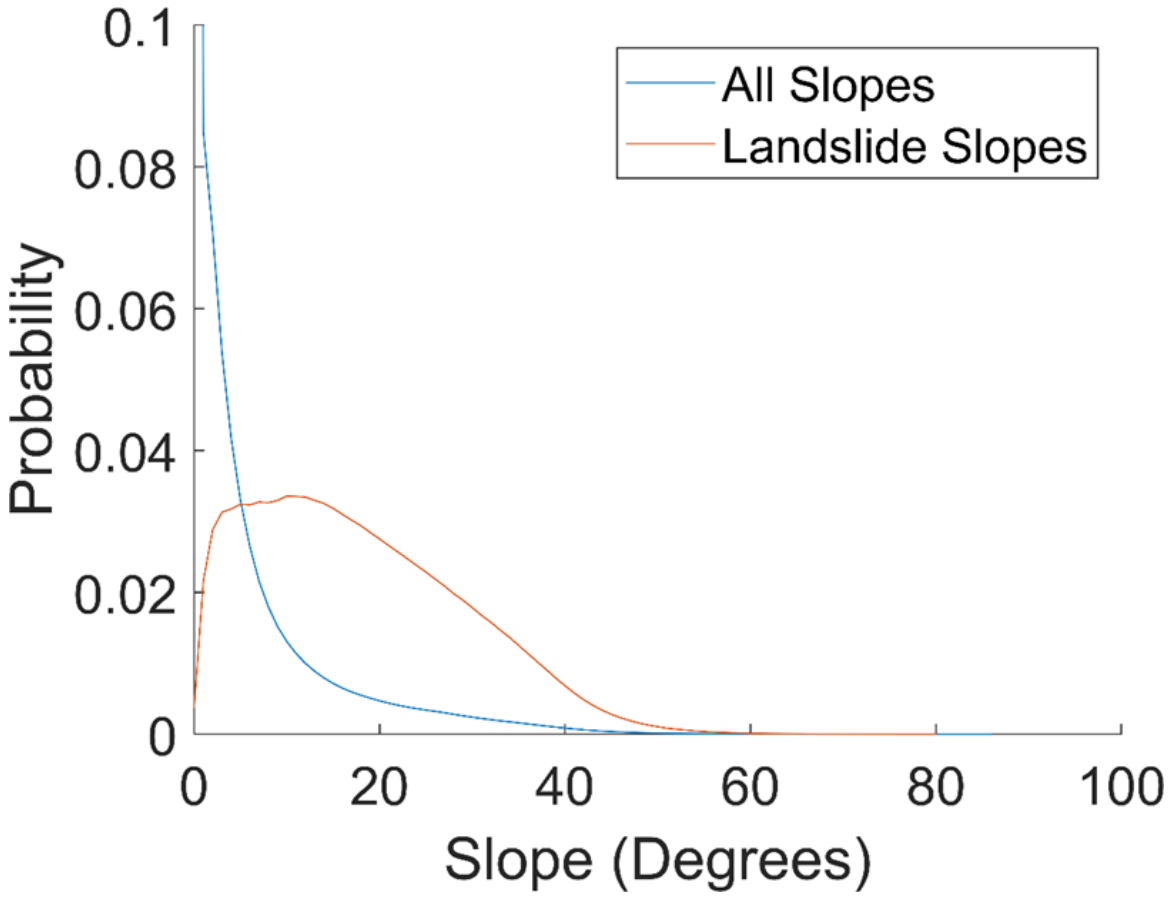

Figure 2.12: Distribution of all slopes in the study area (blue line) versus slopes with landslides (orange line).

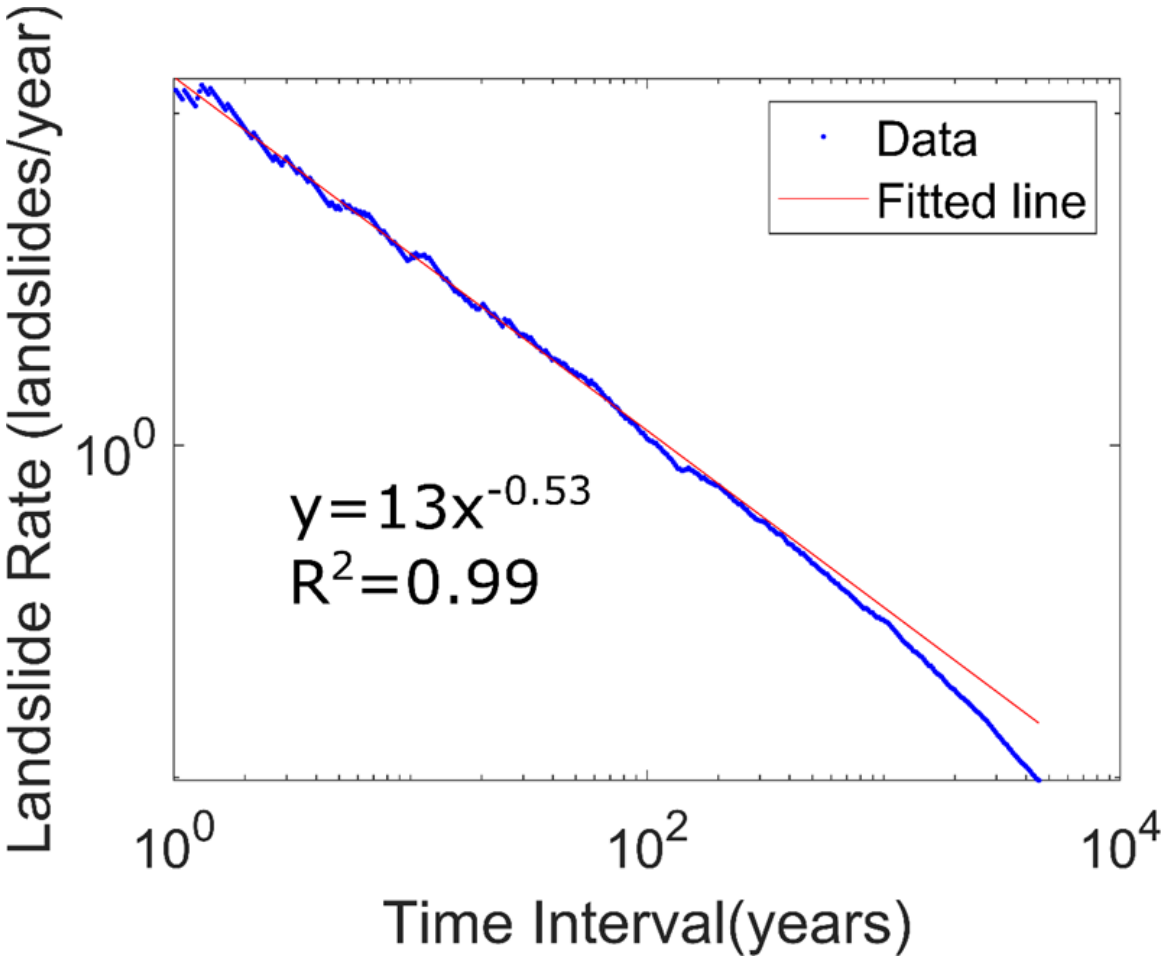

Figure 2.13: Sadler plot of landslide rate as a function of time interval (blue points). The data was fit to a power law function (red line).

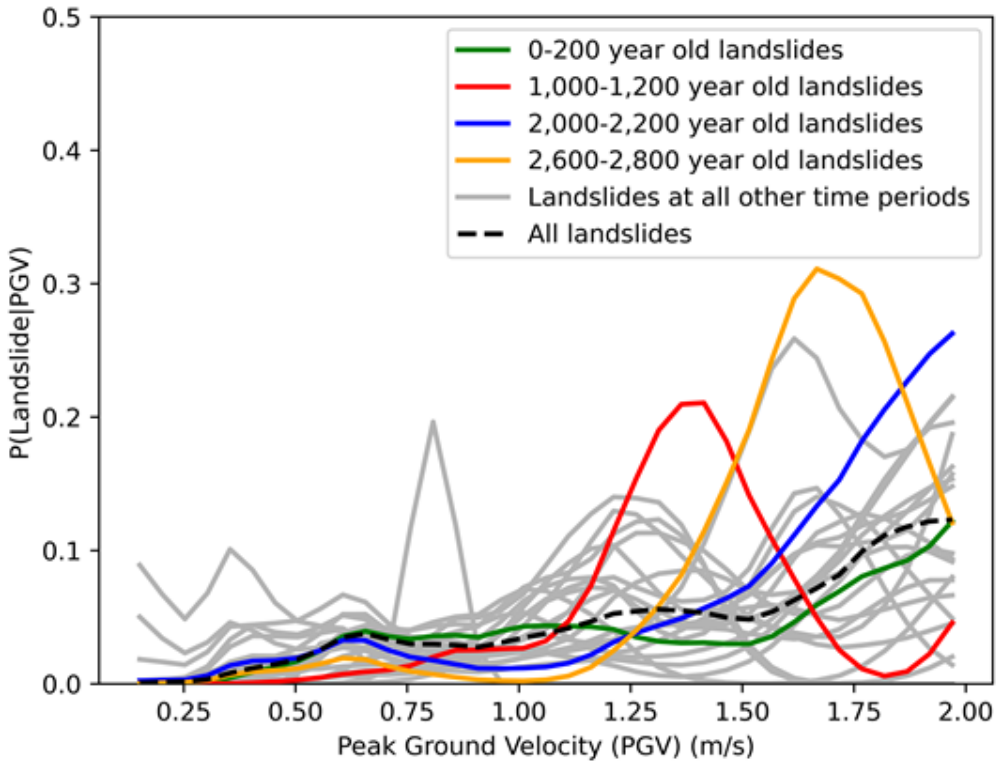

Figure 2.14: Conditional probability of landsliding as a function of mean peak ground velocity P(Landslides—PGV) at 200-year time slices. Highlighted time slices are in color: green for 0-200 yr B. P., red for 1,000-1,200 yr B. P., blue for 2,000-2,200 yr B. P., and yellow for 2,600-2,800 yr B. P. Other time slices from 4.6 – 0 ka are plotted in gray. The probability for entire time period plotted as a dashed black line. Peak ground velocity (PGV) is from the mean of all earthquake scenarios in units of m/s. The 0–200 time period represents a "null" scenario as no M7.0 earthquakes from faults in the region have been recorded, felt, or described during this time.

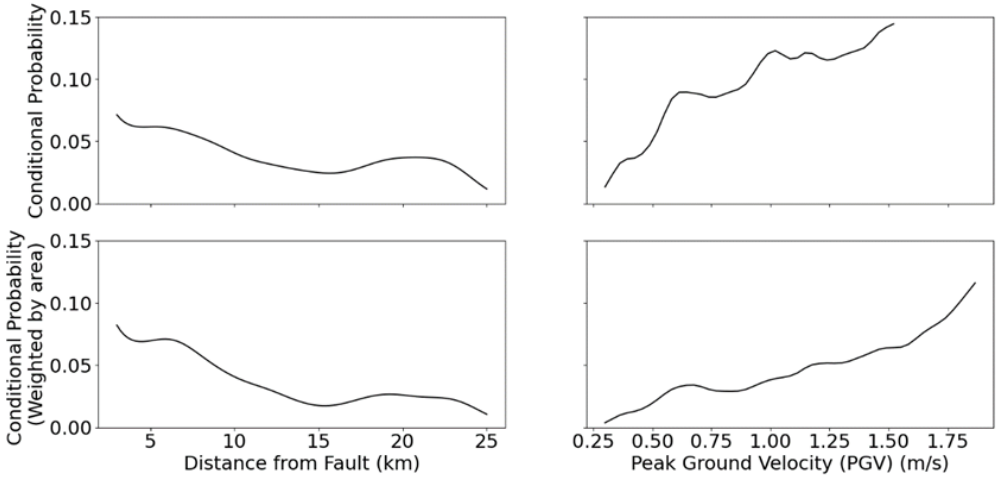

Figure 2.15: Conditional probability of landsliding based on distance from the fault (left) and peak ground velocity (right). These relationships are calculated based on number of landslides (top) and area of landslides (bottom).

Bibliography

Blakely, R., Wells, R., Weaver, C. and Johnson, S. (2002). Location, structure, and seismicity of the seattle fault zone, washington; evidence from aeromagnetic anomalies, geologic mapping, and seismic-reflection data, *Geological Society of America Bulletin* **114**: 169–177.

Booth, A., LaHusen, S., Duvall, A. and Montgomery, D. (2017). Holocene history of deep-seated landsliding in the north fork stillaguamish river valley from surface roughness analysis, radiocarbon dating, and numerical landscape evolution modeling, *Journal of Geophysical Research: Earth Surface* **122**(2): 456–472.

Finlayson, D. (2005). Combined bathymetry and topography of the puget lowland, washington state. Available at.
URL: *https://www.ocean.washington.edu/data/pugetsound/psdem2005.html.*

Frankel, A., Thorne, P. and Rohay, A. (2014). Three-dimensional ground-motion simulations of earthquakes for the hanford area, *Open-file report 2013-1289.*, USGS, Washington.

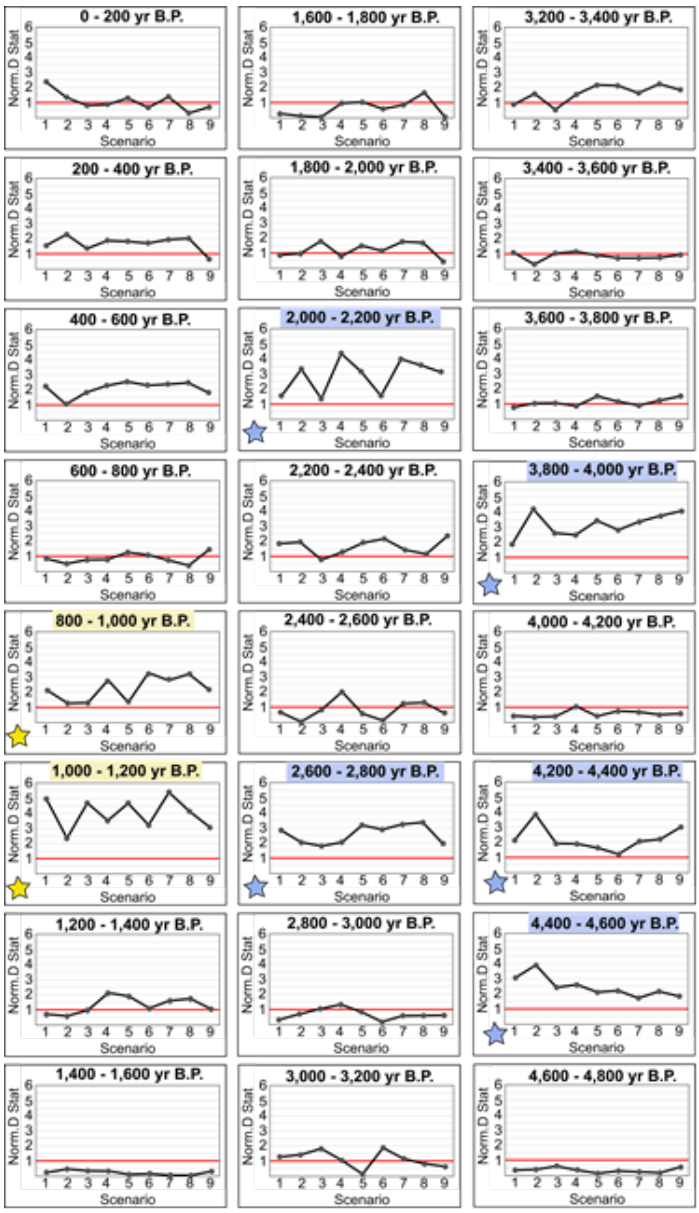

Figure 2.16: Plots showing the normalized D statistic (D statistic divided by the corresponding critical value) for the nine earthquake simulation scenarios for each 200-year time interval through 4,800 yr B. P. The red line shows a value of 1 for each plot. Values above one invalidate the null hypothesis and indicate earthquake forcing. See Section 2.4.4 for details. The plots with a yellow star overlap the time of the last Seattle Fault earthquake. Note the high value of the normalized D statistic for all scenarios. The plots with the blue stars indicate other intervals with consistently high normalized D statistics.

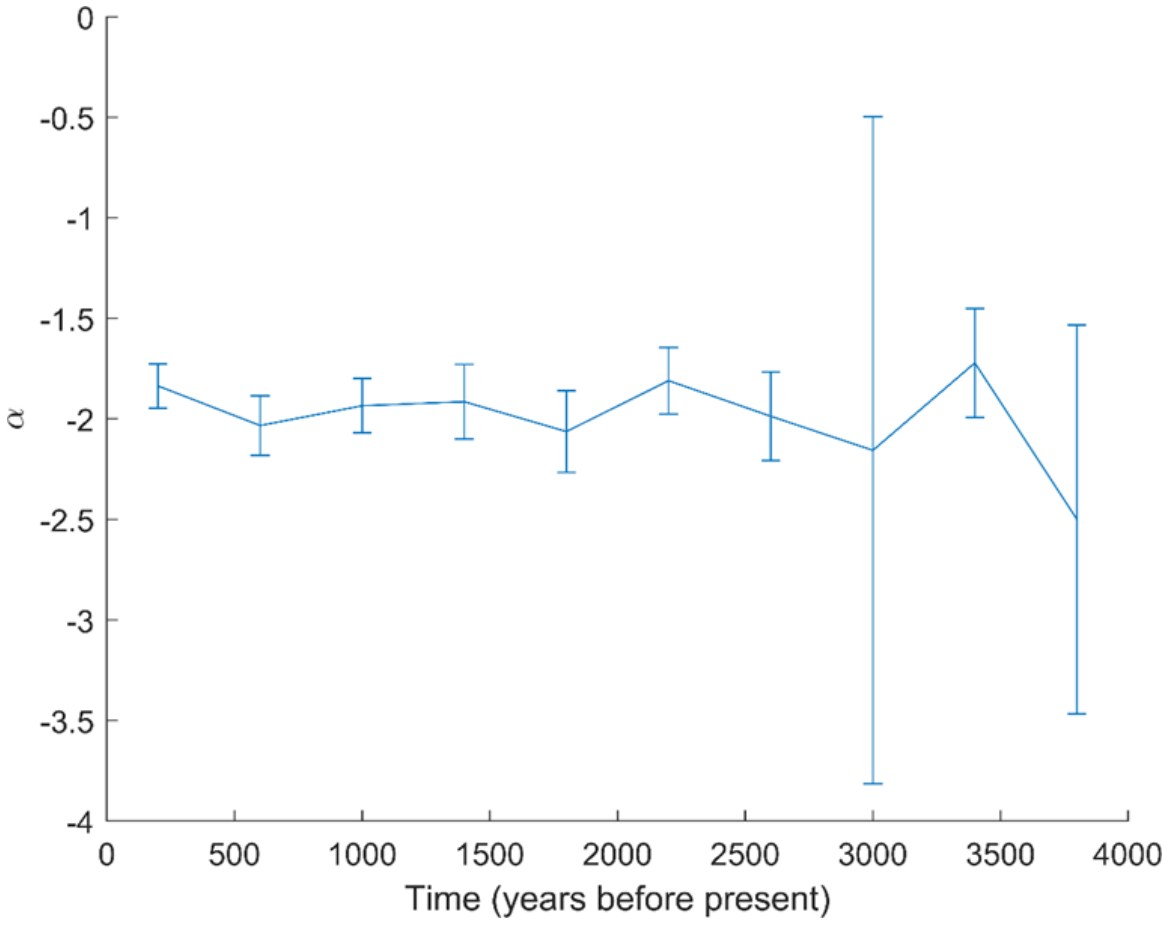

Figure 2.17: Plot of landslide area-frequency power law exponent α as a function of time, using 200 year windows. The 1σ error is represented as vertical bars. Constant values suggest that landslide size distribution does not vary between different sources.

Available at.
URL: *https://pubs.er.usgs.gov/publication/ofr20131289*

Komatitsch, D., Liu, Q., Tromp, J., Suss, P., Stidham, C. and Shaw, J. (2004). Simulations of ground motion in the los angeles basin based upon the spectral-element method, *Bulletin of the Seismological Society of America* **94**(1): 187–206.

Meunier, P., Hovius, N. and Haines, J. (2008). Topographic site effects and the location of earthquake induced landslides, *Earth and Planetary Science Letters* **275**(3-4): 221–232.

Sadler, P. (1981). Sediment accumulation rates and the completeness of stratigraphic sections, *The Journal of Geology* **89**(5): 569–584.

Schumer, R. and Jerolmack, D. (2009). Real and apparent changes in sediment deposition rates through time, *Journal of Geophysical Research: Earth Surface* **114**(F3).

Stephenson, W., Reitman, N. and Angster, S. (2017). P- and s-wave velocity models incorporating the cascadia subduction zone for 3d earthquake ground motion simulations—upyear for open-file report 2007–1348: Usgs open file report 2017-1152. Available at.
URL: *https://pubs.usgs.gov/of/2017/1152/ofr20171152.pdf*

Stone, I., Wirth, E. and Frankel, A. (2022). Topographic response to simulated m w 6.5–7.0 earthquakes on the seattle fault, *Bulletin of the Seismological Society of America* **112**(3): 1436–1462.

Wells, D. and Coppersmith, K. (1994). New empirical relationships among magnitude, rupture length, rupture width, rupture area, and surface displacement, *Bull. Seismol. Soc. Am* **84**(4): 974–1002.

Chapter 3

SIMULATED LANDSLIDE HAZARD FROM A SEATTLE FAULT EARTHQUAKE USING MULTIPLE SEISMIC SCENARIOS

Strong ground motion from a Seattle Fault earthquake could induce thousands of landslides on WA hillslopes known for their high precipitation induced landslide susceptibility. To understand controls on amount, style, and location of co-seismic slides in future earthquakes, we model landslide probability for 18 distinct Seattle Fault scenarios under both wet and dry conditions. Our simulations include both shallow translational and deep-seated rotational landslides, and a range of material properties for local glacial deposits. We find all scenarios result in significant landsliding, with more translational than rotational landslides (10% and 4% of slopes, respectively), on par with real world examples such as the 1994 Northridge CA earthquake. Comparison of our results to precipitation landslides and designated hazard zones yields (based on slopes and a history of landsliding) general spatial agreement. Our study shows the importance of local site effects, such as soil saturation and material strength, as these impacted modeled landslides more than earthquake magnitude (M7 vs M6.5) and hypocenter location.

3.1 Introduction and Study Area

Earthquake induced landslides are a major secondary hazard of earthquakes (Keefer; 1984; Jibson and Keefer; 1993; Malamud et al.; 2004). In many cases these landslides can change the landscape and cause more loss of life than the shaking from the earthquake itself. It is thus important for hazard estimations to understand the potential magnitude and spatial patterns of landsliding induced by future earthquakes. Studies of landslides mapped after earthquakes in Kaikoura, New Zealand (Massey et al.; 2018) and Northridge, USA (Dreyfus et al.; 2013) find that properties such as geologic strength of underlying units, local slope, and the strength of earthquake shaking are the main controls on where these landslides occur.

Seattle, Washington, USA (Figure 3.1), is a landslide prone region (Laprade et al.; 2000; Survey; 2020). High landslide susceptibility stems from a combination of steep slopes underlain by weak glacial deposits (Tubbs; 1974; Schulz; 2007; Perkins et al.; 2017), a wet maritime climate, proximity to earthquake-producing faults, and human activity. Compilations of historical landslides (Laprade et al.; 2000; Survey; 2020; Davis et al.; 2022b) show a predominance of precipitation-induced landslides in this region, though some landslides are earthquake induced. For example, the 2001 M6.8 Nisqually earthquake induced dozens of landslides in the area (Highland; 2003). A Seattle Fault Earthquake is expected to induce many more landslides, posing a a greater hazard, (Allstadt et al.; 2013) due to its location, being located directly under the city of Seattle, and at a shallow depth unlike the deep 2001 Nisqually earthquake. Though, since an earthquake on the Seattle Fault has not occurred in the modern historical record, we do not have a clear understanding of how many landslides might occur and where they might occur. While it is possible to indirectly measure these values for past earthquakes based on ancient landslide distributions (Herzig et al.; 2023), forward models will likely produce more accurate estimates of this landslide hazard.

The Seattle Fault Zone [SFZ] consists of multiple fault strands intersecting Seattle and surrounding populated regions and is a major contributor to local seismic hazard (Petersen et al.; 2020). While the Seattle Fault has not had a major earthquake since 924 CE (Black et al.; 2023), a time well before modern instrumentation and historical records, several lines of evidence support the interpretation of widespread seismically induced landsliding. Supporting evidence includes native oral histories (Ludwin et al.; 2005), dated landslide deposits in Lake Washington (Jacoby et al.; 1992) and a recent study combining dating and modeling of deep-seated landslides from across the region (Herzig et al.; 2023). Important early work by (Allstadt et al.; 2013) combined computed broadband synthetic seismograms for a Seattle Fault rupture with an estimation of shallow landsliding using the Newmark method (Newmark; 1965; Jibson; 1996; Jibson et al.; 2000). Their results indicated extensive landsliding triggered by a simulated M7 Seattle Fault earthquake and that water saturation (wet slopes vs. dry slopes) was a major driver of magnitude of hillslope failure in such an event.

This study builds on Allstadt et al. (2013), obtaining new estimates of magnitude and

distribution of potential Seattle Fault earthquake induced landslides by combining multiple earthquake scenarios (Stone et al.; 2022b) with a multimodal landslide model (Grant; 2017; Pollock et al.; 2019a) under realistic soil saturation conditions (Jeschke D and A; n.d.) and engineering properties for site conditions (Troost and Booth; 2008). For the earthquake ground motions, we use a set of 18 3D kinematic Seattle Fault earthquake scenarios (Stone et al.; 2022b). These scenario earthquakes are either M6.5 or M7 for three different hypocenter locations and three different slip distributions. All scenarios include the effects of topographic amplification on the ground motions. The ground shaking from these scenarios is input into a multi-modal landslide model that includes both translational shallow and rotational deep failure styles (Grant; 2017; Pollock et al.; 2019a) to produce a map of induced landslide probabilities for each scenario. Translational and rotational landslides are the two primary types of landslides for the field site (Laprade and Tubbs; 2008). We compare our new modeled landslide inventories to Allstadt et al. (2013), to a recently published modern landslide inventory for the city of Seattle (Davis et al.; 2022a) and to previously designated landslide hazard areas, to assess if earthquake induced landslides will be as widespread as originally thought and in similar locations to the primarily precipitation induced landslides common to the region.

3.2 Methods

We use ground motions from eighteen simulations of Seattle Fault earthquakes: nine different M7 earthquake scenarios and nine different M6.5 earthquake scenarios (Stone et al.; 2022a). These kinematic simulations were developed using SPECFEM3D, a spectral element method (SEM) code that can incorporate detailed topographic surfaces (Komatitsch et al.; 2004). The mesh used had variable element spacing, with average element sizes of 30 m at depths of 300 m or less, 100 m at depths between 300 and 1200 m, and of 300 m at depths greater than 1200 m. By incorporating a complex topography in the mesh, the model output allows consideration of the effect of topographic amplification or de-amplification (Meunier et al.; 2008). This surface topography had a resolution of 30 m and was based on a combined topography and bathymetry DEM of the Puget Lowlands (Finlayson; 2005).

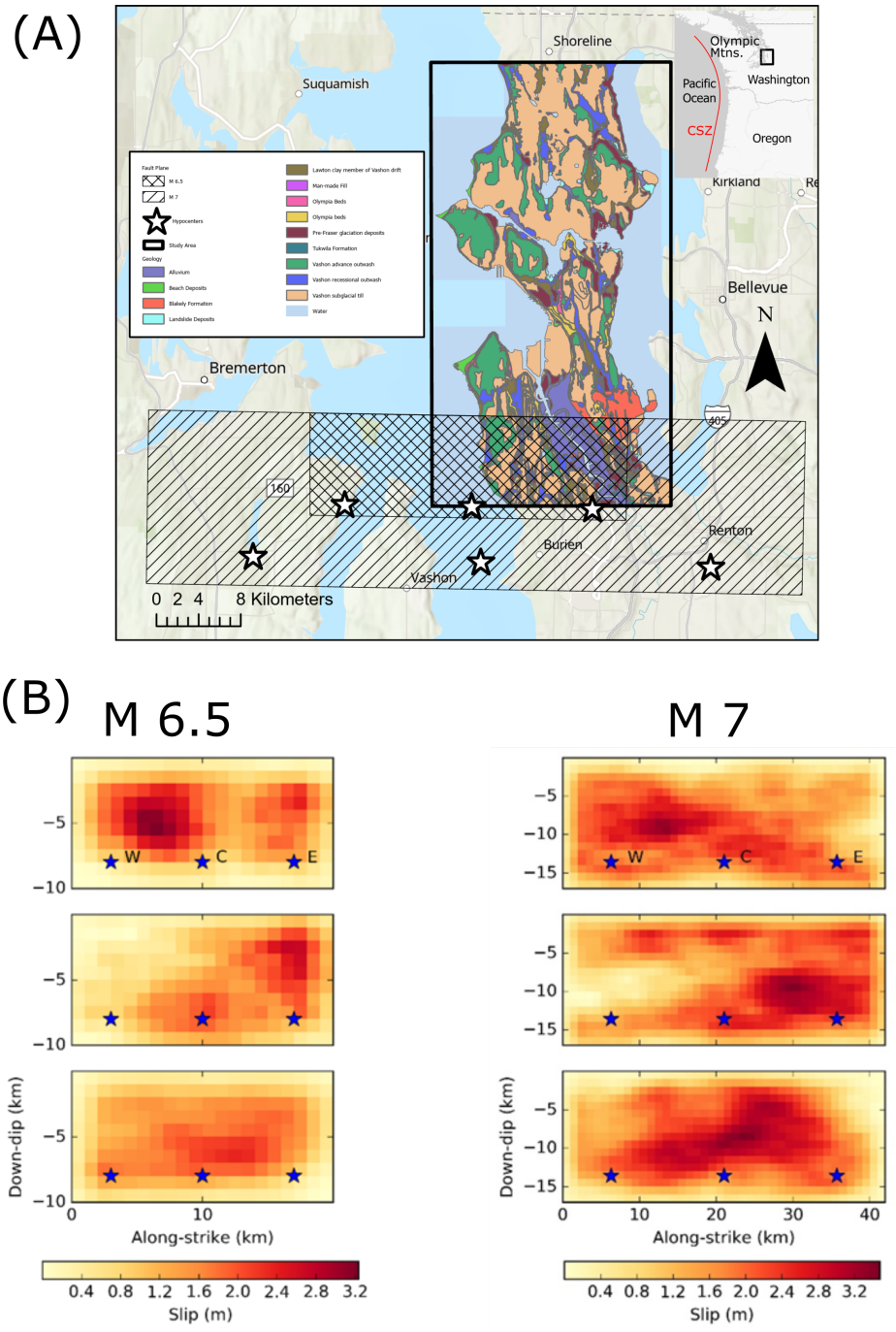

Figure 3.1: (A) Map of study area (black box), with fault planes for M6.5 (crosshatched box) and M7 (single hatched box) earthquake scenarios, and hypocenters as white stars. (B) Plots of slip on the fault plane for both M6.5 (left) and M7 (right) earthquake scenarios. Higher slip is red, lower slip is yellow, hypocenters as blue stars.

All rupture scenarios are based on a combination of three different slip distributions (Figure 3.1) and three different hypocenter locations (East, Center, and West), described in detail by Stone et al. (2022a). The three slip distributions were randomly generated but can roughly be described as slip concentrated in the east (distribution 1), in the west (distribution 2), and in the central portion of the rupture (distribution 3) (Figure 3.1 B). Additionally, although the slip distributions are similar between M7 and M6.5 scenarios, our M6.5 scenarios have a smaller rupture area than the M7 scenarios. Both rupture areas have the same updip edge, but the M7 scenarios extend deeper down dip, this leads to relatively more slip concentrated near the surface in the M6.5 scenarios.

Landscape response to strong ground motion was determined using a modified version of the multimodal landslide model developed by Pollock et al. (2019b) and Grant and Wartman (2017). This model estimates the factor of safety of slopes in the study for two styles of landslide failure: translational and rotational. For computational efficiency, translational landslides were only modeled on slopes steeper than 15°, while rotational landslides were modelled on slopes between 10° and 35°. Factor of safety is based on a 0.9m 2016 King County LIDAR based digital elevation model, down-scaled to 10m resolution (see supplement for details). Troost and Booth (2008) was used as a map of geologic units in the area. In order to account for the difference in strength between colluvium and bedrock, we use a set of two different material properties as in Pollock and Wartman (2020). These values are based on initial values from Harp et al. (2008) that have been adjusted within possible bounds (Savage et al.; 2000; Debray and Savage; 2001; Baum and Godt; 2010; Brien and Reid; 2008; Godt and McKenna; 2008) so that mean strength parameters result in a static factor of safety greater than one at initial conditions (see supplement). Depth to the top of the water table was calculated as a function of land surface elevation for both wet (average winter water table depths) and dry (average summer water table depths) conditions (see supplement). This was based on 630 well logs from the Washington Department of Natural Resources Subsurface Database (Jeschke D and A; n.d.).

Landslide occurrence was modelled on a pixel by pixel basis, using the Newmark method (Newmark; 1965) as described in Strenk and Wartman (2011). For each pixel, we calculated a critical acceleration for failure based on the calculated factors of safety using the equation

$a_c = (FS–1)gsin\alpha$, where a_c is the critical acceleration, FS is the factor of safety, g is the force of gravity, and α is the slope. Newmark displacement is calculated by measuring the acceleration above this critical acceleration at each pixel and integrating it twice to get a displacement. Before this integration, we also add a deceleration when the earthquake ground motions do not exceed the critical acceleration, to get the slide body to 'stop' until it again experience accelerations exceeding the critical acceleration. For each pixel, coseismic displacements over 5cm for translational slides and 15cm for rotational slides, are considered failures, as in Grant and Wartman (2017).

3.3 Results

For the 18 earthquake scenarios, the percentage of vulnerable slopes that failed with rotational failures ranges from 1.5% to 10.5% over all considered conditions such as both dry and wet conditions, with an average value of 4%. For translational slope landslides this percentage ranges from 1.7% to 27.7%, with a mean value of 10.6%. For comparison, the translational slope results from Allstadt et al. (2013) have 5.5% and 44% for wet and dry conditions respectively. These values are modified to account for the different cell sizes and methods of calculating landslide failure. There is a slightly different pattern between the modeled rotational landslides and translational landslides, with more translational landslides on the western side of the study area, and rotational landslide being more uniformly distributed.

Figure 3.2 shows a heat map of modeled landslides averaged over all of the scenarios. Translational slope failures and rotational failures are shown separately in A) and B), and combined in C). The hatched areas represent the areas identified by the City of Seattle as landslide prone regions based on both slope and a history of past landslides. Generally, the modeled landslides fall within these hazard areas, and the hazard areas have at least some modeled landslides, though there are some exceptions. The Thornton creek area is marked as a landslide hazard area by the city, but almost no modeled earthquake induced landslides populate this region. Within and near to Seward Park, our model results predict coseismic landslides, yet the this region is not designated as a landslide hazard zone. Our study area extends farther north than the city limits and the limits of the hazard areas, which explains

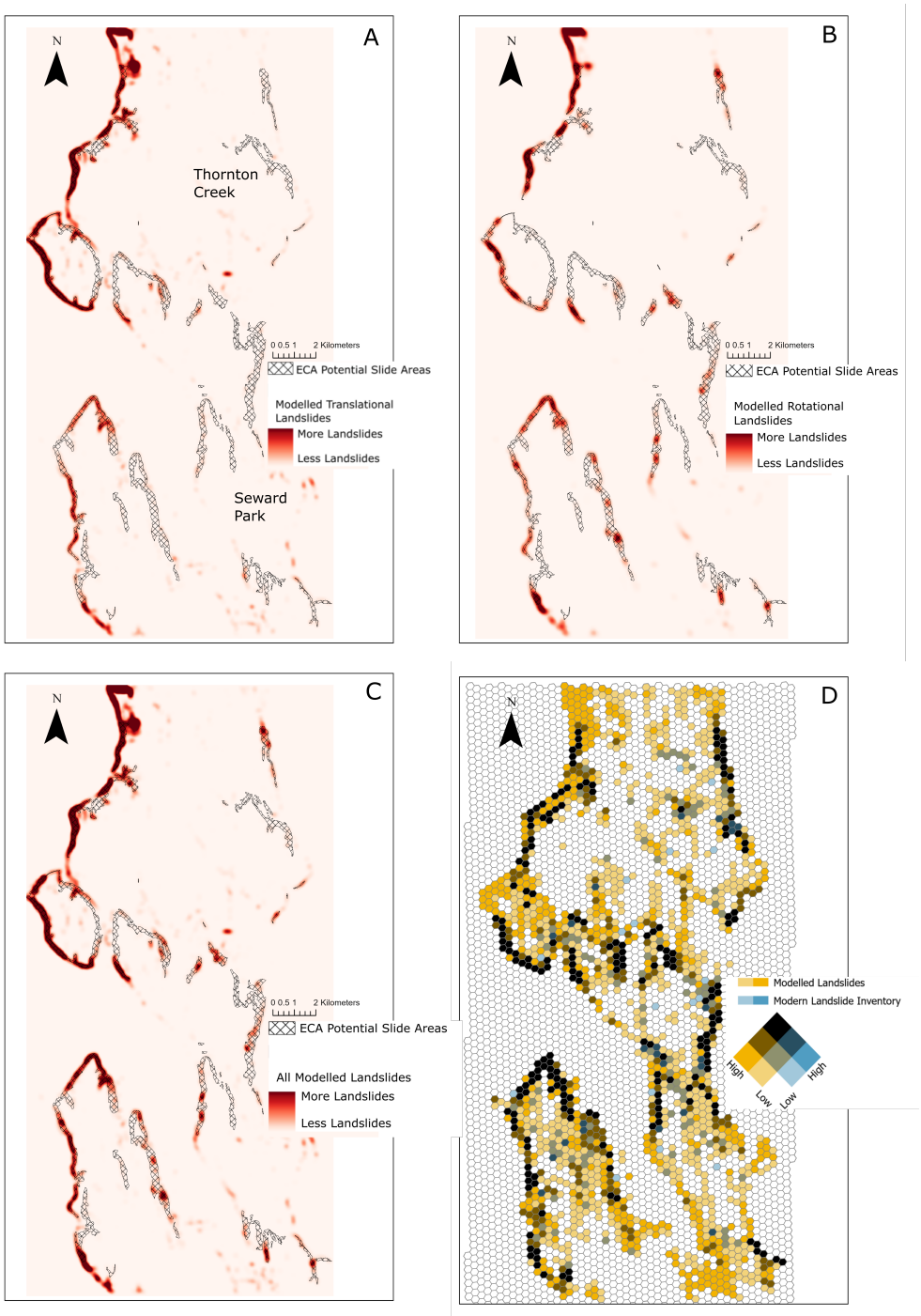

Figure 3.2: Comparison between modeled Seattle Fault earthquake induced (A) translational landslides, (B) rotational landslides, and (C) both rotational and translational landslides and City of Seattle landslide hazard areas. Red areas indicate areas with modeled landslides, hatched areas are Seattle landslide hazard areas. (D) Compares both styles of modeled landslides and a modern landslide inventory (Davis et al.; 2022b). Yellow areas indicate areas with mostly more modeled landslides, blue areas indicate more landslides in the modern inventory, dark brown indicates areas with high amounts of landslides in both, white indicates fewer landslides in either.

a lack of noted hazard in the clear hot spot of modeled landslides in the north.

Figure 3.2 D compares this average modeled landslide distribution to a modern Seattle Landslide Inventory (Davis et al.; 2022b). Hexagon color indicates if the area contains modeled landslides, modern inventory landslides (Davis et al.; 2022b), both or neither. There is more disagreement here than with the hazard areas in 3.2, with many more areas with modeled landslides than inventory landslides. This is likely due to how the modern inventory was collected, with landslides being mapped only when they are reported. In green spaces, it is possible that modern landslides have occurred but have not been reported. Most of the areas of disagreement are in these areas, and excluding them, there is general agreement between the modeled and modern inventory. However, the Thornton Creek and Seward Park discrepancies described above persist when comparing modeled landslides to modern inventory landslides.

Figure 3.3 compares the percentage of steep slopes with modeled landslides for various considered scenarios. The plots represent a kernel density estimation of the percentage of steep slopes where we model landslides under different conditions. In all cases there are approximately double the amount of slopes impacted by translational landslides than rotational ones. On average 10% slopes are failing in translational slides and 4% of slopes are failing in rotational slides. Note that these locations may overlap, with both styles of landslide possibly occurring in the same location.

Figure 3.3A shows the difference between modeled landslides under summer and winter water table conditions over all earthquake scenarios. As expected, wet conditions lead to a higher average percentage of slopes with landslides, though this difference is less extreme than previous studies find (Allstadt et al.; 2013).

Figure 3.3B shows the difference between landslides after M6.5 and M7 scenario earthquakes. For translational slides there are a greater percentage of slopes with landslides in M7 scenarios, while for rotational slides there is a slightly higher proportion of slopes with landslides in M6.5 scenarios. Though in both cases this is a minor change, and the distributions are almost the same. Figure 3.3C shows the difference between landslides modeled with scenario earthquakes with slip in the west, center and east of the fault. Generally, all these scenarios result in similar areas of landsliding, though there are slightly less slopes

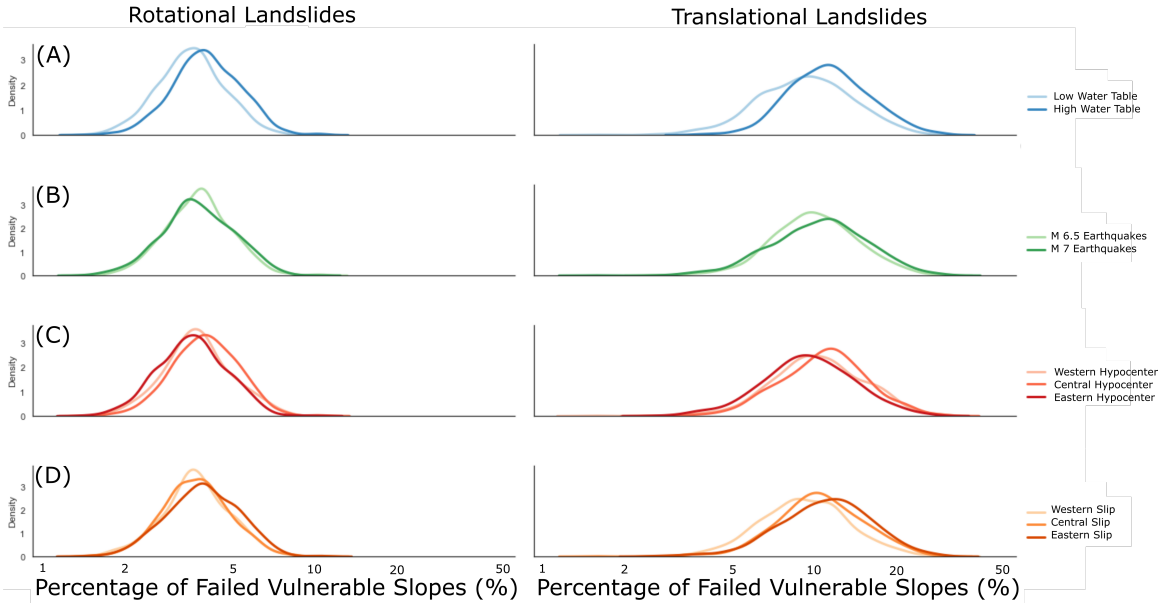

Figure 3.3: Kernel density plots of percentage of steep slopes that have modeled rotational (left) and translational (right) landslides. (A) compares between different water table levels, light blue lines are dry, summer, low water tables and the dark blue lines lines are wet, winter, high water tables. (B) compares between different magnitude earthquake scenarios, light green lines are M 6.5 earthquake scenarios and the dark green lines are M 7 earthquake scenarios. (C) compares between earthquake scenarios with different hypocenters, light red lines are western hypocenter scenarios, the mid red lines are central hypocenter scenarios and dark red lines are eastern hypocenter scenarios. (D) compares between earthquake scenarios with different slip distributions, light orange lines are western slip distribution scenarios, the mid orange lines are central slip distribution scenarios and dark orange lines are eastern slip distribution scenarios.

with landslides for a western slip distribution. Figure 3.3D shows the difference between landslides after scenario earthquakes with hypocenters in the west, center and east of the fault. These scenarios result in similar percentages of slopes with landsliding, though there are slightly lower values for eastern hypocenters.

3.4 Discussion

Results from the 18 analyzed earthquake scenarios and the multimodal landslide modeling show average percentages of modeled translational landslides 10% falling between the values 6% and 44%, covering large parts of the study area and on par with results from a single Seattle Fault earthquake scenario (Allstadt et al.; 2013). For both failure styles, increased saturation during winter conditions leads to an increase in landslides across the study area, which also agrees with Allstadt et al. (2013). As the last major Seattle Fault earthquake recorded by Black et al. (2023) occurred in the winter, we assume that it also induced a high number of landslides, similar to modeled winter scenarios. Favorable seasonal conditions for landslides might be one reason that we see interpreted earthquake-induced landslide deposits still remaining in the landscape, even 1000 years later (Herzig et al.; 2023).

In all of the earthquake scenarios we considered, there are roughly double the amount of translational landslides as rotational landslides, with 10% slopes failing in translational slides and 4% of slopes failing in rotational slides (Figure 3.2). This suggests that any future Seattle Fault earthquake would produce widespread landsliding. Both styles of landslide occur mainly on the steep slopes of the study area, though translational slides are more concentrated on the western side of the study area (Figure 3.2A), and rotational slides (Figure 3.2B) are more evenly distributed. For comparison, the 1994 Northridge CA earthquake induced landslides on approximately 3.4% of slopes in the Santa Susana Mountains (the area most heavily impacted by earthquake induced landslides) (Harp and Jibson; 1996). The landslides induced by the Northridge CA earthquake were unevenly distributed, with more landslides occurring in areas with weak rocks and steep slopes, such as the Santa Susana Mountains (Harp and Jibson; 1996).

Our study was designed to consider how hillslope response to shaking differed among variable earthquake magnitudes and slip distributions. With the caveat that our analysis

of landslides generated under different magnitude earthquakes was limited to a comparison of just M6.5 and M7.0, our findings suggest that the hillslope response to both earthquake magnitudes is similar, but with some interesting differences. For translational slides, M6.5 scenarios have less landslides than M7 scenarios (Figure 3.3A). However, for rotational slides, M6.5 scenarios have slightly more landslides than M7 scenarios. This difference can likely be explained by spatial differences between locations of cells where translational versus rotational landslides occur in our models (Figure 3.3A). Rotational slides are isolated to mostly shoreline slopes, while translational slides occur across a larger area. While the M7 scenarios generally have stronger ground motions, it is possible that due to directivity effects (Stone et al.; 2022a), some areas may experience stronger shaking in the M6.5 scenario earthquakes. As an example, in the area around Discovery Park (Figure S1), more modeled translational and rotational slides occurred for M6.5 scenarios. This is due to stronger ground motion in that area in the M6.5 scenarios, likely due to directivity. While directivity affects both styles of landsliding, the affected area represents a larger portion of the area prone to rotational slides than the area prone to translational slides and slightly more rotational than translational landslides for M6.5 scenarios are modeled as a result (Figure S1).

While the energy released by M7 and M6.5 earthquakes differs by a factor of 3, the modeled amount of landsliding is similar in both cases, with some locations even experiencing more landslides in the M6.5 earthquakes than the M7 ones. This finding presents an important reminder that in a single location, it is possible that a smaller magnitude local earthquake may produce stronger shaking than a larger one. Additionally, if that location is landslide prone compared to the rest of a region, a smaller earthquake can even induce more landslides than a larger earthquake. If we just focus on the largest earthquakes in a landslide hazard analysis, we may under-predict the possibilities, as these smaller earthquakes can be just as dangerous with respect to the hillslopes and are more frequent than the largest earthquakes. However, we must also be clear that our study area focuses on the area closest to the fault, and while there might be elevated numbers of landslides in M6.5 scenarios in our study area, it is also likely that an M7 earthquake would cause strong shaking over a larger area in comparison, and would thus induce more landslides overall when considering

a larger spatial footprint. Moreover, it is important to note that the 18 earthquake scenarios that we used represent a small selection of possible earthquake ruptures, and thus we must be careful when generalizing whether M6.5 earthquakes or M7 earthquakes would induce more or fewer landslides.

In terms of our analysis of earthquakes with different spatial patterns in slip distribution, we find that slip in the west leads to less modeled landslides, while slip in the center or east produce similar amounts of landslides (Figure 3.3C). We suggest this relates less to earthquake or hillslope properties and more to the chosen study area, which sits over the eastern end of the Seattle Fault. Slip concentrated in the west should affect hillslopes, but the shaking would be concentrated out of the study area, to the west. The position of the fault with respect to the study area can also explain why we see less landslides in an eastern hypocenter scenario (Figure 3.3D). This is because directivity effects can amplify shaking away from the hypocenter and along the fault. An eastern hypocenter is thus amplifying shaking in the west, which is out of the study area.

The Monte Carlo modelling of rock strength causes a large proportion of the variance in the number of modelled landslides. This variation in modelled landslides due to rock strength is greater than the difference between wet and dry conditions. This represents small scale variations in rock strength that we cannot directly map or model. This high variance then suggests that local site conditions are equally if not more important for determining if a landslide will occur than saturation level or earthquake properties, such as magnitude (at least between magnitude 6.5 and 7), hypocenter, and slip. This finding also agrees with other studies finding geologic strength strongly controls where earthquake induced landslides occur (Dreyfus et al.; 2013; Massey et al.; 2018). Together, our study shows local geologic strength and water saturation level as the main factors controlling how many landslides an earthquake generates. Our results also demonstrate the utility of coupled earthquake and landslide simulations for estimating landslide hazards, as well as for assessing the relative importance of different input parameters on the resulting hazard model.

3.5 Conclusions

We modeled multimodal landslide probability under 36 different Seattle Fault earthquake scenarios. We considered both summer and winter water saturation levels, and magnitude 6.5 and 7 earthquakes with 3 different slip distributions and 3 different hypocenters. The multi-modal landslide model considered both shallow translational landslides and deep-seated rotational landslides. Averaging over all these scenarios, we find that modeled earthquake induced landslides tend to occur in similar places as modern precipitation induced landslides (Davis et al.; 2022b) and in zones marked by the city of Seattle as landslide prone. This agrees with previous work by Allstadt et al. (2013) that only considered a single scenario of a Seattle Fault earthquake and did not include topographic effects. Additionally, we find that in these locations, a large number of slopes (10% slopes in translational slides and 4% of slopes in rotational slides) slide from an earthquake. The largest difference between scenarios is due to soil saturation level, with more saturated conditions leading to more modeled landslides. This also agrees with previous work by Allstadt et al. (2013). However, within a single scenario, rock strength parameters, representing local variations in strength, account for a large amount of variation in the number of modeled landslides. Earthquake magnitude (at least between M6.5 and M7 earthquakes) does not have as large an effect as variations in geologic strength or water table level. This is partly due to limitations of this study in both study area and the number of scenarios considered. However, it is a reminder that for a small area such as the City of Seattle, a smaller earthquake might not be safer than 'the big one'. 'The smaller one' could be just as damaging, and is worth preparing for.

Bibliography

Allstadt, K., Vidale, J. E. and Frankel, A. D. (2013). A scenario study of seismically induced landsliding in seattle using broadband synthetic seismograms, *Bulletin of the Seismological Society of America* **103**(6): 2971–2992.

Baum, R. L. and Godt, J. W. (2010). Early warning of rainfall-induced shallow landslides and debris flows in the usa, *Landslides* **7**: 259–272.

Black, B. A., Pearl, J. K., Pearson, C. L., Pringle, P. T., Frank, D. C., Page, M. T., Buckley, B. M., Cook, E. R., Harley, G. L., King, K. J. et al. (2023). A multifault earthquake threat for the seattle metropolitan region revealed by mass tree mortality, *Science advances* **9**(39): eadh4973.

Brien, D. L. and Reid, M. E. (2008). Assessing deep-seated landslide susceptibility using 3-d groundwater and slope-stability analyses, southwestern seattle, washington.

Davis, E., Chang, S., Hou, S., Teal, T., Cowell, K. and Garcia-Arceo, S. (2022a). A century of landslides in seattle, washington: Coalescing and digitizing the city's historic landslide inventories, *Environmental and Engineering Geoscience* **28**(4): 335–346.

Davis, E. J., Chang, S., Hou, S., Teal, T., Cowell, K. and Garcia-Arceo, S. (2022b). A century of landslides in seattle, washington: Coalescing and digitizing the city's historic landslide inventories, *Environmental & Engineering Geoscience* **28**(4): 335–346.

Debray, S. and Savage, W. Z. (2001). *A preliminary finite-element analysis of a shallow landslide in the Alki area of Seattle, Washington*, US Department of the Interior, US Geological Survey.

Dreyfus, D., Rathje, E. M. and Jibson, R. W. (2013). The influence of different simplified sliding-block models and input parameters on regional predictions of seismic landslides triggered by the northridge earthquake, *Engineering geology* **163**: 41–54.

Finlayson, D. (2005). Combined bathymetry and topography of the puget lowland, washington state, university of washington.

Godt, J. W. and McKenna, J. P. (2008). Numerical modeling of rainfall thresholds for shallow landsliding in the seattle, washington, area.

Grant, A. (2017). Regional-scale coseismic landslide hazard modeling and consequence analysis.

Grant, A. and Wartman, J. (2017). Regional-scale coseismic landslide hazard modeling and consequence analysis.

Harp, E. L. and Jibson, R. W. (1996). Landslides triggered by the 1994 northridge, california, earthquake, *Bulletin of the Seismological society of America* **86**(1B): S319–S332.

Harp, E. L., Michael, J. A. and Laprade, W. T. (2008). Shallow landslide hazard map of seattle, washington.

Herzig, E., Duvall, A., Booth, A., Stone, I., Wirth, E., LaHusen, S., Wartman, J. and Grant, A. (2023). Evidence of seattle fault earthquakes from patterns in deep-seated landslides.

Highland, L. (2003). *An account of preliminary landslide damage and losses resulting from the February 28, 2001, Nisqually, Washington, Earthquake*, Citeseer.

Jacoby, G., Williams, P. and Buckley, B. (1992). Tree ring correlation between prehistoric landslides and abrupt tectonic events in seattle, washington, *Science* **258**(5088): 1621–1623.

Jeschke D, Eungard D, T. K. and A, W. (n.d.). Subsurface database of washington state-gis data, *Technical report*, Washington Division of Geology and Earth Resources Digital Data Series 11, version 1.2.

Jibson, R. (1996). Use of landslides for paleoseismic analysis, *Engineering geology* **43**(4): 291–323.

Jibson, R. and Keefer, D. (1993). Analysis of the seismic origin of landslides: examples from the new madrid seismic zone, *Geological Society of America Bulletin* **105**(4): 521–536.

Jibson, R. W., Harp, E. L. and Michael, J. A. (2000). A method for producing digital probabilistic seismic landslide hazard maps, *Engineering geology* **58**(3-4): 271–289.

Keefer, D. (1984). Landslides caused by earthquakes, *Geological Society of America Bulletin* **95**(4): 406–421.

Komatitsch, D., Liu, Q., Tromp, J., Suss, P., Stidham, C. and Shaw, J. H. (2004). Simulations of ground motion in the los angeles basin based upon the spectral-element method, *Bulletin of the Seismological Society of America* **94**(1): 187–206.

Laprade, W., Kirkland, T., Nashem, W. and Robertson, C. (2000). Seattle landslide study. shannon & wilson, *Technical report*, Inc. Internal Report W-7992-01.

Laprade, W. T. and Tubbs, D. W. (2008). Landslide mapping in seattle, washington.

Ludwin, R., Thrush, C., James, K., Buerge, D., Jonientz-Trisler, C., Rasmussen, J. and Los Angeles, A. (2005). Serpent spirit-power stories along the seattle fault, *Seismological Research Letters* **76**(4): 426–431.

Malamud, B., Turcotte, D., Guzzetti, F. and Reichenbach, P. (2004). Landslide inventories and their statistical properties, *Earth Surface Processes and Landforms* **29**(6): 687–711.

Massey, C., Townsend, D., Rathje, E., Allstadt, K. E., Lukovic, B., Kaneko, Y., Bradley, B., Wartman, J., Jibson, R. W., Petley, D. et al. (2018). Landslides triggered by the 14 november 2016 m w 7.8 kaikōura earthquake, new zealand, *Bulletin of the Seismological Society of America* **108**(3B): 1630–1648.

Meunier, P., Hovius, N. and Haines, J. A. (2008). Topographic site effects and the location of earthquake induced landslides, *Earth and Planetary Science Letters* **275**(3-4): 221–232.

Newmark, N. M. (1965). Effects of earthquakes on dams and embankments, *Geotechnique* **15**(2): 139–160.

Perkins, J. P., Reid, M. E. and Schmidt, K. M. (2017). Control of landslide volume and hazard by glacial stratigraphic architecture, northwest washington state, usa, *Geology* **45**(12): 1139–1142.

Petersen, M. D., Shumway, A. M., Powers, P. M., Mueller, C. S., Moschetti, M. P., Frankel, A. D., Rezaeian, S., McNamara, D. E., Luco, N., Boyd, O. S. et al. (2020). The 2018 update of the us national seismic hazard model: Overview of model and implications, *Earthquake Spectra* **36**(1): 5–41.

Pollock, W., Grant, A., Wartman, J. and Abou-Jaoude, G. (2019a). Multimodal method for landslide risk analysis, *MethodsX* **6**: 827–836.

Pollock, W., Grant, A., Wartman, J. and Abou-Jaoude, G. (2019b). Multimodal method for landslide risk analysis, *MethodsX* **6**: 827–836.

Pollock, W. and Wartman, J. (2020). A framework for regional scale quantitative landslide risk analysis.

Savage, W. Z., Morrissey, M. M. and Baum, R. L. (2000). Geotechnical properties for landslide-prone seattle; area glacial deposits, *Technical report*, US Department of the Interior, US Geological Survey,.

Schulz, W. H. (2007). Landslide susceptibility revealed by lidar imagery and historical records, seattle, washington, *Engineering Geology* **89**(1-2): 67–87.

Stone, I., Wirth, E. A. and Frankel, A. D. (2022a). Topographic response to simulated m w 6.5–7.0 earthquakes on the seattle fault, *Bulletin of the Seismological Society of America* **112**(3): 1436–1462.

Stone, I., Wirth, E. and Frankel, A. (2022b). Topographic response to simulated m w 6.5–7.0 earthquakes on the seattle fault, *Bulletin of the Seismological Society of America* **112**(3): 1436–1462.

Strenk, P. M. and Wartman, J. (2011). Uncertainty in seismic slope deformation model predictions, *Engineering Geology* **122**(1-2): 61–72.

Survey, W. G. (2020). Landslide protocol inventory mapping–gis data, february, 2020: Washington geological survey digital data series 19, version 2.0, previously released january, 2019., *Technical report*.

Troost, K. G. and Booth, D. B. (2008). Geology of seattle and the seattle area, washington.

Tubbs, D. W. (1974). Landslides in seattle, *Technical report*, Department of Natural Resources.

3.6 Appendix

3.6.1 Multimodal Methods

Landscape response was determined using a modified version of the multimodal landslide model developed by Pollock et al. (2019) and Grant and Wartman (2017). This is a physical landslide model that considers two styles of landslide failure, translational and rotational slides. These failure styles are also two of the dominant failure styles in the study area (Laprade and Tubbs; 2008).

For processing efficiency, landslide probability is only calculated for areas prone to landsliding. For translational slides these are slopes steeper than 15°, while rotational landslides were modelled on slopes between 10° and 35°.

This model estimates factor of safety of slopes in the study area. This calculation is different for each style of failure. For the transitional landslides, a traditional infinite slope model is used, with factor of safety given by:

$$FS = \frac{(c + c_r) + (\gamma z * cos^2\beta - h * \gamma_w) * tan\phi}{\gamma z cos\beta * sin\beta} \tag{3.1}$$

where c is the cohesion, c_r is the root cohesion, γ is the unit weight of the soil, z is the depth to the failure plane, β is the slope angle, h is the height of the saturated soil, γ_w is the unit weight of water, and ϕ is the friction angle of the soil. For the rotational failures, the model developed by Pollock and Wartman (2020) is used to calculate the factor of safety. The functional form of this model is:

$$FS = \frac{(2\pi Rbc) + (Wcos\alpha - F_w) * tan\phi}{Wsin\alpha} \tag{3.2}$$

where c is the soil cohesion and ϕ is the soil friction angle. The basal angle α is:

$$\alpha = sin^{-1}\frac{4sin^3\delta sin\theta}{6\delta - 3sin2\delta} \tag{3.3}$$

the weight of the sliding block W is:

$$W = \pi\gamma b^2(R - b/3) \tag{3.4}$$

and the force of pore water pressure F_w is:

$$F_w = \pi \gamma_w q^2 (R - q/3) \tag{3.5}$$

where $b = R(1 - cos\delta)$ and $q = R(1 - cos\theta)$. The radius of failure R is given as:

$$R = \frac{H}{4}(\frac{cos\beta}{psin^2\beta} + \frac{p}{cos\beta}) \tag{3.6}$$

where H is local hillslope relief and p is the depth of failure as a percentage of relief. The internal angle δ is:

$$\delta = sin^{-1}\frac{H}{2Rsin\beta} \tag{3.7}$$

and the internal angle to the water table θ is:

$$\theta = cos^{-1}(1 - (1 - \frac{2z_w cos^2 R}{Hp}) * (1 + cos\delta)) \tag{3.8}$$

where z_w is the depth of the water table. Factor of safety is based on a 0.9m 2016 King County LIDAR based digital elevation model, down-scaled to 10m resolution. Troost and Booth (2008) was used as a map of geologic units in the area.

These factors of safety were then used to calculate a critical acceleration k_y as in Chien and Tsai (2017) as:

$$k_y = \frac{FS - 1}{tan^{-1}\phi + tan\alpha} \tag{3.9}$$

where FS is the factor of safety, ϕ is the material internal friction angle and α is the angle of the failure plane. This critical acceleration was then used to calculate a Newmark displacement (Newmark; 1965; Wilson and Keefer; 1983; Jibson; 1993). For each considered cell, a critical acceleration was compared to the nearest synthetic seismogram from the earthquake scenarios described in the main text. Accelerations higher than the critical acceleration were integrated to get a velocity-time history, this velocity-time history was then integrated again to get a displacement. These displacements do not represent an actual expected displacement, but can be used as a predictor for failure. As in Grant and

Wartman (2017) we set these limits to a displacement of 5cm for translational slides and 15cm for rotational slides.

Bibliography

Chien, Y.-C. and Tsai, C.-C. (2017). Immediate estimation of yield acceleration for shallow and deep failures in slope-stability analyses, *International Journal of Geomechanics* **17**(7): 04017009.

Grant, A. and Wartman, J. (2017). Regional-scale coseismic landslide hazard modeling and consequence analysis.

Jibson, R. W. (1993). Predicting earthquake-induced landslide displacements using newmark's sliding block analysis, *Transportation research record* **1411**: 9–17.

Laprade, W. T. and Tubbs, D. W. (2008). Landslide mapping in seattle, washington.

Newmark, N. M. (1965). Effects of earthquakes on dams and embankments, *Geotechnique* **15**(2): 139–160.

Pollock, W., Grant, A., Wartman, J. and Abou-Jaoude, G. (2019). Multimodal method for landslide risk analysis, *MethodsX* **6**: 827–836.

Pollock, W. and Wartman, J. (2020). A framework for regional scale quantitative landslide risk analysis.

Troost, K. G. and Booth, D. B. (2008). Geology of seattle and the seattle area, washington.

Wilson, R. C. and Keefer, D. K. (1983). Dynamic analysis of a slope failure from the 6 august 1979 coyote lake, california, earthquake, *Bulletin of the Seismological Society of America* **73**(3): 863–877.

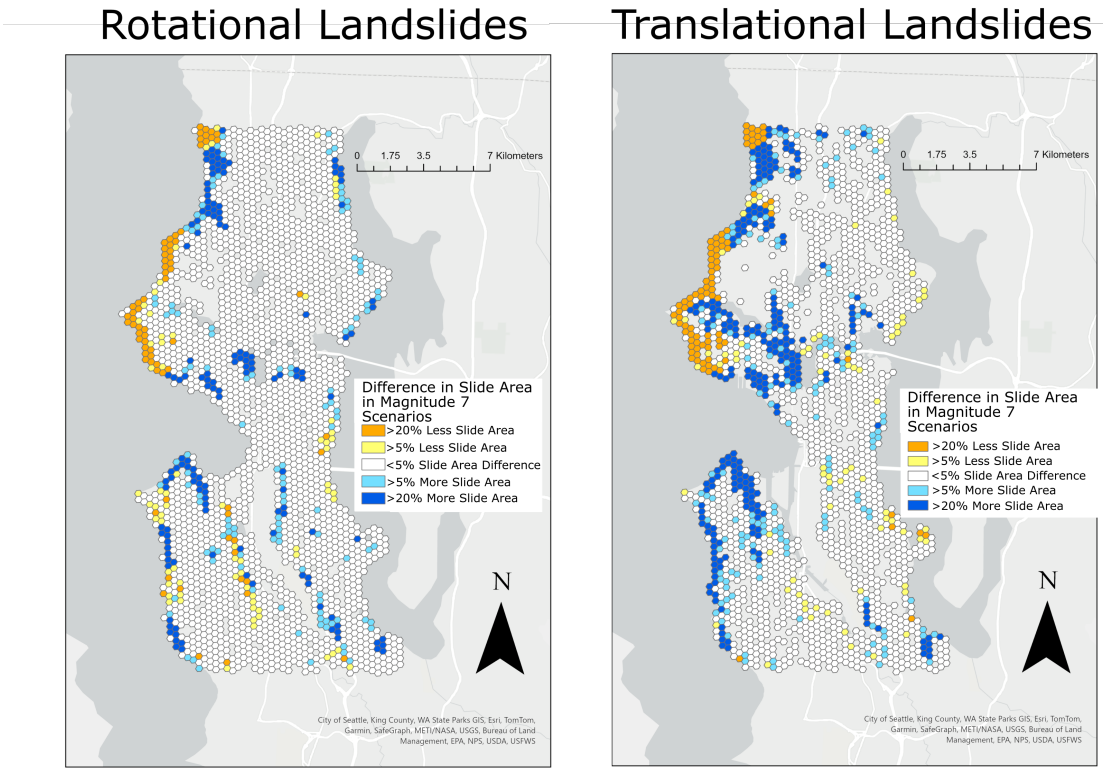

Figure 3.4: Map of spatial difference in rotational (left) and translational (right) landslides between wet and dry conditions, orange and yellow indicate more landslides in M 6.5 scenarios and blue and light blue indicate more landslides M 7 scenarios.

Chapter 4

INVESTIGATING LANDSLIDE ROUGHNESS

The roughness of a landslide can be used as a proxy for its age, assuming that the landslide has a typical initial roughness and this roughness smooths regularly over time (Booth et al.; 2009; LaHusen et al.; 2016; Booth et al.; 2017; LaHusen et al.; 2020). We test these assumptions respectively by measuring the initial roughness of thousands of landslides of the same age and by measuring the change in roughness over time of a single large landslide deposit. The initial landslide roughness data is based on landslides induced by the 2016 Kaikoura, New Zealand earthquake and the 1994 Northridge, USA earthquake. These landslides have a variability in log roughness of 0.83 m^{-1} and 0.75 m^{-1} respectfully. By filtering these landslides by size and geologic unit we can reduce that variability to 0.56 m^{-1} and 0.46 m^{-1}. Using the roughness age relationship of LaHusen et al. (2020), this would result in an error on the age estimates of 500 and 200 years. We also consider the 2014 Oso Landslide to measure how landslide deposits smooth over time. We find that the rate of smoothing is also different in broad categories of geologic units, such as glacio-fluvial deposits, but similar when subgroupings of more specific units (i.e., glacial outwash sand) are considered. Together this work demonstrates that the roughness of landslide deposits can be used as a proxy for deep seated landslide age globally, but needs to be calibrated for different geologic units in each setting.

4.1 Introduction

Modern high resolution lidar has permitted data high-resolution mapping and analysis of landslides. For example, landslide deposit roughness from lidar can be used to estimate landslide age (Booth et al.; 2009; LaHusen et al.; 2016; Booth et al.; 2017; LaHusen et al.; 2020). This is based on two assumptions: landslides are roughest when they occur and that they smooth or diffuse over time exponentially in a quantifiable way. When both

assumptions hold, landslide deposit roughness can be used as a proxy for landslide age and can yield quantitative estimates of timing (though with large uncertainty). Thus far, the roughness-dating approach has been used to successfully date large landslide inventories with hundreds to thousands of landslides in the Pacific Northwest (LaHusen et al.; 2016; Booth et al.; 2017; LaHusen et al.; 2020; Herzig et al.; 2023). However, there are assumptions in this technique that lead to high uncertainties in the calculated ages. In this study we test these assumptions to assess the error in using roughness as a proxy for landslide age.

First, we test the assumption that directly after failure, the roughness of all landslides is the same. We do this by examining thousands of landslides with the same known age and compare their roughness. We consider two earthquake induced landslide inventories, for the 2016 Kaikoura earthquake (Tanyaş et al.; 2022) and the 1994 Northridge Earthquake (Harp and Jibson; 1996).

Next, we test that landslides smooth out over time in a predictable manner. This was done by monitoring a single landslide of known initial roughness with repeat lidar surveys. These repeat surveys provide multiple measurements of the landslide roughness over time. We consider the 2014 Oso Landslide (Wartman et al.; 2016) as a case study to measure this smoothing.

4.2 Study Areas

4.2.1 Kaikoura, New Zealand

The geology of the Kaikoura area is relatively uniform as the region is underlain primarily by the Torlesse greywacke (Figure 4.1 A, Heron (2020)). The faults of the area are driven by strike-slip motion along the Alpine Fault between the Pacific and the Australian Plate.

The 2016 Kaikoura, New Zealand earthquake occurred on November 14 2016, and was the most complex earthquake rupture on record (Cesca et al.; 2017; Hamling et al.; 2017). The earthquake registered as a magnitude 7.8 earthquake with a hypo-central depth of 15km and it induced over 29,000 landslides (Massey et al.; 2020). The size distribution of these landslides is not significantly different from other earthquake induced inventories (Tanyaş et al.; 2022). Airborne lidar was collected months after the earthquake, which allows us to

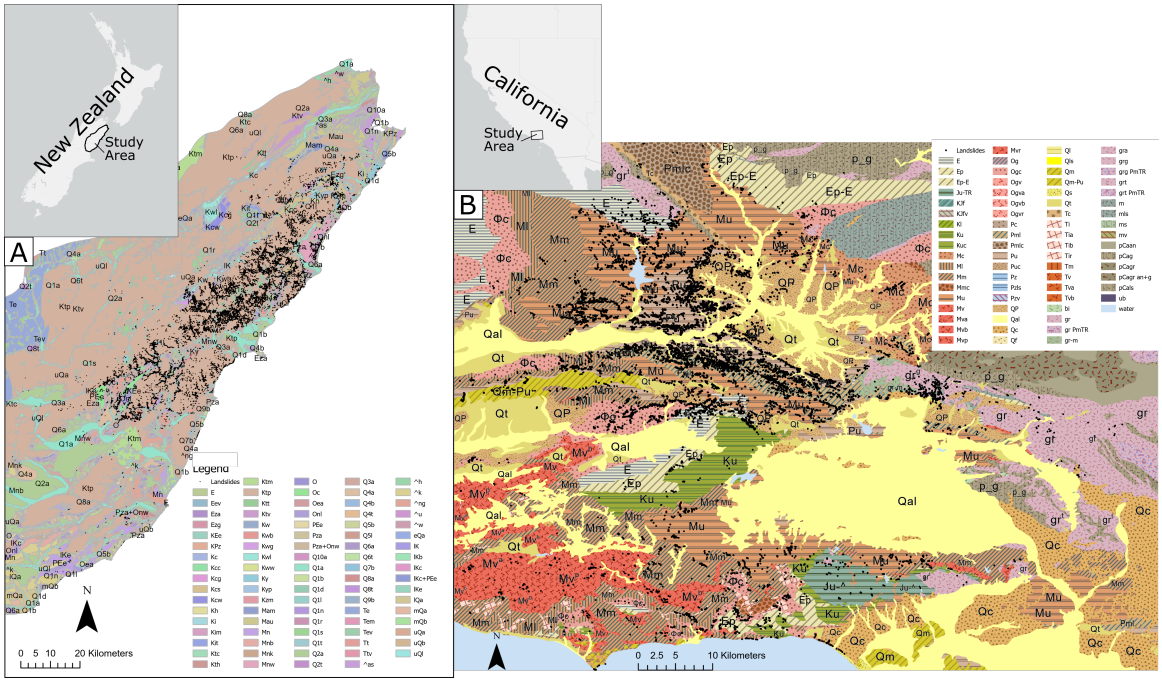

Figure 4.1: Maps of landslides and geologic units in Kaikoura, NZ (A) (Heron; 2020; Tanyaş et al.; 2022) and Northridge, CA, USA (B) (Jennings and Strand; 1969; Harp and Jibson; 1996). Landslides are points, geologic units are colored areas. Inset maps show location of corresponding study area.

essentially measure the initial induced landslide roughness of these landslides.

4.2.2 Northridge, CA, USA

The geology of the Northridge area is composed of marine sedimentary rocks and both intrusive and extrusive igneous rock, as well as their metamorphosed counterparts (Figure 4.1 B, Jennings and Strand (1969)). Faulting in the area is driven by strike-slip motion on the San Andreas Fault, which separates the Pacific and North American Plates.

The magnitude 6.7, Northridge, California USA earthquake occurred on January 17, 1994. The rupture had a hypocenter that was 18km deep (Wald et al.; 1996) and the earthquake triggered over 11,000 landslides (Harp and Jibson; 1996). High quality lidar of this area was collected in 2015, giving a record of the roughness of these induced landslides 11 years after failure. This is enough time for the landslides to start smoothing out, and means that these are not true initial roughness measurements. However, they still represent a set of landslides of the same age and how much variability is present in those landslides.

4.2.3 Oso, WA, USA

The 2014 Oso, Washington, USA landslide was one of the most deadly landslides in US history, killing 43 people and destroying an entire community (Iverson et al.; 2015; Wartman et al.; 2016). The slide was a deep seated complex failure, which failed in multiple parts (Wartman et al.; 2016). After the landslide, the area has been extensively monitored and studied (Iverson et al.; 2015; Wartman et al.; 2016; Anderson et al.; 2017; Collins and Reid; 2020). These repeat studies and new lidar collected for this work, allow for measuring how the landslide has changed over time.

The Oso landslide was a failure on the side of a glacial terrace known as the Whitman Bench. This terrace is composed of mostly horizontal layers of glacial stratigraphy, which are identified from top to bottom as recessional outwash (Q_{goe}), till (Q_{gtv}), advance outwash (Q_{gov}), and advance glaciolacustrine deposits (Q_{glv}) (Tabor et al.; 2002; Dragovich et al.; 2003; Badger; 2015). In addition to the glacial stratigraphy, Collins and Reid (2020) also mapped and differentiated parts of the landslide as: landslide headscarp (Q_c), undifferen-

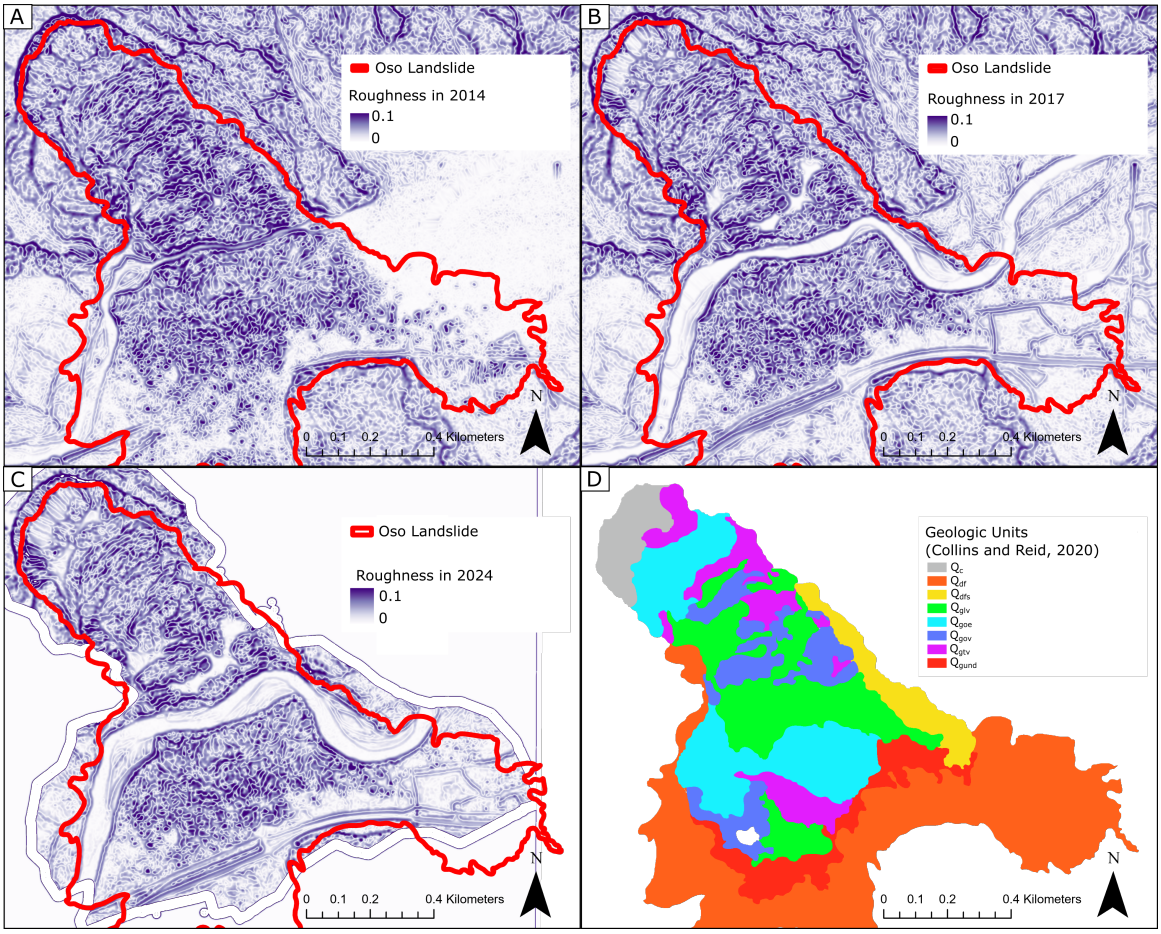

Figure 4.2: Maps of the roughness of the Oso Landslide over time (A-C) and of mapped geologic units of the landslide (D). Maps of 20m roughness, with higher roughness represented with purple, for roughness of the Oso landslide in 2014 (A), 2017 (B), and 2024 (C). The extent of the landslide is outlined in red. Geologic map (D) is adapted from Collins and Reid (2020). Mapped units are recessional outwash (Q_{goe}), till (Q_{gtv}), advance outwash (Q_{gov}), advance glaciolacustrine deposits (Q_{glv}), landslide headscarp (Q_c), undifferentiated sediments (Q_{gund}), primary (Q_{df}) and secondary (Q_{dfs}) debris-flow deposits.

tiated sediments (Q_{gund}), primary (Q_{df}) and secondary (Q_{dfs}) debris-flow deposits (Figure 4.2).

4.3 Methods

4.3.1 Initial Roughness Measurements

As in LaHusen et al. (2020), we measured landslide roughness using a 20 m Ricker wavelet (Ricker; 1943) transform, alternatively known as a "Mexican hat" wavelet, on the lidar elevation data of landslide deposits. This wavelet was scaled so that it measures topographic curvature as a function of length scale (Kumar and Foufoula-Georgiou; 1997; Lashermes et al.; 2007; Booth et al.; 2017). We excluded areas of the deposit within 15 m of gullies which do not follow a diffusive hillslope transport law. Gullies were identified as areas with a concave-up profile curvature of $\geq 0.09 m^{-1}$ and with a drainage area of $\geq$2,670m^2 calculated using a D-infinity flow accumulation algorithm as done in Booth et al. (2017). Lidar was not available for all landslides in both inventories. By restricting to landslides completely covered by lidar, we analyse 5,066 and 1,455 landslides in Kaikoura and Northridge respectfully.

We generalize the roughness of the landslides by measuring the mean and standard deviation of the log of roughness. This is because the landslide roughness measurements tend to form a log normal distribution (Figure 4.3). We call these log mean values the mean initial roughness. These values were further refined by filtering by geology. Geologic units on a 1:250,000 scale were used for both Kaikoura (Heron; 2020) and Northridge (Jennings and Strand; 1969) (Figure 4.1). Additionally we repeat this analysis considering only large (Area $\geq$ 10,000 m^2) landslides and measure new log normal distributions for both the overall distributions and the geology specific distributions.

4.3.2 Roughness over Time

Roughness of the Oso Landslide was also measured using a Ricker wavelet (Ricker; 1943), though for this area we used a 15m wavelet as this was found to be most informative for weak glacial sediments of the North Fork Stillaguamish River area (Booth et al.; 2017).

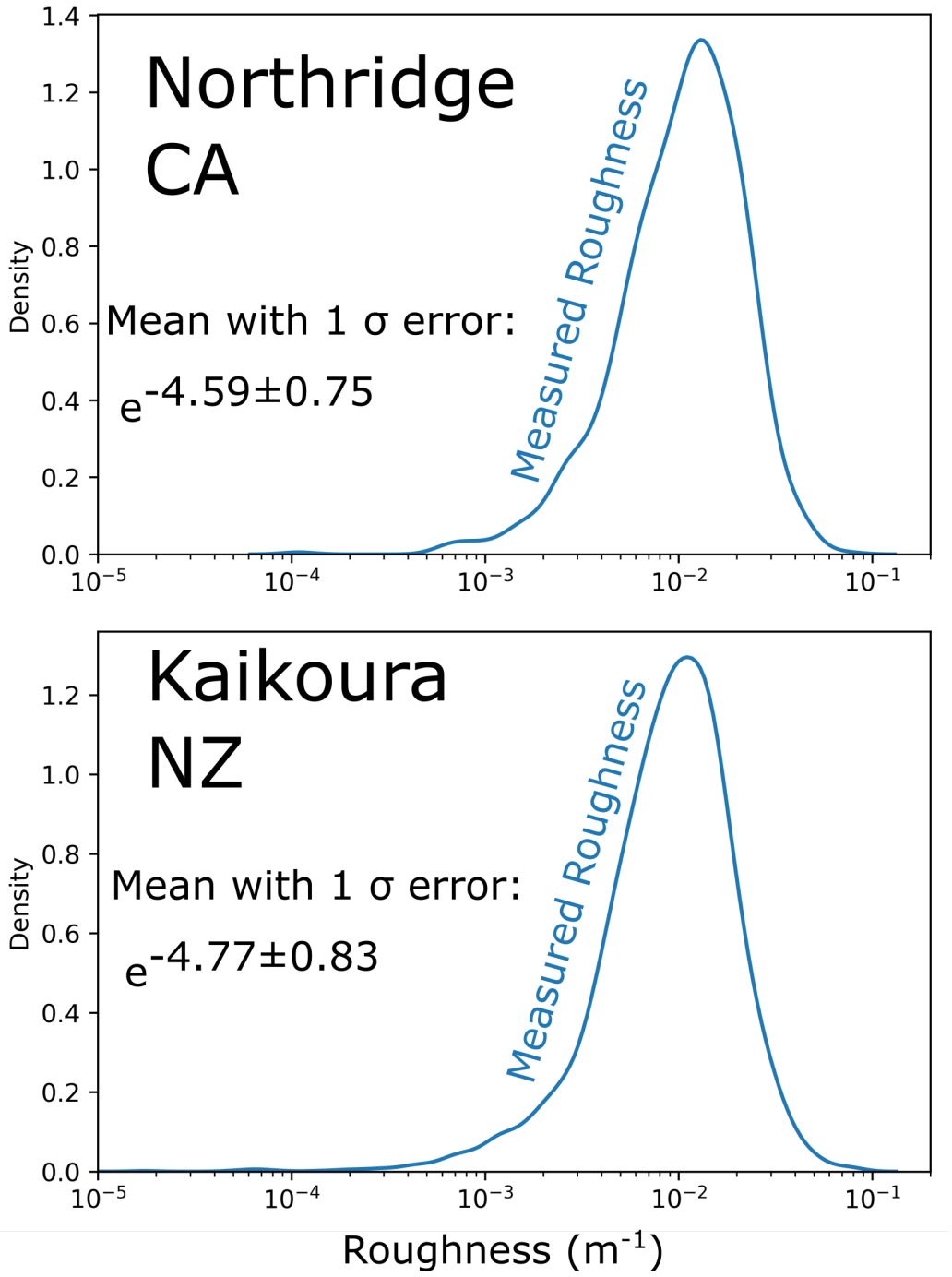

Figure 4.3: Kernel density estimate plots of landslide roughness for both Northridge (top) and Kaikoura (bottom). The x-axis is roughness (m^{-1}) on a log scale.

The different geologic units present in the Oso landslide might smooth out at different rates. To test this, we split the Oso landslide into zones of similar geologic units as mapped by Collins and Reid (2020) and measure the change in roughness separately for each zone.

We measure the roughness from three lidar surveys, one in 2014 that was conducted soon after the landslide, a 2017 lidar dataset and finally a new dataset that we collected via UAV in 2024. These data were all collected at 1m resolution or better. Higher resolution data was down-sampled to 1m to properly compare between the studies. Roughness was only calculated for areas covered by all three lidar surveys.

Figure 4.2 shows the lidar used for the roughness analysis and geologic units in the Oso landslide mapped by Collins and Reid (2020). The roughness was calculated for each of these individual geologic units.

4.4 Results

4.4.1 Initial Landslide Roughness

We find that the landslides in Kaikoura have a mean initial log roughness of -4.77 m^{-1} with a standard deviation of 0.83 m^{-1} (Figure 4.3). The Northridge inventory has a mean initial roughness of -4.59 m^{-1} with a standard deviation of 0.75 m^{-1} (Figure 4.3).

Geology

While most geologic units have similar roughness distributions (Tables 4.1 and 4.2, Figure 4.4), some units have different mean initial roughness. For example, in Kaikoura, Motunau Group sandstone (MN) (-6.50 ± 2.50 m^{-1}), Cookson Volcanics Group (Oc) (-5.16 ± 0.73 m^{-1}), Late Pleistocene ocean beach deposits (Q5b) (-5.30 ± 0.99 m^{-1}), and Holocene dune deposits (Q1d) (-5.22 ± 0.42 m^{-1}) have a smoother initial roughness ($< -4.77 \pm 0.83$ m^{-1}). For Northridge, units such as Sespe Formation (Ogc) (-5.32 ± 0.78 m^{-1}), Marble Lenses in Gneiss (pCals) (-5.32 ± 0.94 m^{-1}), and Fiss Fanglomerate (Mc) (-5.14 ± 0.75 m^{-1}) have a smoother initial roughness ($< -4.59 \pm 0.75$ m^{-1}). Filtering by geologic unit leads to an average variation in initial log roughness of 0.91 m^{-1} in Kaikoura and 0.72 m^{-1} in Northridge.

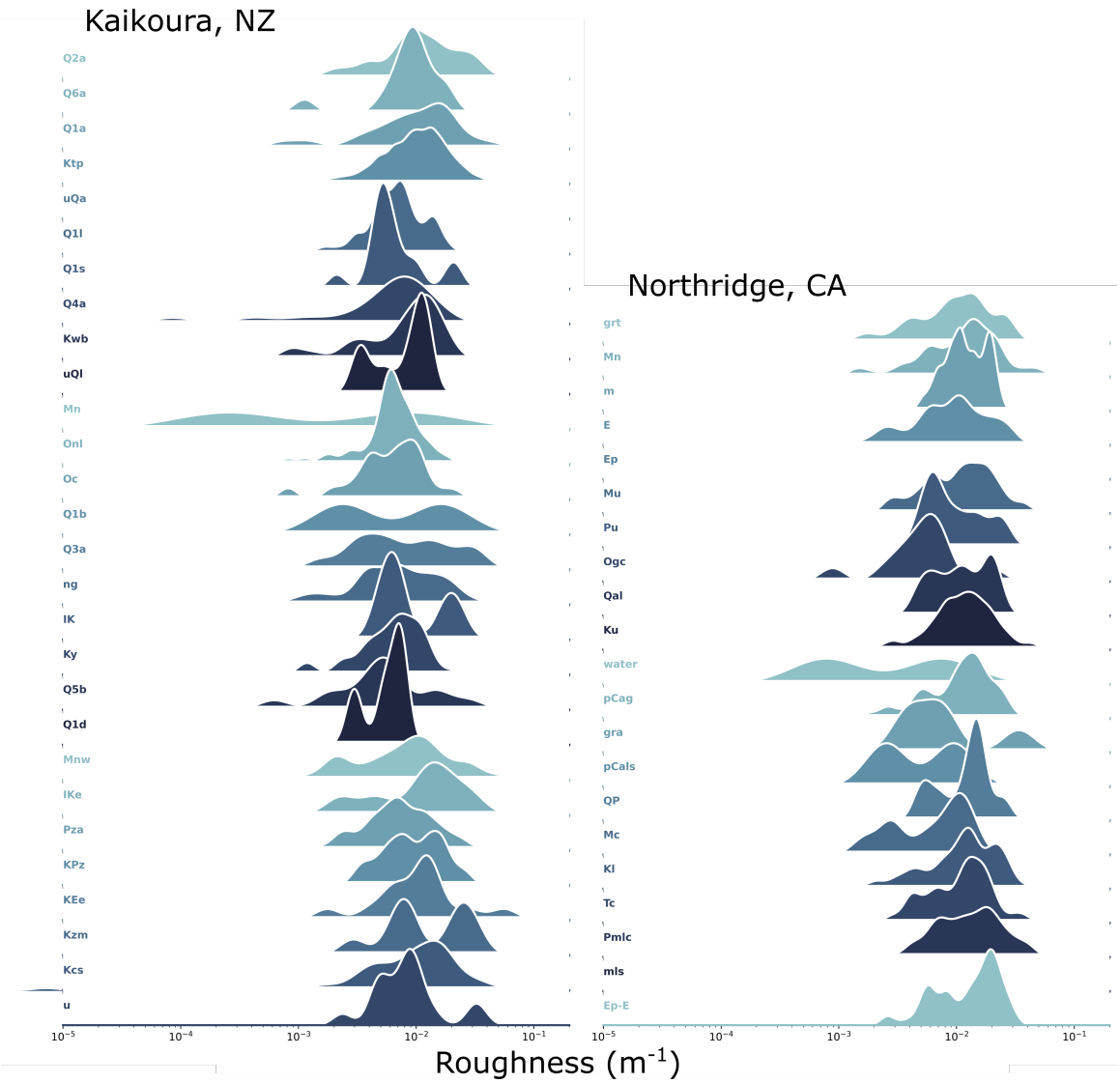

Figure 4.4: Kernel density estimate plots of landslide roughness as a function of geologic unit for both Northridge (right) and Kaikoura (left). The x-axis is roughness (m^{-1}) on a log scale.

Geologic Unit	Code	Mean Log Roughness (m^{-1})	Mean Log Roughness Area $\geq$ 10,000 m^2 (m^{-1})
Late Pleistocene river deposits	Q2a	-4.69 ± 0.94	-4.50 ± 0.35
Middle Pleistocene river deposits	Q6a	-4.80 ± 0.71	NA
Holocene river deposits	Q1a	-4.87 ± 1.16	-5.18 ± 1.28
Pahau sandstone and mudstone	Ktp	-4.70 ± 0.79	-4.62 ± 0.55
Holocene landslide deposits	Q1l	-5.07 ± 0.67	-5.03 ± 0.40
Holocene scree deposits	Q1s	-5.03 ± 0.59	-5.25 ± 0.36
Late Pleistocene river deposits	Q4a	-5.56 ± 1.46	NA
Bluff Sandstone Formation	Kwb	-4.95 ± 0.86	-5.31 ± 1.23
Quaternary landslide deposits	uQl	-4.91 ± 0.55	-5.05 ± 0.85
Motunau Group sandstone	Mn	-6.50 ± 2.50	NA
Weka Pass Limestone	Onl	-5.14 ± 0.62	-5.00 ± 0.23
Cookson Volcanics Group	Oc	-5.16 ± 0.73	-5.20 ± 0.47
Holocene ocean beach deposits	Q1b	-5.08 ± 1.37	NA
Late Pleistocene river deposits	Q3a	-4.87 ± 0.94	NA
Greta Formation	ng	-5.17 ± 1.08	-5.04 ± 0.40
Undifferentiated sandstone	IK	-4.7 ± 0.63	NA
Seymour Group sandstone	Ky	-5.14 ± 0.76	-4.93 ± 0.45
Late Pleistocene ocean beach deposits	Q5b	-5.30 ± 0.99	-5.30 ± 0.31
Holocene dune deposits	Q1d	-5.22 ± 0.42	NA
Waima Formation	Mnw	-4.88 ± 0.98	4.99 ± 0.66
Conway Formation	IKe	-4.58 ± 0.88	NA
Amuri Formation	Pza	-4.96 ± 0.84	-4.92 ± 0.61
Muzzle Group limestone	KPz	-4.70 ± 0.71	-4.65 ± 0.67
Eyre Group sandstone and conglomerate	KEe	-4.59 ± 0.85	NA
Mead Hill Formation	Kzm	-4.44 ± 0.80	-4.04 ± 0.63
Split Rock Formation	Kcs	-4.78 ± 1.16	-4.66 ± 0.53
Undifferentiated Pliocene Siltstone	u	-4.78 ± 0.66	-5.20 ± 0.14

Table 4.1: Mean Initial Landslide Roughness in Kaikoura

Geologic Unit	Code	Mean Log Roughness (m^{-1})	Mean Log Roughness Area $\geq$ 10,000 m^2 (m^{-1})
Vermont Quartz Diorite	grt	-4.63 ± 0.80	-4.62 ± 0.40
Monterey Shale	Mn	-4.54 ± 0.78	-4.32 ± 0.67
Pelona Schist	m	-4.43 ± 0.40	-4.53 ± 0.67
Coldwater Sandstone	E	-4.79 ± 0.83	-4.48 ± 0.83
Pattiway Formation	Ep	-3.91 ± 2.00	NA
Temblor Sandstone	Ml	-4.89 ± 0.01	NA
Tequepis Sandstone	Mu	-4.58 ± 0.71	-4.48 ± 0.64
Pico Formation	Pu	-4.64 ± 0.58	NA
Sespe Formation	Ogc	-5.32 ± 0.78	NA
Alluvium	Qal	-4.51 ± 0.56	NA
Jalama Formation	grt	-4.56 ± 0.77	-4.23 ± 0.32
Granite	gr	-4.66 ± 0.62	NA
Mendenhall Gneiss	pCag	-4.63 ± 0.72	-4.42 ± 0.52
Liebre Quartz Monzonite	gra	-4.84 ± 0.88	-5.25 ± 0.53
Marble Lenses in Gneiss	pCals	-5.32 ± 0.94	NA
Paso Robles Formation	QP	-4.46 ± 0.52	NA
Fiss Fanglomerate	Mc	-5.14 ± 0.75	NA
Espada Formation	Kl	-4.54 ± 0.71	-4.23 ± 0.38
Caliente Formation	Tc	-4.56 ± 0.61	-4.18 ± 0.24
Anaverde Formation	Pmlc	-4.48 ± 0.82	-4.05 ± 0.47
San Francisquito Formation	Ep-E	-4.41 ± 0.63	-4.04 ± 0.54

Table 4.2: Mean Initial Landslide Roughness in Northridge

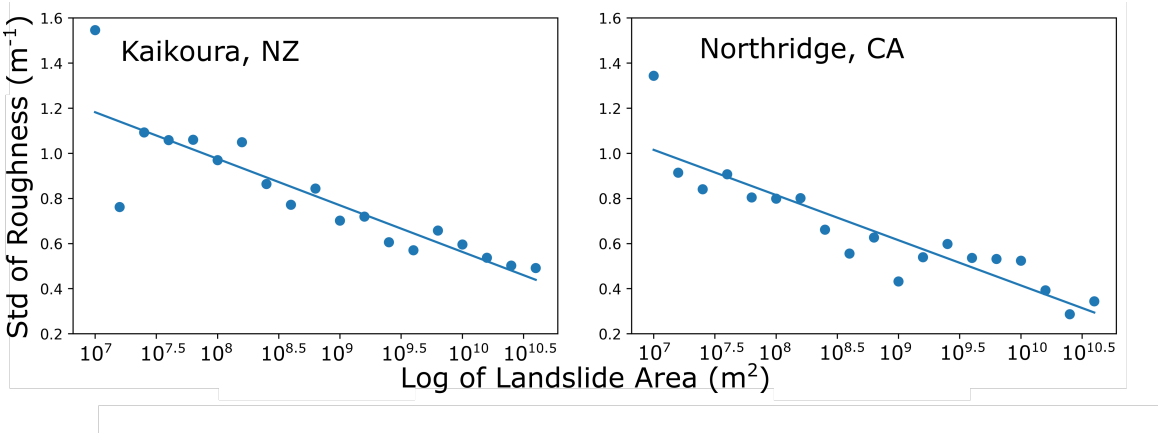

Figure 4.5: Scatter plots of variation of landslide roughness (y-axis) as a function of landslide area (log scale on the x-axis) for both Northridge (right) and Kaikoura (left).

Landslide Area

Landslide area is correlated with variation in roughness (Figure 4.5), with larger landslides reducing the variation in roughness. By limiting our analysis to landslides larger than 10,000 m^2 we can improve our log roughness in Kaikoura to $-4.69 \pm 0.58\ m^{-1}$ and in Northridge to $-4.32 \pm 0.53\ m^{-1}$. We also restrict the landslides considered in the geologic unit analysis (Figure 4.6). This similarly reduces the variation of the roughness and leads to more separation in roughness values for the geologic units with different mean initial roughness. The average variation in initial log roughness is reduced from 0.91 m^{-1} to 0.56 m^{-1} and 0.72 m^{-1} to 0.46 m^{-1} for Kaikoura and Northridge respectively.

Comparison based on geologic unit also changes some of the observed patterns in mean initial roughness. In Kaikoura, this further separates the roughnesses, with units such as Holocene scree deposits (Q1s) ($-5.25 \pm 0.36\ m^{-1}$) and Undifferentiated Pliocene Siltstone (u) ($-5.20 \pm 0.14\ m^{-1}$) having smoother than average roughness, and units such as the Mead Hill Formation (Kzm) ($-4.04 \pm 0.63\ m^{-1}$) with rougher than average initial roughness. In Northridge, we see similar patterns, for example, with the Liebre Quartz Monzonite (gra) ($-5.25 \pm 0.53\ m^{-1}$). In both Kaikoura and Northridge, other units, such as the previously smoother Northridge units: Sespe Formation (Ogc), Marble Lenses in Gneiss (pCals), and

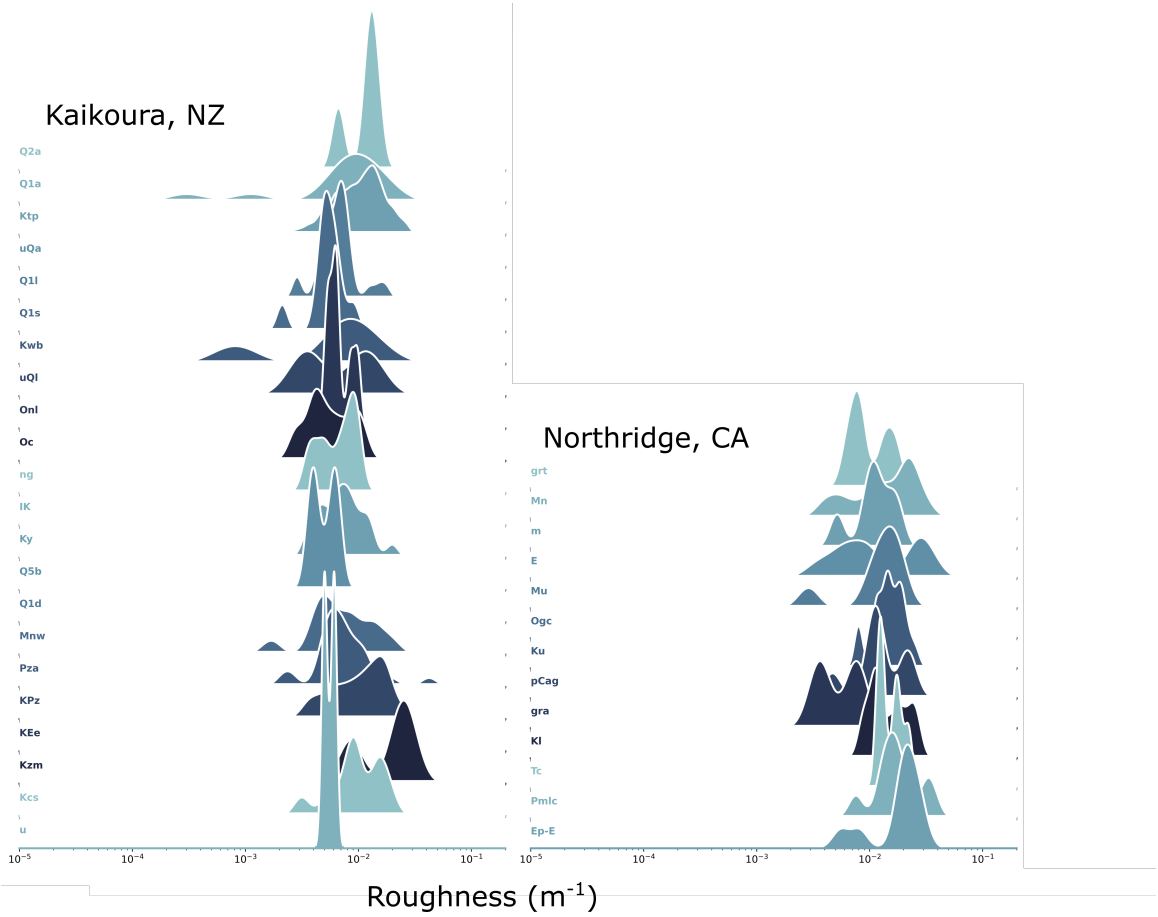

Figure 4.6: Kernel density estimate plots of landslide roughness as a function of geologic unit for both Northridge (right) and Kaikoura (left). This figure only considers landslides over 10,000m^2. The x-axis is roughness (m^{-1}) on a log scale.

Geologic Unit	Code	a	b
Landslide Headscarp	Q_c	11.88	-368.2
Debris-flow Deposit	Q_{df}	8.029	-472.2
Secondary Debris-flow Deposit	Q_{dfs}	-12.78	501.0
Till	Q_{glv}	24.65	-729.7
Recessional Outwash	Q_{goe}	137.6	-4547
Advance Outwash	Q_{gov}	30.42	-880.4
Advance Glaciolacustrine Deposit	Q_{gtv}	26.83	-782.7
Undifferentiated Deposit	Q_{gund}	24.11	-680.7

Table 4.3: Oso Age-Roughness fitting parameters

Fiss Fanglomerate (Mc), now do not have enough data to measure the variation in roughness data (NA).

4.4.2 Roughness over Time

Roughness a decade after the landslide for the different geologic units in the Oso Landslide are plotted in Figure 4.7 along with the best fit regression between roughness and log age. Table 4.3 shows the coefficients for the best fit regression for exponential function $age = a * e^{b*R}$, where R is the measured roughness. These show that some geologic units smooth differently, while others smooth similarly. For example the till (Q_{glv}), advance outwash (Q_{gov}), and advance glaciolacustrine deposits (Q_{glv}) all smooth at similar rates and have similar initial roughnesses. The recessional outwash (Q_{goe}) on the other hand, smooths much slower and has a smoother initial roughness. The debris-flow deposits (Q_{df}) and undifferentiated deposits (Q_{gund}) of the 2014 landslide also have slower diffusion rates. The secondary debris-flow deposits (Q_{dfs}) even have a negative diffusion rate, indicating roughening over time. Finally, the landslide (Q_c) headscarp has a much faster rate of diffusion than every other unit.

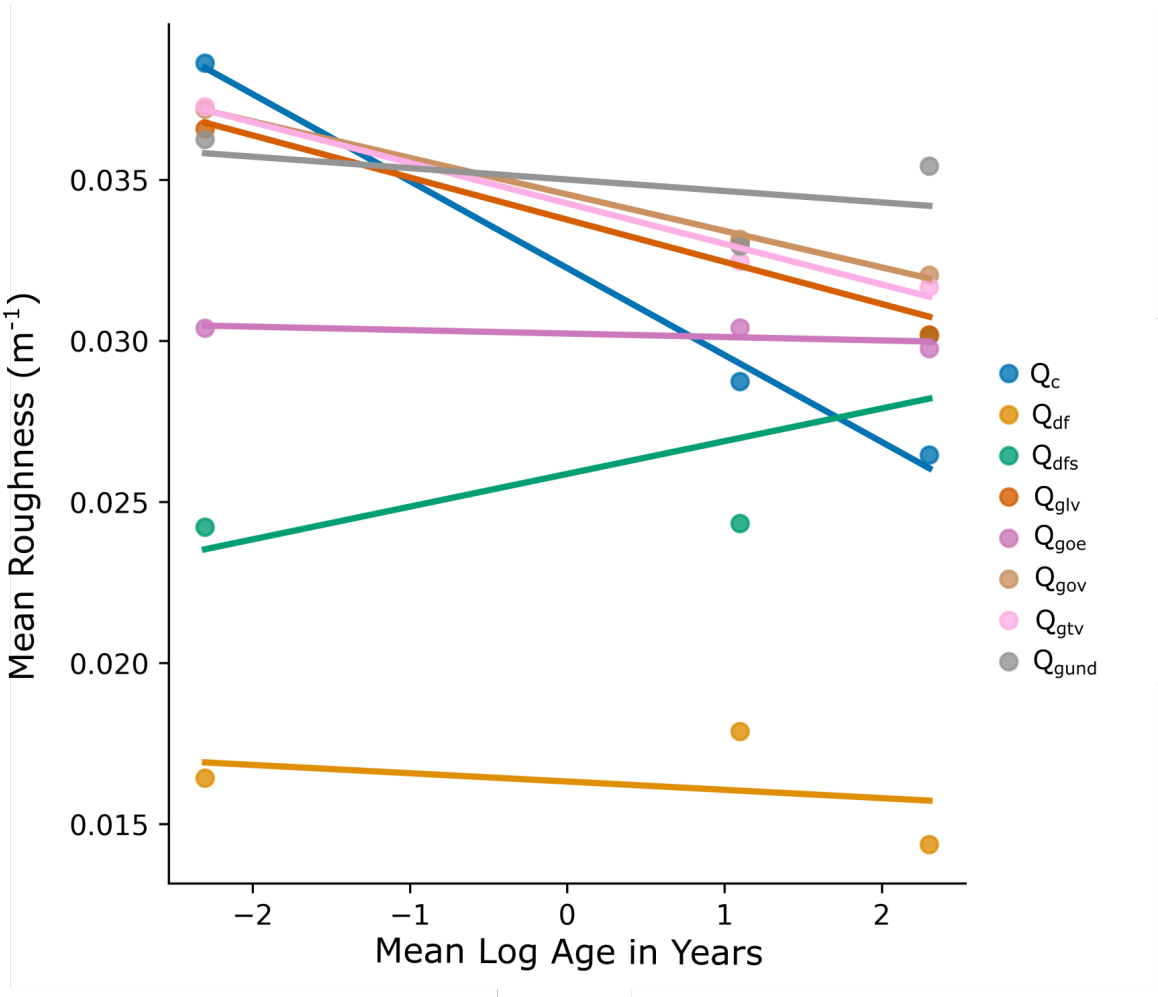

Figure 4.7: Plot of roughness vs log age for different geologic units in the Oso Landslide. Lines show best fit regression for each geologic unit (Table 4.3). Geologic units are landslide headscarp (Q_c), debris-flow deposits (Q_{df}), recessional outwash (Q_{goe}), till (Q_{gtv}), advance outwash (Q_{gov}), and advance glaciolacustrine deposits (Q_{glv}) as mapped in Collins and Reid (2020).

4.5 Discussion

Initial landslide roughness likely varies with factors such as climate and rock type. The initial mean roughness values for Northridge landslide deposits is similar to initial work in the Pacific Northwest(LaHusen et al.; 2016; Booth et al.; 2017), while Kaikoura has a smoother mean initial roughness. Within each study area, some geologic units have different initial roughness. This is also supported by the different initial roughness measurements for the different geologic units in the Oso Landslide. This is likely due to how different geologic strengths can lead to differences in failure process and deposit features like block size.

Specifically, we find that strong units such as the chert of the Mead Hill formation (Kzm) tends to form smoother landslide deposits. While weaker units, such as ocean beach (Q5b) and dune deposits (Q1d) in Kaikoura and the heavily fractured Liebre Quartz Monzonite (gra) in Northridge, tend to form rougher deposits. These differences likely relate to differing failure styles, with stronger rocks failing in rockfall style failures with less hummocks of the measured size (20m) and weaker rocks and Quaternary deposits failing in flow-slide style failures with more hummocks with the same size as the wavelet used (20m).

Correlation between variability in roughness and lithology suggests that for future landslide-age based dating studies, a new roughness-age relationship needs to be calibrated for each newly considered region and geologic unit. While it is outside the scope of this study to re-calibrate the age roughness relationship for Northridge and Kaikoura, we can use the relationship developed for the Oregon Coast Range, $age = 1.428 * 10^6 * e^{-412.8*R}$ (LaHusen et al.; 2020), to estimate the error (in years) this variation would cause in an age estimate. For the 0.56 m^{-1} variation in log roughness measured in the Kaikoura landslides, this results in a 500 year variation in estimated age of a 1 year old landslide. For the 0.46 m^{-1} variation measured from the Northridge landslides, this results in a 200 year variation in estimated age. This error is within the expected error for the roughness-age analysis used in Chapter 2.

The landslide inventories we consider do not distinguish between shallow landslides and deep-seated landslides. The roughness-age relationship was developed for deep seated landslides (Booth et al.; 2009, 2017; LaHusen et al.; 2020), as shallow landslides tend to not

create a lasting disturbance in lidar measurements of the ground surface. By selecting for large landslides, we may have inadvertently selected for deeper seated slides as they types tend to be larger than shallow failures. This may explain why the variation in roughness is reduced by selecting for larger landslides. Whether this is the cause or not, this pattern suggests that for work using the landslide-age roughness method as a proxy for landslide age, only landslides over 10,000 m^2 should be considered to reduce error in dating.

The rate at which a deposit smooths over time is also dependent on geologic unit. For example, Figure 4.7 shows that for the Oso landslide the recessional outwash (Q_{goe}) smooths out slower than the till (Q_{glv}), advance outwash (Q_{gov}), and advance glaciolacustrine deposits (Q_{glv}), all of which smooth at a similar rate. This shows that for diffusion rates broad geologic type is important, the deposits from glacial recession are different than all the deposits from glacial advance. But, within a similar geologic type, such as within the different glacial advance deposits, it appears that diffusion rate is effectively the same.

The other considered units are all not true geologic units, but instead different failure styles. Since the roughness dating method is designed for the deposits of deep-seated rotational landslides, we show here that it does not function for different failure styles. The debris flow deposits all have low or even negative diffusion rates, indicating that diffusion is not operating in the same manner as on the rotational landslide deposits. The undifferentiated deposits can also be included in this analysis, as they are mostly composed of flow-slide or debris-flow like features. The landslide head-scarp on the other hand has a much faster diffusion rate, again suggesting a different diffusion regime than the rest of the landslide, and supported the decision to exclude head scarps from landslide roughness age estimates. This corroborates our previous hypothesis that variance in the landslide roughness in Northridge and Kaikoura is partially driven by a lack of records of landslide style, and of landslide polygons that include landslide head scarps.

4.6 Conclusions

Landslide age can be estimated from roughness, assuming that landslides have a common initial roughness and smooth out over time at similar rates. To test these assumptions, we investigated 5,066 landslides induced by the Kaikoura earthquake in 2016 in New Zealand

(Tanyaş et al.; 2022), and 1,455 landslides induced by the 1994 Northridge earthquake (Harp and Jibson; 1996). We find that initial landslide deposit roughness for these two cases is highly variable, with almost an order of magnitude of variation (standard deviation of log roughness of 0.83 m^{-1} for Kaikoura, and 0.75 m^{-1} for Northridge). This roughness is controlled by geologic unit and landslide size. By restricting to landslides over 10,000 m^2 in area and filtering by geologic unit, we can reduce the measured variability in initial roughness. This results in average variations in initial log roughness of 0.56 and 0.46 for Kaikoura and Northridge that equates to an error of 500 and 200 years, for Kaikoura and Northridge respectively, based on the roughness analysis of LaHusen et al. (2020).

We also investigated how the roughness changed over time with repeat lidar surveys of the 2014 Oso Landslide. We found that geologic units again play an important role, with deposits from glacial advance outwash smoothing faster than deposits of glacial retreat outwash. Our findings emphasize the necessity for calibrating an age-roughness relationship to estimate the ages of landslides for sites with different geologic materials, landslides in different materials should be calibrated and dated separately. Though it also shows that detailed geologic mapping is not necessary for this work, general geologic categories initially appear to be sufficient for distinguishing between different diffusion rates.

Bibliography

Anderson, S. W., Keith, M. K., Magirl, C. S., Wallick, J. R., Mastin, M. C. and Foreman, J. R. (2017). Geomorphic response of the north fork stillaguamish river to the state route 530 landslide near oso, washington, *Technical report*, US Geological Survey.

Badger, T. C. (2015). Sr 530 mp 35 to 41 geotechnical study, *Washington State Department of Transportation, Olympia, Washington* .

Booth, A., LaHusen, S., Duvall, A. and Montgomery, D. (2017). Holocene history of deep-seated landsliding in the north fork stillaguamish river valley from surface roughness analysis, radiocarbon dating, and numerical landscape evolution modeling, *Journal of Geophysical Research: Earth Surface* **122**(2): 456–472.

Booth, A., Roering, J. and Perron, T. (2009). Automated landslide mapping using spectral

analysis and high-resolution topographic data: Puget sound lowlands, washington, and portland hills, oregon, *Geomorphology* **109**(3-4): 132–147.

Cesca, S., Zhang, Y., Mouslopoulou, V., Wang, R., Saul, J., Savage, M., Heimann, S., Kufner, S.-K., Oncken, O. and Dahm, T. (2017). Complex rupture process of the mw 7.8, 2016, kaikoura earthquake, new zealand, and its aftershock sequence, *Earth and Planetary Science Letters* **478**: 110–120.

Collins, B. D. and Reid, M. E. (2020). Enhanced landslide mobility by basal liquefaction: The 2014 state route 530 (oso), washington, landslide, *GSA Bulletin* **132**(3-4): 451–476.

Dragovich, J., Stanton, B., Lingley, W., Griesel, G. and Polenz, M. (2003). *Geologic Map of the Mount Higgins 7.5 Minute Quadrangle, Skagit and Snohomish Counties, Washington: Washington State Division of Geology and Earth Research Open-File Report 2003-12, scale 1:24,000.*

Hamling, I. J., Hreinsdóttir, S., Clark, K., Elliott, J., Liang, C., Fielding, E., Litchfield, N., Villamor, P., Wallace, L., Wright, T. J. et al. (2017). Complex multifault rupture during the 2016 m w 7.8 kaikōura earthquake, new zealand, *Science* **356**(6334): eaam7194.

Harp, E. L. and Jibson, R. W. (1996). Landslides triggered by the 1994 northridge, california, earthquake, *Bulletin of the Seismological society of America* **86**(1B): S319–S332.

Heron, D. (2020). Geological map of new zealand 1: 250,000. gns science geological map 1, *GIS data* .

Herzig, E., Duvall, A., Booth, A., Stone, I., Wirth, E., LaHusen, S., Wartman, J. and Grant, A. (2023). Evidence of seattle fault earthquakes from patterns in deep-seated landslides.

Iverson, R. M., George, D. L., Allstadt, K., Reid, M. E., Collins, B. D., Vallance, J. W., Schilling, S. P., Godt, J. W., Cannon, C., Magirl, C. S. et al. (2015). Landslide mobility and hazards: implications of the 2014 oso disaster, *Earth and Planetary Science Letters* **412**: 197–208.

Jennings, C. and Strand, R. (1969). Geologic map of california : Los angeles sheet, *Technical Report Geologic Atlas of California GAM-08*, California Division of Mines and Geology.

Kumar, P. and Foufoula-Georgiou, E. (1997). Wavelet analysis for geophysical applications, *Reviews of geophysics* **35**(4): 385–412.

LaHusen, S., Duvall, A., Booth, A., Grant, A., Mishkin, B., Montgomery, D. and Wartman, J. (2020). Rainfall triggers more deep-seated landslides than cascadia earthquakes in the oregon coast range, usa, *Science advances* **6**(38): 6790.

LaHusen, S., Duvall, A., Booth, A. and Montgomery, D. (2016). Surface roughness dating of long-runout landslides near oso, washington (usa), reveals persistent postglacial hillslope instability, *Geology* **44**(2): 111–114.

Lashermes, B., Foufoula-Georgiou, E. and Dietrich, W. (2007). Channel network extraction from high resolution topography using wavelets, *Geophysical Research Letters* **34**(23).

Massey, C., Townsend, D., Lukovic, B., Morgenstern, R., Jones, K., Rosser, B. and de Vilder, S. (2020). Landslides triggered by the mw 7.8 14 november 2016 kaikōura earthquake: an update, *Landslides* **17**: 2401–2408.

Ricker, N. (1943). Further developments in the wavelet theory of seismogram structure, *Bulletin of the Seismological Society of America* **33**(3): 197–228.

Tabor, R., Booth, D., Vance, J. and Ford, A. (2002). *Geologic map of the Sauk River 30-by 60-minute quadrangle, Washington*, number 2592.

Tanyaş, H., Görüm, T., Fadel, I., Yıldırım, C. and Lombardo, L. (2022). An open dataset for landslides triggered by the 2016 mw 7.8 kaikōura earthquake, new zealand, *Landslides* **19**(6): 1405–1420.

Wald, D. J., Heaton, T. H. and Hudnut, K. W. (1996). The slip history of the 1994 northridge, california, earthquake determined from strong-motion, teleseismic, gps, and leveling data, *Bulletin of the Seismological Society of America* **86**(1B): S49–S70.

2122 Wartman, J., Montgomery, D. R., Anderson, S. A., Keaton, J. R., Benoît, J., dela Chapelle,
2123 J. and Gilbert, R. (2016). The 22 march 2014 oso landslide, washington, usa, *Geomor-*
2124 *phology* **253**: 275–288.

Chapter 5

CONCLUSIONS

Earthquake induced landslides are an important geologic process. Like all landslides, they can shape the landscape and represent a dangerous hazard to both people and property. Because they occur in clusters near the earthquake source, they amplify the hazard posed by earthquake shaking alone, and can accelerate hillslope erosion. This clustering, however, serves as a useful property for both identifying past earthquake induced landslides and understanding properties of landslides themselves. In this dissertation, I use earthquake induced landslides to investigate past earthquakes and landslide roughness. I also model earthquake induced landslides in order to test what factors control where these landslides are likely to occur.

In Chapter 2, I collect a dated landslide inventory of the Puget Lowlands, WA, USA and use landslide clusters to find evidence of past earthquakes on the Seattle Fault. By finding that landslide clusters occurred at the same time as past Seattle Fault earthquakes, I show that it is possible to use landslides as a regional paleo-seismic indicator.

In Chapter 3, I model possible future earthquake induced landslides from a Seattle Fault earthquake. I find that a Seattle Fault earthquake would likely cause 10% of slopes to fail in translational landslides, and 4% of slopes to fail in rotational landslides. This distribution is mostly controlled by water saturation levels and local geology, though results are similar in most cases.

In Chapter 4, I use the clustering of earthquake induced landslides to test the variability of initial roughness of landslides that failed under similar conditions. I also investigate how landslide roughness evolves over time with repeat Lidar surveys of a single landslide. I find that the variability in initial roughness is high, but it can be reduced by considering only large landslides ($\geq$10,000 m^2) and by considering different geologic units separately. Geologic units also control how the landslide deposits smooth out over time. Based on this,

it is necessary for future use of landslide roughness for age estimation to only consider large landslides and to analyze landslides in different geologic units separately.

Together, this work advances the field by improving our ability to estimate the age of landslides. These ages finally allow regional investigation of landslides induced by earthquakes that occurred before modern instrumentation. This knowledge leads to a better understanding of the future hazards and erosional force of earthquake induced landslides. We also demonstrate that earthquake induced landslides can be useful as a tool for understanding earthquakes and landslides more generally.

VITA

Erich Herzig grew up in Ojai, California. He graduated from the Thacher School in 2014 and graduated from Caltech with a B.S. in Geophysics in 2018.